Aircraft Plume Modelling For Quantifying Near-Runway Air Quality

Investigating the influence of different ambient and operational conditions to understand the effect on jet plume evolution

Aircraft Noise and Climate Effects

Samuel Otterloo

Delft University of Technology

TU Delft

Aircraft Plume Modelling For Quantifying Near-Runway Air Quality

Investigating the influence of different ambient and operational conditions to understand the effect on jet plume evolution

by

Samuel Otterloo

Student Name	Student Number
Samuel Otterloo	4559681

Instructor:	Dr. I.C. Dedoussi
Teaching Assistant:	L. Koji Kavabata
Project Duration:	3, 2023 - 10, 2024
Faculty:	Faculty of Aerospace Engineering, Delft

Cover: Photo taken by author

TU Delft

Preface

Dear reader,

This thesis is submitted in partial fulfilment of the requirements for the Master of Science degree in Aerospace Engineering at Delft University of Technology. The work presented in this document was carried out at the Faculty of Aircraft Noise and Climate Effects under the supervision of Dr I.C. Dedoussi during the period from March 2023 to September 2024.

I would like to thank a few people for their unconditional love and support throughout this journey. My parents, Katy and Henk, thank you for always listening and encouraging me. My girlfriend, Charlotte, thank you for always trying to help and motivate me during this academic rollercoaster.

In addition, a sincere thank you to my supervisor, Dr I.C. Dedoussi, for providing new insights and feedback to complete this research in the best possible way. I would also like to thank Luccas for his constant willingness to try and help with all sorts of problems that have arisen throughout this project.

Samuel Otterloo
Delft, October 2024

Summary

With growing concerns about air quality around airports and runways, this research develops a jet plume model to predict how pollutants disperse in these environments. Data from the model will be compared with experiments conducted at Schiphol Airport to provide insight into the performance of the model. The jet plume model was created using the COMSOL CFD multiphysics engine. This resulted in the calculation of the velocity and pressure profiles of the flow. The specific species studied being NO, NO_2 and CO. The different operational and environmental variables are described and established as input parameters for the model. A time-dependent study is chosen to be able to simulate the plume over a given time period. Plume identification is performed using a threshold concentration limit value set at 2.5% of the peak value. This allows the analysis of the plume. Two different characteristics of the plume are examined. The first is the width of the plume, which can be determined using the previously constructed concentration threshold. The second is the peak contaminant concentration. In addition, different types of plume cross-sections were analysed and a mean value approach was chosen.

The complete model is subjected to a sensitivity analysis, where all the different parameters are examined to understand their effect on the model. The results showed that the ambient wind speed had the greatest effect on the plume. For every $1 m/s$ increase in wind speed, the plume width decreased by an average of 3.49%. Another finding was that increasing the input concentration did not lead to a wider plume. Only the plume peak became higher. In addition, another variable that strongly affected the plume width and, thus, the concentration value was the aircraft velocity component. An increase of 1 m/s meant that the plume width increased by 3.36%.

The model plume widths were compared with the plume widths collected at the measurement site. For both arrivals and departures, the mean plume widths of the model and experiments were in relative agreement. The simulation of plumes from arriving aircraft resulted in a mean plume of 203.34 metres, while the measurements showed a mean of 217.17 metres. The measurements of departing aircraft show a mean width of 229.34 metres, and the simulations 234.33 metres. The discrepancies can be seen by looking at the variance of the two sets of data. The standard deviation of the measurements is 86.05 metres for departures and 73.21 metres for arrivals. The model shows a much smaller variance, i.e. the standard deviation is 17.33 for departures and 49.16 for arrivals. This discrepancy in variance is probably due to the fact that variable parameters in real life are translated into constants in the model, for example, wind speed and aircraft speed.

The results for the concentration values showed a specific flaw in the input concentration method. When considering medium and smaller aircraft, the results showed concentrations for all pollutants, CO, NO and NO_2, that were in the same range as the simulations. The method was unable to produce a workable approach for larger aircraft, as this resulted in a value well in excess of the measurements. This was the case for both arrivals and departures. This indicates that this method has the potential to quantify and simulate the pollutants associated with the landing and take-off cycles of small to medium-sized aircraft.

Contents

List of Figures

List of Tables

Nomenclature

Abbreviations

Abbreviation	Definition
CFD	Computational Fluid Dynamics
CV	Coefficient of Variation
EI	Emission Index
FAR	Fuel to air ratio
FEM	Finite Element Method
HC	Hydro Carbons
ICAO	International Civil Aviation Organisation
LTO	Landing and Take-off cycles
MNB	Mean Normalised Bias
NVPM	Non-Volatile Particulate Matter
PAH	Polycyclic aromatic hydrocarbons
PM0.1	Particulate matter smaller than 0.1μm
PM10	Particulate matter smaller than 10μm
PM2.5	Particulate matter smaller than 2.5μm
RANS	Reynolds-Averaged Navier Stokes
RMSE	Root mean square error
SAF	Sustainable Air Fuels
UFP	Ultrafine Particles
UHC	Unburned Hydro Carbons
VOC	Volatile organic compounds
MAE	Mean Absolute Error
PPM	Parts Per Million
MSE	Mean Squared Error
MBE	Mean Bias Error

Symbols

Symbol	Definition	Unit
HO_x	Hydrogen oxides	
NO_x	Nitrogen oxides	
CO	Carbon Monoxide	
C_nH_m	Hydro Carbons	
S	Sulfur	
O_2	Oxygen	
N_2	Nitrogen	
H_2O	Water	
SO_2	Sulfur-dioxide	
SO_x	Sulfur-oxides	
ϕ	Stoichiometric fuel ratio	
m_{ox}	Molar mass oxygen	g/mol
m_{fuel}	Molar Mass Fuel	g/mol
SO_3	Sulfur-trioxide	
H_2SO_4	Sulfur-acid	

Symbol	Definition	Unit
NH_3	Ammonia	
NH_4NO_3	Ammonium Nitrate	
NH_42SO_4	Ammonium Sulfate	
NH_3	Ammonia	
NH_3	Ammonia	
$T_{duration}$	Plume duration time	s
T_{start}	Plume start time	s
T_{end}	Plume end time	s
β	Wind angle	degrees
U_{wind}	Wind speed	m/s
$\bar{d}$	Mean of the differences between the paired observations	
s_d	Standard deviation of the differences	
n	Number of pairs	
y_i	Observed experimental values	
$\hat{y}_i$	Model predicted values	
β_0	Intercept Regression Line	
β_1	Slope of the regression line	
e_i	Residual Value	
$S(\beta_0, \beta_1)$	Sum of residual values	
R^2	Coefficient of determination	
ϵ	Dissipation Rate	m^2/s^3
v_i, u_j	Velocity Components	m/s
x_i, y_j	Spatial Coordinates	m
$c_{b1}, c_{b2}, c_{f1}, c_{fw}$	Spalart-Allmaras model constants	
ρ	Fluid density	kg/m^3
μ, μ_t	Molecular/Turbulent viscosity	Pa·s
P_e	Exhaust Engine Pressure	Pa
T_e	Exhaust Engine Temperature	K
A	Engine Exit Area	m^2
V_{exit}	Engine Exit Speed	m/s
V_{sound}	Speed of sound	m/s
γ	Heat Capacity Ratio	
α	Corrected wind angle	$degrees$
$U_{aircraft}$	Speed of the aircraft	m/s
V_{air}	Initial airspeed	m/s
p_t	total air pressure	pa
M_{exit}	Engine Exit speed in mach	m/s
$C_{threshold}$	Concentration Threshold	mol/m^3
L_{width}	Arc length plume	m
$C_{i,j,k}$	Input concentration	ppm
i	Engine mode	
j	Type of engine	
k	Pollutant type	
FF	Fuel Flow	kg/s
R	Gas constant	$J * mol/K$
V	Engine Volume	m^3
σ	Standard Deviation	
σ^2	Variance	

1 Introduction

According to the International Civil Aviation Organisation, the demand for air transport is expected to show a steady growth of 4,3% per annum over the next 20 years [27]. This growth will also fuel an increase in the emissions contributed by aviation. Aircraft emissions hurt the health and well-being of human populations. It has been studied that 16000 premature deaths can be directly linked to emissions of $PM_{2.5}$ and ozone that are aviation-attributed [5, 66]. A quarter of these premature deaths are caused by the Landing and Take-off (LTO) cycles [66]. These cycles account for high local peak levels of air pollution near the airports as they are emitted at a low altitude and in relative proximity to the urban areas. This phenomenon has been confirmed by multiple studies which describe the relationship between the growth in airport activity and the population density around the airport. It has been estimated that if the activity at a specific airport would grow by 10% the population density would increase by 3.8% within a 7.5 km radius of the airfield [12]. This highlights the significance of the research regarding local air quality.

Airports do not only have negative effects. Airports are also important economic catalysts, bringing in billions of dollars and boosting local and regional economies [21]. Air quality worries near airports, however, can hurt the commercial climate and property prices. Due to worries about air pollution, businesses near airports may find it difficult to recruit and keep personnel, and property values in polluted areas may decrease. This could result in a drop in economic activity, negating the airport's beneficial economic effects. The air around airports needs to be cleaner if sustainable economic growth is desired. This may result in putting in place regulations to restrict emissions from planes and other ground-based sources, encouraging the use of different forms of transportation, and making investments in clean energy technologies. Communities benefit from this as it still promotes economic growth while protecting the health of the human residents.

Atmospheric and environmental conditions impact the emissions during Landing and Take-off cycles. It is important to accurately assess the air quality near the airports to develop strategies to mitigate the potential impact of aircraft emissions. This has to start at the origin of the pollutants: the jet engine. The emissions from the jet engine develop into a plume consisting of gaseous pollutants such as HO_x, NO_x, and CO. In addition, particulate matter is emitted through the plume [41]. Both of these aspects must be evaluated carefully to quantify the air quality.

1.1. Thesis Objective

Quantifying the air quality near the airport can be seen as very significant. There are different ways to tackle this objective. One of these is using jet plume models. This models the plume that is emitted from the jet engine and predicts its development and evolution. There are many different methods for modelling jet engine plumes, each with strong points and shortcomings [68, 4]. This project aims to develop a model that accurately describes the jet plume development and dispersion of pollutants of aircraft taking off and landing at Schiphol Airport. In addition to the plume model, data will be used with the help of low-cost sensors placed along the runway at Schiphol to validate and compare the results

from the model. This data will contain information about the concentration of the different pollutants and particulate matter that are present in the air. The data can be used to further optimise and validate the plume model. Improving the modelling of the plume results in the fact that projections of pollution dispersion would be more precise, allowing for better strategies for mitigating air pollution around airports. The low-cost sensor measurements thus play an important role in validating the jet plume model. The main research objective will be as follows:

"How effectively does the jet plume model developed for quantifying aircraft-attributable emissions replicate the observed experimental data collected at Schiphol?"

This research question will be supported by three research questions.

1. *How sensitive is the model to variations in ambient and operational conditions, and what impact do these factors have on the accuracy of its predictions?*
2. *Is the model able to accurately predict the plume width from the aircraft compared to the experimental measurements at Schiphol Airport?*
3. *How well do pollutant concentration levels predicted by the jet plume model match the experimentally observed concentrations for different types of aircraft pollutants?*

1.2. Outline of the Report

The report can be seen as a summary of all the work done to carry out this research. Chapter 2 provides the background information necessary to understand the context of this study. Chapter 3 consists of the construction of the plume model. Subsequently, the model is subjected to a sensitivity analysis, which can be seen in Chapter 4. In Chapter 5, the data from the model are presented, where the plume widths and concentration values from the model are compared with the measurements. Finally, Chapter 6 presents the conclusions drawn from the study and recommends improvements for future research.

2

Background

This chapter aims to give the necessary background information for the thesis. Aviation Attributable Emissions are discussed. The various pollutants that aeroplanes emit, such as carbon dioxide, nitrogen oxides, sulfur dioxide, particulate matter, and others, are described. The chapter also looks at how operational factors like aircraft type, altitude, and weather might affect the quantity and makeup of these pollutants. The chapter concludes by exploring the effects of these pollutants on the environment and public health and illustrating the importance of ongoing initiatives to mitigate aviation's environmental impact.

2.1. Types of Pollutants

Aviation emits two different forms of emissions into the atmosphere: gaseous pollutants and particulate pollution. Compounds like carbon monoxide, nitrogen oxides, and sulfur dioxide are examples of gases that can be harmful to the environment and human health [36]. On the other hand, fine particles suspended in the air, like soot and dust, make up particulate matter. In particular, when inhaled, these particles can be hazardous to both human health and the environment [5]. The main distinction between particulate matter and gaseous pollutants in aviation is that particulate matter is frequently created by the combustion of gasoline and other materials in the engine, whereas gaseous pollutants are typically emitted from the engines themselves [50].

2.2. Gaseous Pollutants

The first type of pollutants that are studied are gaseous pollutants. The gaseous pollutants find their origin in the engine of the aircraft. During the combustion process, various pollutants are formed and emitted. To analyse this, it is important to understand the combustion process in the jet engine. When fuel and air are combined in a jet engine and ignited, combustion takes place, the energy that is released powers the turbine and moves the aircraft forward. Combustion can often be divided into ideal or complete combustion and actual combustion. These two combustion processes refer to an idealized, theoretical situation and the imperfect, real-world circumstances that can impact combustion in a jet engine.

2.2.1. Combustion Process

The combustion process is the origin of most of the pollutants that are attributed to aviation. Therefore, looking at what takes place during that process will help us understand the different chemical components that are emitted. If a perfect fuel-air mixing and instantaneous burning of all the fuel molecules were assumed, it would be considered ideal combustion. As a result, there are no waste products or byproducts and all the energy will go towards forming the thrust the aircraft needs. The theoretical temperature and pressure produced by ideal combustion serve as a standard against which to compare actual performance [16].

On the other hand, actual combustion involves several variables that may have an impact on the com-

bustion process, including incomplete fuel and air mixing and pollutants or impurities in the fuel. These aspects may cause less effective combustion, which could result in pollutants such as carbon monoxide, unburned hydrocarbons, nitrogen oxides as well as certain fuel molecules that are not completely burnt. The temperature and pressure of the combustion gases can also be lowered due to incomplete combustion, which will reduce the turbine's efficiency and the engine's overall performance [51].

The ideal and actual combustion processes can be described using the following chemical formulas. Important to note that these are not balanced as this depends on the fuel type.

$$C_nH_m + S + O_2 + N_2 \longrightarrow CO_2 + H_2O + N_2 + O_2 + SO_2 \tag{2.1}$$

Equation 2.1 illustrates the chemical formula of an ideal combustion process in the engine [36]. The air intake of the engine is characterized by the molecules O_2+N_2. The fuel is depicted as a combination of carbon and hydrogen atoms: C_nH_m. The chemical compound S means sulfur, which can be present in a low amount in aircraft fuel.

$$C_nH_m + S + O_2 + N_2 \longrightarrow CO_2 + H_2O + N_2 + O_2 + SO_x + NO_x + Soot + HC + CO \tag{2.2}$$

Equation 2.2 shows what the combustion process of a jet engine actually looks like [36]. As can be seen, there are more by-products compared to the ideal combustion process in Equation 2.1.

2.3. ICAO Modes

The amount of emissions an aircraft emits depends on which phase of flight it is. As with a take-off, some pollutants are more present than others. To distinguish these different phases ICAO has constructed four different modes [26]. These phases are linked to the Landing and Take-off cycle (LTO). An LTO occurs at low altitudes and, therefore, has a significant impact on the local air quality [20]. Therefore, this is the most important part of a flight to consider when evaluating the local air quality near airports. The LTO cycle defined by ICAO is set below an altitude of 915 metres [26].

2.3.1. LTO Cycle Modes

The different modes are listed in Table 2.1. The mode with the highest thrust setting is the Takeoff mode. Here the thrust is used to provide the aircraft with lift during takeoff and initial climb. In this mode, the engine must be capable of providing the maximum amount of power while maintaining a high level of efficiency. This is important to ensure that the aircraft can take off safely and reach a safe altitude promptly. It is important to note that here, the thrust setting is set at 100%. However, in real-life operations, this is often not the case. This is mainly due to engine lifetime and cost-efficiency reasons, the take-off thrust could be as low as 60% [26]. The approach mode describes the aircraft descending and approaching the runway, thus a low thrust percentage is needed. At the beginning of the flight, the aircraft is in idle mode. During this mode, the engine operates at a low power setting to conserve fuel and minimize noise. However, it must still provide enough power to operate the aircraft's auxiliary systems, such as air conditioning, hydraulic pumps, and electrical generators. In this mode, the engine is also required to provide sufficient thrust for the aircraft to move forward and steer on the ground, which is needed when the aircraft needs to taxi to the runway. The idle mode is combined with the taxi mode of the aircraft taxiing to the runway. Both of these phases require a low amount of thrust, 7%. Therefore, they are grouped [37]. The last mode is the climb mode, which happens after the aircraft has taken off. The aircraft climbs to the cruise altitude, and the end of the climb mode is, as mentioned, at an altitude of 915 metres. An important remark regarding these modes is that it is a simplification, this can be seen that for example the change from take-off mode to climb mode is modelled with an instantaneous change in thrust setting, from 100% to 85%.

Operating phase	Time-in-mode (minutes)	Thrust setting (% of rated thrust)
Approach	4.0	30
Taxi and ground idle	26.0 (7.0 in, 19.0 out)	7
Take-off	0.7	100
Climb	2.2	85

Table 2.1: ICAO Modes [26]

The different modes thus describe how the thrust setting differs in the aircraft. The thrust setting, in combination with the Time-in-mode, can help with the calculation of the exact emission of the plane.

2.3.2. Reverse Thrust

In addition to the different ICAO modes, it is important to consider another phenomenon: reverse thrust. To slow down an aircraft during landing, pilots can use reverse thrust, which allows them to direct the engine's thrust forward rather than backward. An airplane approaches the runway during a landing at a relatively high speed, and it is the pilot's job to slow the plane down before impact. To guarantee that the aircraft can land safely within the allotted landing distance, the speed must be reduced. It is not always used due to safety concerns, like a shorter runway. Sometimes, it is more efficient for aircraft to use a taxiway that is positioned higher up the runway, which requires the airplane to reduce its speed at a higher rate. Altering the angle of the engine exhaust provides a force that pushes back against the plane's motion, slowing it down, and this is used to apply reverse thrust. When reverse thrust is activated, the air is pushed towards the front of the airplane. As a result, the engine thrust reduces the aircraft's speed by acting in the opposite direction of the aircraft's motion. Depending on the type of aircraft, its weight, and the landing circumstances, different amounts of thrust are used during reverse thrust. However, the average amount of push used for reverse thrust is about 30%. There are also more modern jet engines which can produce a reverse thrust of about 30-55% [1]. A study on landings at a US airport concluded that the average time of reverse thrust is around 16 seconds [49]. This phenomenon is important to consider as a reverse thrust sequence can drastically alter the amount of pollutants emitted.

2.3.3. Fuel to Air Ratio

In addition to the different ICAO modes described in section 2.3 other factors are important when considering aviation-attributable emissions. Depending on the level of flight, aircraft engines are built to operate at certain air-fuel ratios.

In aircraft, the fuel-to-air ratio (FAR) is important to understand. One of the key aspects that illustrate this is the equivalence ratio (ϕ). The equivalence ratio is a dimensionless ratio used in combustion engineering to compare the stoichiometric fuel-air mixture ratio. The stoichiometric mixture is the ideal proportion of fuel and air needed to achieve complete combustion, which means that all of the fuel is consumed by the air, leaving no unburned fuel [24]. The equivalence ratio is defined using Equation 2.3.

$$\phi = \frac{(\text{ FAR })_{\text{Actual}}}{(\text{ FAR })_{\text{stoichiometric}}} = \frac{(m_{\text{fuel}}/m_{\text{ox}})_{\text{Actual}}}{(m_{\text{fuel}}/m_{\text{ox}})_{\text{stochiometric}}} \tag{2.3}$$

In equation Equation 2.3 is shown how ratio can be calculated. To be able to compare both the actual and stoichiometric ratios, the masses of both situations are needed. m_{fuel} represents the mass of the fuel used both in the stochiometric equation and the actual. The same is done for the oxygen, m_{ox}. If the actual fuel-air ratio is less than the stoichiometric ratio, the equivalence ratio is less than 1, and the mixture is called lean. If the actual fuel-air ratio is greater than the stoichiometric ratio, the equivalence ratio is greater than 1, and the mixture is called rich. If the actual fuel-air ratio is precisely equal to the stoichiometric ratio, the equivalence ratio is equal to 1, and the mixture is called stoichiometric [24].

The equivalence ratio plays a crucial role in determining the species and amount of pollutants emitted from an aircraft engine. At lean equivalence ratios (less than one), the combustion temperature is relatively low, resulting in incomplete combustion of the fuel. This leads to the production of high amounts of unburned hydrocarbons ($UHCs$) and carbon monoxide (CO), which are harmful pollutants. On the other hand, at rich equivalence ratios (greater than one), the combustion temperature is high, leading to the production of nitrogen oxides (NO_x), which are also harmful pollutants. Thus, it is essential to maintain an optimum equivalence ratio during aircraft operations to minimize the emission of pollutants and ensure better air quality. In taxi mode, the equivalence ratio used is relatively lean, as the engine is operated at a low power setting to conserve fuel and minimize noise. This process is shown in Figure 2.1.

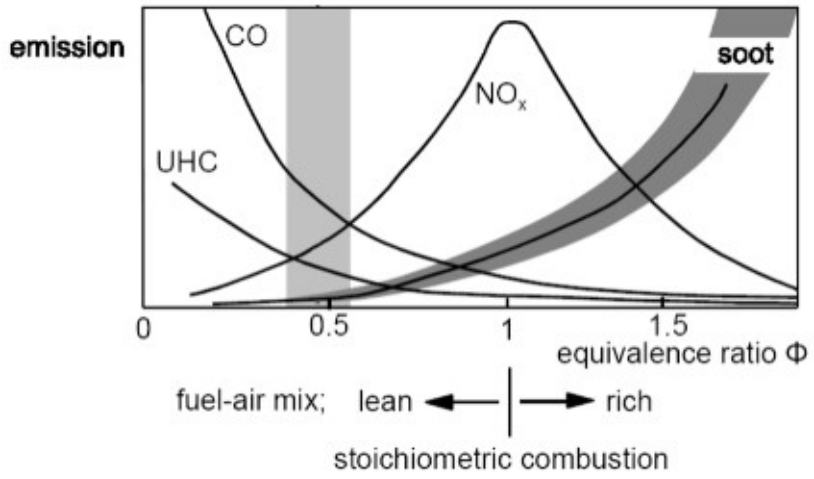

Figure 2.1: Impact of the Equivalence ratio on the species of pollutants emitted [31]

The equivalency ratio is normally set to a value larger than 1, which is referred to as a fuel-rich mixture, during the takeoff mode. To make sure the engine generates enough power to lift off the ground and ascend to a greater height, this is done. A mixture that is high in fuel, however, also generates additional pollutants, such as carbon monoxide and unburned hydrocarbons [25].

The equivalency ratio is normally set to a value around 1, which is referred to as a stoichiometric mixture when the vehicle is in cruise mode. This is done to guarantee that the engine runs as efficiently as possible while emitting as few emissions as possible. In this setting, the engine produces an equal amount of nitrogen oxides and carbon dioxide, which are less damaging to the environment than other emissions [25].

If the airplane is in idle mode, the equivalency ratio is normally adjusted to a value less than 1, also known as a lean mixture. In doing so, it is possible to lower fuel use and pollutants while maintaining auxiliary system functionality.

It's important to keep in mind that for the aircraft to run safely and efficiently, the right air-fuel ratio must be maintained. A poor air-fuel ratio can damage or even ruin an engine while also raising pollutants and fuel consumption. There are strict operational protocols and maintenance practices in place to make sure that the air-fuel ratio is always maintained within the right range.

2.4. Nitrogen Oxides

Now that the different pollutants have been identified, it is possible to individually analyse and further describe the formation of the pollutants. The first pollutant is Nitrogen oxide or NO_x. Vedeshkin et al illustrate different mechanisms that result in the formation of NO_x [62]. The first mechanism was established by Zeldovich. This was characterized by the following set of chemical reactions.

$$\begin{aligned} \mathrm{N_2 + O} &\overset{k_1}{\rightleftharpoons} \mathrm{NO + N} \\ \mathrm{N + O_2} &\overset{k_2}{\rightleftharpoons} \mathrm{NO + O} \\ \mathrm{N + OH} &\overset{k_2}{\rightleftharpoons} \mathrm{NO + H} \end{aligned} \tag{2.4}$$

Equation 2.4 describe how N_2 oxides and how other nitrogen elements bond with OH radicals in a set of equilibrium equations. This results in the formation of nitrogen monoxide. All these reactions occur when the temperature is high enough, such as is the case in a jet engine [62]. The nitrogen oxide that is formed can also react even further. Oxidation leads to the formation of nitrogen dioxide, which in turn plays an important role in the formation of Ozone and smog [6].

2.5. Sulfur Oxides

Similarly to nitrogen oxides, sulfur oxides are also a product of the combustion process in a jet engine, mainly because the combustion is incomplete. Sulfur oxides (SO_x) typically do not form in jet engines due to the very low sulfur content of aviation fuels. However, sulfur in fuel can react with oxygen during combustion to form sulfur dioxide (SO_2) and sulfur trioxide (SO_3) [2]. The sulfur content in jet fuels has been limited by regulations, however, the sulfur content is still allowed to be 0,3% of the fuel weight [58]. The sulfur in the fuel reacts with air due to the high temperature in the combustion chamber, which can be seen in Equation 2.5.

$$\begin{aligned} \mathrm{S + O_2} &\longrightarrow \mathrm{SO_2} \\ \mathrm{2\,SO_2 + O_2} &\longrightarrow \mathrm{2\,SO_3} \end{aligned} \tag{2.5}$$

The sulfur trioxides also play a role in the formation of acid rain. This compound will react with water vapour in the atmosphere to form sulfuric acid, H_2SO_4. As is seen in Equation 2.6.

$$\mathrm{SO_3 + H_2O} \longrightarrow \mathrm{H_2SO_4} \tag{2.6}$$

2.6. Carbon Monoxide

Carbon monoxide (CO) is produced during the combustion process because it is a byproduct of incomplete combustion. In ideal combustion, the fuel reacts completely with oxygen to produce carbon dioxide (CO_2) and water vapour (H_2O). However, in situations where there is insufficient oxygen, the fuel cannot be fully oxidized and carbon monoxide is produced instead. The reaction is depicted in Equation 2.7

$$\mathrm{2\,C + O_2} \longrightarrow \mathrm{2\,CO} \tag{2.7}$$

2.7. Ozone

The last pollutant that also occurs through the emissions is ozone, O_3. This pollutant is formed due to the emission of NO_2 by aircraft. NO_2 can be broken down by photolysis, as is seen in Equation 2.8. This causes a free oxygen atom to form. In turn, this atom can react with molecular oxygen, O_2, to form ozone. This can be seen in Equation 2.9.

$$\mathrm{NO_2 + hv} \longrightarrow \mathrm{NO + O} \tag{2.8}$$

$$\mathrm{O_2 + O} \longrightarrow \mathrm{O_3} \tag{2.9}$$

2.8. Particulate Matter

Now that several gaseous pollutants have been discussed, the focus will be on another type of pollutant attributable to aviation: Particulate matter. Particulate matter (PM) is a complex mixture of small particles suspended in the air, which can have negative impacts on human health and the environment [6, 66]. Aircraft engines are a significant source of PM emissions, and the PM produced by aircraft engines can be categorized into two main types: primary PM and secondary PM. In addition to these two categories, another important aspect is that the formation of primary PM can be influenced by several factors, such as the type of fuel used in the engine, the engine design, and the operating conditions of the engine. The size, composition, and quantity of primary PM can vary depending on these factors [69, 53].

2.8.1. Primary Particulate Matter

Primary PM is directly emitted from aircraft engines and, therefore, impacts the local air quality of airports. The incomplete combustion of fuel in the aircraft engine causes this phenomenon. Primary PM falls into three main categories [31].

- Black/Elemental carbon (soot): This is a direct product of the incomplete combustion that takes place in the aircraft engine. Due to this incomplete mixing of fuel and air, not all carbon from the jet fuel has the opportunity to oxidize [57]. This results in the formation of Black/Elemental Carbon or soot.
- Primary Organic Aerosol: This primary PM is mainly formed from the emission of volatile organic compounds (VOCs) during the combustion process. These VOCs can condense and form particles through nucleation, which can be emitted directly from the aircraft engine. The chemical composition of primary organic aerosols in aviation can vary depending on the type of fuel used, the combustion process, and the engine design. However, typical compounds include: formaldehyde, benzene, tetrachloroethylene, trichloromethane, 1,2-dichloroethane, and naphthalene [67].
- Primary Sulfate: Aviation fuel contains sulfur in small amounts, as was discussed in section 2.5. Most of this sulfur is emitted as sulfur dioxide (SO_2) during combustion. However, as was shown in Equation 2.6, some of the SO_2 can be converted into fully oxidized sulfuric acid (H_2SO_4) through chemical reactions with oxygen and water inside the engine [30]. The degree of conversion into H2SO4 depends on various factors such as combustion conditions, turbine flow properties, blade cooling effects, and mixing [30]. The sulfuric acid can then form clusters that lead to the formation of primary sulfate.

These types of primary particulate matter are all related to the jet engine and exhaust of the aircraft. However, there are also non-exhaust emissions caused by the wear and tear of different aircraft components, such as brakes and tyres. The amount of these emissions depends on various factors, such as aircraft weight and runway condition. The studies regarding this type of particulate matter are limited. However, it is starting to develop in the transportation sector [47].

2.8.2. Secondary Particulate Matter

Secondary particulate matter (PM) is formed in the atmosphere as a result of complex chemical reactions between gases emitted by aircraft engines, such as nitrogen oxides and sulfur dioxide. The formation of secondary PM involves several steps, including gas-phase oxidation of NO_x and $SO2$ to form nitric acid (HNO_3) and sulfuric acid (H_2SO_4), respectively. These acids can then react with ammonia (NH_3) and other atmospheric compounds to form ammonium nitrate (NH_4NO_3) and ammonium sulfate ((NH_4)2SO_4), which are two common types of secondary PM [32].

Other types of secondary PM can form due to the oxidation of VOCs, which are emitted by aircraft engines and are precursors to the formation of secondary organic aerosols. These secondary organic aerosols are complex organic compounds that can form through a series of reactions involving VOCs and other atmospheric compounds and can contribute to the formation of fine particulate matter[65].

The formation of secondary PM can occur over a range of time scales, from hours to days, depending on atmospheric conditions such as temperature, humidity, and sunlight. The formation of secondary

PM can also be influenced by the altitude and location of aircraft emissions, as well as the composition of the surrounding air [65].

In addition to the type of PM produced, the amount of PM emitted by aircraft engines can vary depending on factors such as engine type, fuel type, and flight conditions. For example, older aircraft engines tend to produce more PM than newer engines, and engines burning high-sulfur fuels tend to produce more sulfur oxides (SO_x), which can contribute to the formation of secondary PM [58].

2.8.3. Properties

The properties of particulate matter are needed to model the dispersion of the particles carefully. One of the most evident properties is size. There are three main categories into which particulate matter can be divided [60].

- PM_{10}: Particles in this category have a diameter smaller than 10 micrometres (μm), these particles are also known as inhalable or coarse particles.
- $PM_{2.5}$: Particles in this category have a diameter smaller than 2.5 micrometres (μm). Particles of this size are seen as fine particles.
- $PM_{0.1}$ *or Ultrafine particles*: Particles in this category have a diameter smaller than 0.1 micrometres (μm). This category consists of the finest particles, and therefore, all particles smaller than the threshold can be seen as ultrafine particles.

In addition to size, there also is another aspect of particulate matter that is important to consider. There is a distinction that can be made between non-volatile particulate matter (NVPM) and Volatile particulate matter (VPM).

- *Non-volatile particulate matter*: This type is composed of particles that do not evaporate at the temperature at which a jet engine typically operates. Due to this fact, NVPM is generally considered to be a significant contributor to air pollution, as it can remain in the atmosphere for long periods and has been linked to a range of health and environmental impacts [6, 5].
- *Volatile particulate matter*: This type of particulate matter refers to particles that are formed when volatile organic compounds are released from aircraft engines and react with other compounds in the atmosphere. These particles can include secondary organic aerosols, for example. Compared to NVPM, volatile particulate matter has a shorter lifetime. This does not mean it is less harmful to the environment and human health. A shorter lifetime may result in the air quality far away being less impacted, but at a local level can still contribute to the degradation of the air. However, looking at the total amount of PM emitted by jet engines only 5% is classified as volatile [36].

2.9. Air Quality Guidelines

In the last sections, the different pollutants that play a role in the aircraft's attributable emissions were discussed. In the thesis, the air quality will be quantified, but it is important to be able to put these into context. This can be done through the World Health Organization's (WHO) air quality guidelines [63]. These guidelines provide a benchmark for assessing the results that flow from this thesis. By aligning the thesis with these international standards, the research obtains more credibility and relevance. The guidelines are shown in Table 2.2.

Pollutant	Averaging time	Interim target 1	Interim target 2	Interim target 3	Interim target 4	AQG level
$PM_{2.5}$ ($\mu g/m^3$)	Annual 24-hour[a]	35 75	25 50	15 37.5	10 25	5 15
PM_{10} ($\mu g/m^3$)	Annual 24-hour[a]	70 150	50 100	30 75	20 50	15 45
O_3 ($\mu g/m^3$)	Peak season[b] 8-hour[a]	100 160	70 120	- -	- -	60 100
NO_2 ($\mu g/m^3$)	Annual 24-hour[a]	40 120	30 50	20 -	- -	10 25
SO_2 ($\mu g/m^3$)	24-hour	125	50	-	-	40
CO (mg/m^3)	24-hour	7	-	-	-	4

Table 2.2: The different recommended air quality levels per pollutant constructed by the WHO [64]

[a] 99th percentile (i.e., 3–4 exceedance days per year).
[b] Average of daily maximum 8-hour mean O_3 concentration in the six consecutive months with the highest six-month running-average O_3 concentration.

In Table 2.2 the guidelines are shown per pollutant. In addition, the concentration is averaged over both an annual and a daily time period. As can be seen in the table, different interim targets are shown. Starting with Interim target 1, this target is the least stringent; for $PM_{2.5}$, this value is equal to 35$\mu g/m^3$ annually. The first target is for countries whose air is severely polluted and can work towards this first value. As the interim targets move up the threshold becomes stricter and stricter. The most optimal level of air quality is denoted with AQC (Air Quality Guidelines).

2.10. Sensors Used

The experiments at Schiphol are carried out using several sensors. The sensors are used to measure and store the data. Therefore, it is important to understand the sensors. This helps ensure the accuracy, reliability, and validity of the data that is used to compare the model. As mentioned in section 2.2 and section 2.8, two main types of pollutants are present when assessing aviation-attributable emissions. Thus, two types of sensors are needed to capture and quantify the air quality.

2.10.1. Naneos Partector

One of the sensors used is the Naneos partector, which can be seen in Figure 2.2. This device is a portable nanoparticle counter developed by Naneos [43]. Most devices that use optical detection of particulate matter are unable to detect particles smaller than 300 nanometers. The Naneos Partector can detect particles down to 10 nanometers making it a suitable option for measuring particulate matter from aircraft.

Figure 2.2: The Naneos partector used for measuring particulate matter [43]

When looking at the working principle of the sensor, four key steps illustrate how the sensor can detect particulate matter.

- *Sampling*: The sampling step is based on the fact that the air containing nanoparticles is sucked using an integrated pump in the device, which ensures that the representative samples are collected from the environment.
- *Condensation*: After the device has sucked in the air, the sample enters the measurement chamber. In this chamber, the air encounters supersaturated vapour. This vapour rapidly condenses on the the particles that are present in the air, which enlarges the size of the particle. This process helps to detect even the smallest of particulate matter.
- *Detection*: The particles that are enlarged pass through the detection zone of the partector. Here, using electrical currents, the system can accurately measure the properties of the particle.
- *Analysis*: The data collected from the particles are processed and analyzed in real-time by the partectors onboard software. This software translates the measurements into insights that can be used to draw conclusions about air quality.

Like all sensors, the partector has its limits and specifications as to what it is able to measure and what not. These specifications are shown in Table 2.3.

Specifications Partector	**Range**
Long Deposited Surface Area	0 - 12000 $\mu m^2/cm^3$
Number of Particles	0 - $10^6 cm^{-3}$
Average particle diameter	10 - 300 nm
Surface area concentration	0 - 50000 $\mu m^2/cm^3$
Mass particle range	0 - 2500 $\mu g/m^3$
Time resolution	1 second

Table 2.3: The specifications of the Naneos Partector [43]

2.10.2. Gas Sensor Boxes

The gaseous pollutants emitted by the aircraft are measured using gas sensor boxes. The sensor boxes were created as part of a previous master thesis done by Jeff Maes [38]. The boxes can identify the pollutants such as NO_x and CO. The boxes were created using an Arduino and were set in a casing. The box was not only able to capture pollutant concentration but also meteorological information such as humidity, temperature, and pressure. The four boxes can be seen in Figure 2.3; here, they are positioned at the Polderbaan at Schiphol.

Figure 2.3: The 4 gas sensor boxes positioned next to the Polderbaan at Schiphol used for measuring gaseous pollutant

These boxes are the measuring equipment regarding the gaseous pollutants. Therefore, it is important to analyse the error margins of these sensors. The errors are important as the data is used to validate and compare the jet plume model that will be created. These margins were calculated at a setup in Wijk aan Zee. Here, different resolution times and specific species were tested to quantify the error. It is important to note that these error margins were calculated at concentrations higher than the 90% quantile of the test. So, in other words, the error margins for more extreme or peak values of the pollutants were analysed. The margins can be seen in Table 2.4.

	CO 10 s	CO 1 min	CO 60 min	NO 10 s	NO 1 min	NO 60 min	NO_2 10 s	NO_2 1 min	NO_2 60 min
Mean error μgm^{-3}	219.17	220.24	9.77	4.91	3.00	1.65	5.06	4.36	1.43
Median error μgm^{-3}	111.56	89.50	9.77	3.27	2.11	1.64	4.32	3.99	1.43

Table 2.4: The error margins of the gas sensor boxes for concentrations higher than the 90% quantile of the Wijk aan Zee experiment [38]

2.11. Data Measurements

The focus of this research is on the plume modelling aspect. However, it is also necessary to compare this model with measurements taken at Schiphol. This work has been carried out by students Jeff Maes and Rik Goudswaard [38, 22]. They have implemented methods to measure the plumes and compare them with subsequent aircraft landing and arriving at the Polderbaan. Part of their research leads to the plots shown in Figure 2.4. This time series plot monitors the peaks of the pollutants, and through the use of ADS-B, it is possible to identify which aircraft the plume belongs to. This is shown for the pollutant CO. This type of data from the experiments is used in this research to understand the accuracy and validity of the results from the jet plume model.

2.11.1. Plume Width Measurements

The data collected from the measurements were made on the sensors discussed in subsection 2.10.1 and subsection 2.10.2. The model is then used to calculate the width of the plume. This gives an idea of how the plume has evolved during its journey to the monitoring site. The plume width in the model is calculated using the method explained in subsection 3.6.1. A different method is required for the width of the plumes in the measurements. The two main data points required are the plume arrival time and the plume end time. The plume arrival time is defined as the time when the concentration of the pollutant, either particulate or gaseous, rises above the background level. The time at which the background pollution threshold is exceeded is recorded. Similarly, when the pollution level falls back to background levels, the plume end time is recorded. Subtracting these two times from each other results in the plume duration time as seen in Equation 2.10. An example of the plume arrival and end times can be seen in Figure A.23.

$$T_{duration} = T_{end} - T_{start} \tag{2.10}$$

Equation 2.10 allows for the next step to be taken to calculate the plume width. The plume is perpetuated alongside the runway by multiple flows. The velocity around the aircraft is due to its speed as well as the velocity it gains from the combustion process in the jet engine. Perpendicular to the

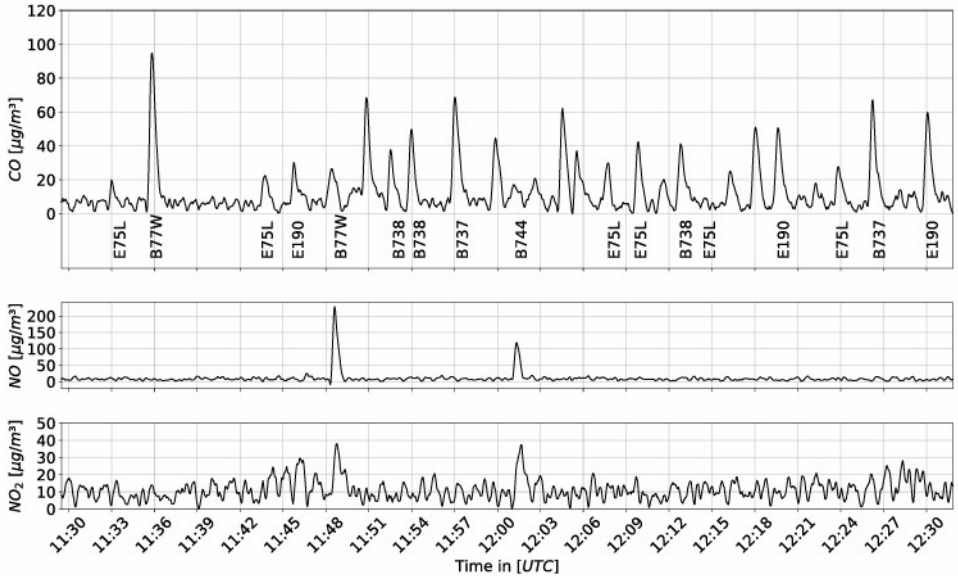

Figure 2.4: Time series plot containing plumes matched to the aircraft, part of the thesis of Rik Goudswaard [22]

runway, only one thing is affecting the plume; this is the crosswind component of the ambient wind. This means that the plume width can be calculated by multiplying the crosswind component and the plume duration time, shown in Equation 2.11. Here β is the wind angle in relation to the runway. U_{wind} is the ambient wind speed.

$$W_{plume} = sin(\beta) * U_{wind} * T_{duration} \tag{2.11}$$

2.12. Statistical Methods

Throughout this thesis, several statistical methods will be used to analyse and observe the type of relationships seen in the data. These methods will be discussed in this section.

2.12.1. Paired t-test

The paired t-test is used to compare the means of two related data sets - in this case, the model predictions and the experimental observations - to determine whether there is a statistically significant difference between them. This test is particularly useful when each experimental observation has a corresponding model prediction, ensuring the comparisons are directly matched—the paired t-test tests whether the mean difference between these paired observations is significantly different from zero. The formula for the paired t-test is seen in Equation 2.12.

$$t = \frac{\bar{d}}{s_d/\sqrt{n}} \tag{2.12}$$

The different variables are as follows:
- $\bar{d}$ is the mean of the differences between the paired observations ($d_i = y_i - \hat{y}_i$)
- s_d is the standard deviation of the differences d_i
- n is the number of pairs.

The steps involved include calculating the difference between each pair of observed (y_i) and predicted ($\hat{y}_i$) values, finding the mean and standard deviation of these differences, and then using these statistics to calculate the t-value. This t-value is then compared with the critical value from the t-distribution table for $n - 1$ degrees of freedom to determine the p-value, which indicates whether the differences are statistically significant.

This study uses the paired t-test to assess whether the discrepancies between the model predictions

and the experimental results were statistically significant. This test helps to confirm the model's validity by identifying whether any observed differences are due to random variation or represent a systematic bias in the model's predictions.

2.12.2. Root Mean Square Error

The Root Mean Square Error is the first statistical variable to validate the model. The Root Mean Square Error (RMSE) is used to quantify the average size of the differences between the values predicted by the model, in this case, the COMSOL model, and the values observed in the experiments at Schiphol. The RMSE is particularly sensitive to large errors because it squares the residuals before averaging them, giving more weight to more significant discrepancies. Therefore, it should be critically assessed as the sensors' data can also show large measurement discrepancies. This metric helps understand how well the model can replicate the variation in the experimental data and highlights areas where the model may be significantly out of line with actual observations. In this thesis, the RMSE was calculated for each set of conditions using the formula seen in Equation 2.13

$$\text{RMSE} = \sqrt{\frac{1}{n}\sum_{i=1}^{n}(y_i - \hat{y}_i)^2} \tag{2.13}$$

In Equation 2.13, different variables can be seen starting with n, which is the number of observations, y_i represents the observed experimental values, and $\hat{y}_i$ denotes the model's predicted values. The number of observations is shown with n.

2.12.3. Mean Absolute Error

The Mean Absolute Error (MAE) measures the average size of the errors between the model predictions and the experimental data, regardless of the direction of the errors. Unlike the RMSE, the MAE does not square the residuals, making it less sensitive to outliers and providing a simpler interpretation of the average error size. This metric is particularly useful for getting a general sense of the model's accuracy in a more interpretable and less biased way. In this analysis, the MAE was calculated using the formula:

$$\text{MAE} = \frac{1}{n}\sum_{i=1}^{n}|y_i - \hat{y}_i| \tag{2.14}$$

where n is the number of observations, y_i is the observed experimental values, and $\hat{y}_i$ is the predicted values from the COMSOL model. This formula provides insight into typical prediction errors and guides further refinement to improve model accuracy.

2.12.4. Bland-Altman Analysis

The next statistical method used is the Bland-Altman analysis. This analysis is used to assess the agreement between the simulations and the results from the model. A Bland-Altman plot is created by plotting the differences between the simulations and the experiments against their averages. There are several steps to take to execute this analysis.

- *Calculating the Differences*: The first step in creating a Bland-Altman Plot is to calculate the differences between the simulations and experiments. This is shown in Equation 2.15. Here X_i is the value from the simulation, and Y_i is the value from the measurements.

$$\text{Difference}_i = X_i - Y_i \tag{2.15}$$

- *Calculating the Averages*: The next step is to calculate the averages. Each pair's average is calculated using a measurement and a subsequent simulation. As seen in Equation 2.16.

$$\text{Average}_i = \frac{X_i + Y_i}{2} \tag{2.16}$$

- *Mean Difference (Bias)*: In the first step the differences were calculated. These are averaged to determine the bias of the model. The variable n shown in Equation 2.17 represents the number

of measurement and simulation pairs.

$$\text{Mean Difference}(\overline{d}) = \frac{1}{n}\sum_{i=1}^{n}(X_i - Y_i) \tag{2.17}$$

- *Standard Deviation of the differences*: The standard deviation is calculated to help assess the spread. This is done in Equation 2.18.

$$\sigma_d = \sqrt{\frac{1}{n-1}\sum i = 1^n((X_i - Y_i) - \overline{d})^2} \tag{2.18}$$

- *Limits of Agreement*: In the analysis there a limits set. These limits are typically set at the mean difference plus and minus 1.96 times the standard deviation. This is done to obtain a 95% confidence interval, or in other words, to contain 95% of the measurements' differences. The limits are calculated in Equation 2.19 and Equation 2.20.

$$\text{Upper Limit of Agreement} = \overline{d} + 1.96 \times \sigma_d \tag{2.19}$$

$$\text{Lower Limit of Agreement} = \overline{d} - 1.96 \times \sigma_d \tag{2.20}$$

Interpretation of the Bland-Altman plot involves examining the horizontal axis, which represents the average of the measurement and simulation for each pair, and the vertical axis, which represents the difference between the simulation and measurement for each pair. The plot includes a mean difference line, a horizontal line at the mean difference value, limits of agreement lines, and two horizontal lines at the upper and lower limits of agreement.

2.12.5. Linear Regression

The final statistical method used is linear regression. This technique models and analyses the relationship between a dependent variable and one or more independent variables. The goal is to establish a linear equation that best predicts the dependent variable based on the values of the independent variables. In this case, the dependent variable will be the characteristics of the plume, such as the width or the peak concentration. The independent variable can be any ambient or operational variable.

Linear regression models to say it simply model the relationship between a dependent variable y and a single independent variable x using Equation 2.21:

$$\hat{y}_i = \beta_0 + \beta_1 x_i \tag{2.21}$$

In Equation 2.21, the following variables are found. First is $\hat{y}_i$, which is the predicted value of the dependent variable for the i-th observation. x_i is thehe independent variable for the i-th observation. The intercept of the regression line is denoted with β_0, and β_1 is the slope of the regression line. For this thesis, only the single independent variable method is used.

Least Squares Method

The least squares method estimates the parameters (β_0, β_1, of the linear regression model by minimizing the sum of the squared differences between the observed and the predicted values. These differences are called residuals. For each observation, i, the residual, e_i, is calculated using Equation 2.22. The sum of the residuals must be minimized, this is done in Equation 2.23.

$$e_i = y_i - \hat{y}_i \tag{2.22}$$

$$S(\beta_0, \beta_1) = \sum_{i=1}^{n} e_i^2 = \sum_{i=1}^{n}(y_i - (\beta_0 + \beta_1 x_i))^2 \tag{2.23}$$

Coefficient of Determination

The coefficient of determination, denoted R^2, is an important measure in linear regression. This parameter quantifies the proportion of the variance in the dependent variable that is predictable from the independent variable. It is calculated as seen in Equation 2.24.

$$R^2 = 1 - \frac{SS_{\text{res}}}{SS_{\text{tot}}} \tag{2.24}$$

The variable SS_{res} is the sum of squares of the residuals calculated in Equation 2.25. The other variable SS_{tot} is the total sum of squares with $\bar{y}$ being the mean of the observed values, as seen in Equation 2.26.

$$SS_{\text{res}} = \sum_{i=1}^{n}(y_i - \hat{y}_i)^2 \tag{2.25}$$

$$SS_{\text{tot}} = \sum_{i=1}^{n}(y_i - \bar{y})^2 \tag{2.26}$$

Calculating the coefficient of determination, R^2, is possible using all these equations. A value of R^2 close to one indicates that the linear regression has managed to find a good fit. A good fit means that a stronger argument can be made about the effect of an ambient or operational variable on the model or measurements. The relationship between the variables can be seen by β_1; if the sign is positive, the relationship is positive and vice versa. Similarly, a larger value of β_1 means that the model found that the independent variable studied severely influenced the simulation or measurement data.

3 Model

This chapter will introduce the COMSOL Multiphysics software and its application in making a model to simulate the aircraft jet plume. COMSOL Multiphysics is a computational modelling tool that enables engineers to simulate and analyse multiphysical phenomena across various disciplines. The theory behind COMSOL is based on finite element methods, which break complex geometries into smaller elements, enabling numerical simulations of physical phenomena by solving governing equations across these elements. This chapter will provide an overview of the capabilities of the COMSOL model. The different variables used will be discussed, as well as the domain in which the jet plume is simulated. All the assumptions made will be clarified, and the identification method for extracting the plume will be explained. In addition, a sensitivity analysis will be done. Here, the effect of various operating and ambient conditions will be studied to understand their impact on plume evolution and, thus, the dispersion of pollutants.

3.1. Domain

In COMSOL Multiphysics, the domain refers to the space or region where the simulated phenomena occur. It defines the boundaries and geometry of the system under study. This foundation is essential as it provides the framework for specifying properties and boundary conditions. Therefore, accurately defining the domain is crucial in creating effective results for the model. The domain must represent the experimental setup used to gather the emission data from the aircraft. Most of the data has been measured at the Polderbaan (180R - 360L) at Schiphol. In Figure 3.1, it can be seen that this runway is positioned at the top left of the airport, which means it is relatively isolated compared to other runways.

Figure 3.1: The layout of the runways at Schiphol Airport, including the Polderbaan [3]

Now that it is determined which runway is used as a base, it is possible to zoom further into what

the domain consists of. As individual aircraft plumes are analysed and a single runway is considered logical, the next step would be to use this as a starting point. The location of the measurement station at the Polderbaan is 190 meters perpendicular to the runway's centre line. This can be seen in Figure 3.2, where the aircraft can be seen taking off.

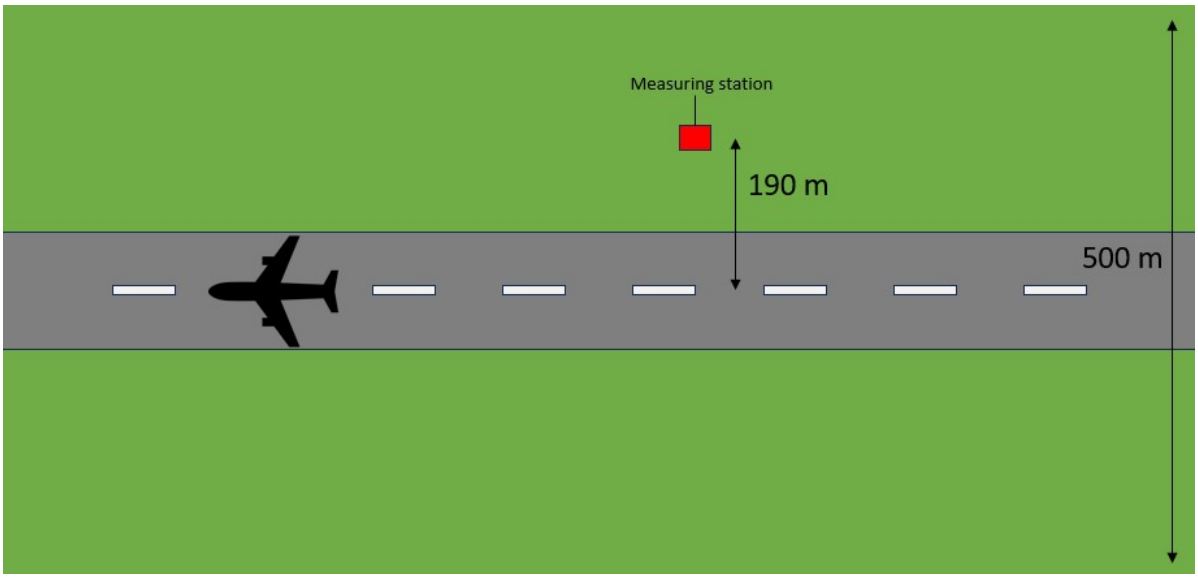

Figure 3.2: A schematic representation of the Polderbaan and the measurement station at Schiphol Airport

Due to the distance between the runway and the measurement equipment, a first sense of what the domain size must be can be concluded. In order to create some margin between the measuring station and the end of the domain, a width of 250 meters was chosen. To account for plume effects that might occur at the other half of the runway, the entire width is set at 500 meters as is seen in Figure 3.2. The length of the area that is researched heavily depends on the ambient conditions and is therefore not set at a specific number; for example, a higher crosswind would result in the plume arriving faster at the measurement station, thus needing a shorter length.

3.1.1. Boundary Conditions

Now that the rough size of the domain is constructed, it is essential to define its boundary conditions. Properly defining boundary conditions ensures that the simulation accurately represents the LTO cycle of an aircraft. Since the flow of the plume is modelled, there are assumptions about what the flow can and cannot do when entering or exiting the domain. In section 3.1, a first estimate of the size of the domain was proposed; this has now been translated into COMSOL, which can be seen in Figure 3.3. The grey area is the area from which the jet plume is simulated, and eventually, concentrations can be extracted.

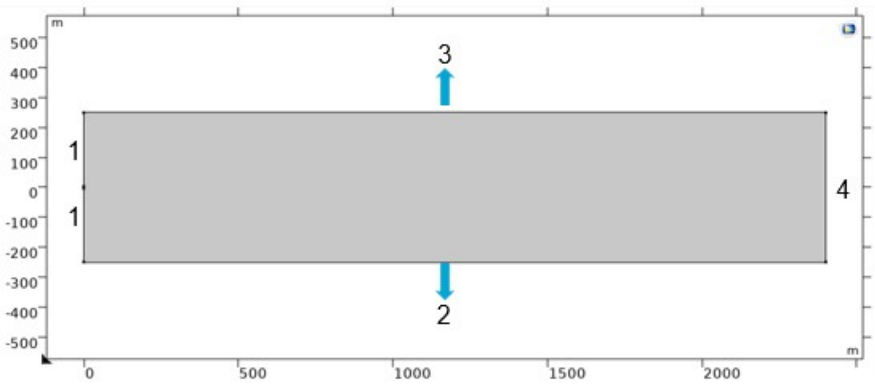

Figure 3.3: The domain in COMSOL with the different boundaries labelled

In Figure 3.3, four different boundaries are numbered, each with specific conditions to simulate the plume accurately. The different boundaries are defined as follows:

1. *Free flow edge*: This boundary means that air can freely flow into the system with a specific temperature, pressure and velocity. When comparing this to a real-life situation, this edge is mostly used to feed air into the system because of the speed at which the aircraft is moving. In addition, the ambient wind component can also be fed into the domain using this edge
2. *Free flow edge*: Free flow edge: Similar to boundary one, this edge is also a free flow edge. Air can also flow freely; however, in comparison with edge 1, this edge is mostly used to incorporate the crosswind that is blowing across the runway.
3. *Outlet*: Here, the air can exit the domain; no air can enter it again after it has left. It is also important to mention that this edge does not act as a wall so that no flow can be bounced around. Most of the time, the jet plume exits the domain using this edge.
4. *Outlet*: Similar to 3, this boundary also serves as an outlet. Ambient wind, as well as the plume, can exit the domain here.

The left side of the domain is also where the jet inlets are positioned. Therefore, it is also relevant to zoom in on that side. Two different boundaries are defined in Figure 3.4.

1. *Free Flow Edge*: Similar to the free flow edge in Figure 3.3, here it is also made clear that there is a flow of air between the two inlets. Here, the airflow due to the aircraft's speed is considered.
2. *Jet inlet*: The airflow from the jet engines can enter the domain here. In addition, the pollutants are emitted through this flow.

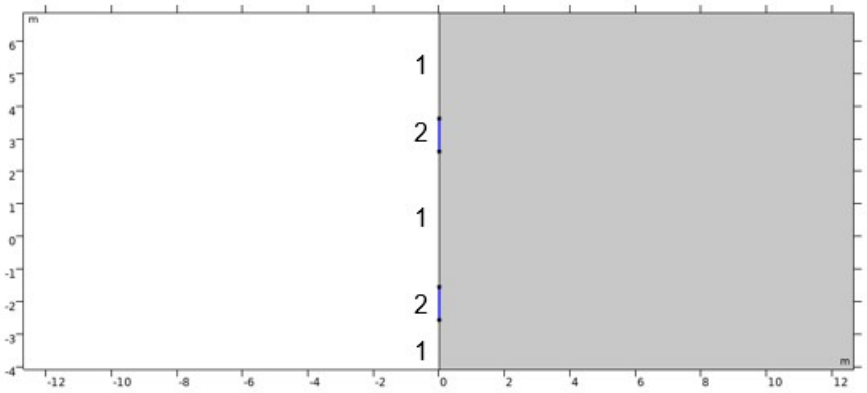

Figure 3.4: The zoomed-in domain in COMSOL with position of the jet inlets

3.2. Flow Properties

A flow in COMSOL needs to be modelled according to specific key characteristics. These characteristics govern the properties and assumptions that simplify the flow, allowing for a simulation. When assessing the flow of the jet engine, there are two main parts into which the flow can be divided: the high Mach number flow and the transport of diluted species. The high Mach number flow consists of the velocity and temperature profiles as well as how the shape of the plume is affected by the ambient and operational conditions. The transport of diluted species governs how the pollutants are dispersed in the plume of the jet engine. These two aspects of the plume contain many different parts and are discussed in the following sections.

3.2.1. High Mach Number Flow

The flow simulation in COMSOL is done through a High Mach number flow model, which is characterised by fluid velocities that approach or exceed the speed of sound. In aerodynamics, Mach numbers greater than approximately 0.3 Mach indicate supersonic flow regimes, where the flow velocity starts to approach the speed of sound. This is in line with the modelling approach of COMSOL, which states

that velocities around 0.3 Mach need to use said flow type [14]. The speed with which the air exits the jet engine heavily depends on the thrust applied and the maximum thrust level of the jet engine. More on this in subsection 3.3.1 variables.

High Mach number flows are known to be compressible, which means that changes in density due to pressure variations occur, unlike in low Mach number flows where the flow is typically treated as incompressible. In COMSOL, the high Mach number flow model incorporates compressibility effects. While COMSOL mentions compressibility effects in their high Mach number flow, other sources indicate that compressibility only occurs at speeds higher than Mach 1 [46]. Since the aircraft is considered to be of a subsonic nature, this does not play a significant role in the results.

In addition to compressibility, another aspect plays a role. This is the isentropic relation, which describes the thermodynamic properties of high-speed flows in a simplified manner. This relation is built on a few assumptions. The first is that the flow is adiabatic, and there are no irreversibilities in the plume. This means that no heat transfer takes place and no phenomena such as shock waves occur. Assuming that the flow is isentropic, it allows for a method of calculating the total air pressure and temperature, more on this in subsection 3.3.1.

Spalart-Allmaras Model

A turbulence model is crucial to fully implementing a model simulating a jet plume. A turbulence model is a mathematical framework used in computational fluid dynamics, and thus also in COMSOL, to simulate the behaviour of turbulent flows. Turbulence refers to the chaotic complex motion of fluid particles characterised by fluctuations in velocity, pressure, and other flow properties. Unlike laminar flow, where fluid motion is smooth and orderly, turbulent flow involves irregular turbulent shapes called eddies and vortices at various scales.

There are different categories into which turbulence models can be divided. One of these categories is RANS Modelling. RANS modelling stands for Reynolds-Averaged Navier Stokes. Based on these models, the theory is that the Navier-Stokes equations are, as the name suggests, Reynolds-averaged. The Navier-Stokes are a complex set of equations. These equations describe how various properties such as a fluid's velocity, pressure, temperature, and density interact [45]. Due to these equations' complexity, reducing and simplifying them is desirable. This is done through Reynolds-Averaging. This method is built upon the separation of the time-varying variables. It simplifies the equation by averaging the fluctuations over time, focusing on characteristics like mean flow and pressure. This results in less computational complexity [59].

There are different types of turbulence models to choose from within RANS modelling. The COMSOL model is the Spalart-Allmaras turbulence model. Philippe Spalart and Steven Allmaras developed the model in the early 1990s; this one-equation turbulence model is mainly known for its applicability to a wide range of flow regimes, including attached and separated flows, transitional flows, and even supersonic flows [34]. One key difference between more complex turbulence models that solve multiple transport equations is that the Spalart-Allmaras model simplifies the turbulent flow problem by focusing on the turbulent viscosity alone. Therefore, the model can be seen as a one-equation model. For example, this gives it a computational cost advantage compared to the k-ϵ model. The equation that the model is built on is shown in Equation 3.1.

$$\frac{\partial \hat{\nu}}{\partial t} + u_j \frac{\partial \hat{\nu}}{\partial x_j} = c_{b1}\left(1 - f_{t2}\right)\hat{S}\hat{\nu} - \left[c_{w1} f_w - \frac{c_{b1}}{\kappa^2} f_{t2}\right]\left(\frac{\hat{\nu}}{d}\right)^2 + \frac{1}{\sigma}\left[\frac{\partial}{\partial x_j}\left((\nu + \hat{\nu})\frac{\partial \hat{\nu}}{\partial x_j}\right) + c_{b2}\frac{\partial \hat{\nu}}{\partial x_i}\frac{\partial \hat{\nu}}{\partial x_i}\right] \quad (3.1)$$

The goal of Equation 3.1 is to calculate the $\hat{\nu}$ or the turbulent viscosity. In the equation, t is time and x_j and v_j are the spatial coordinates and velocity components, respectively. The variables c_{b1}, f_{t2}, f_w and c_{w1} a e model constants provided by COMSOL. The rate of strain tensor is denoted with $\hat{S}$; this variable describes the stretching of the fluid analysed. The variable d is the smallest distance from the field point to the nearest wall. The Von Karman constant is shown with κ.

The reason for choosing this turbulence model is mainly focused on the domain in which the measurements and, thus, the simulations take place as shown in section 3.1. This domain includes the runway and a particular area around it. Combining this leads to a significant area. The larger this area, the longer it takes for the simulation to compute. Choosing one equation turbulence model decreases the c computation time. This could lead to less accurate simulations. However, the domain can also be considered relatively simple. The area is considered flat and rural. No objects interfere with the flow except the ambient wind. Therefore, this model will suffice.

3.2.2. Transport of diluted species

Now that the type of flow has been described, the next part of the plume can be discussed. This is the transport of diluted species. In Comsol, this module is designed to simulate the transport and dispersion of various species, such as pollutants or chemical species, within the fluid domain or, in this case, the runway area. For this module, two ways of transportation were chosen. The e are diffusion and convection.

Transport through diffusion is based on a difference in concentration. This concentration difference fuels the energy needed for transport. To model this type of transport, several diffusion coefficients are required. These coefficients describe how quickly a particular pollutant will disperse in certain gasses; that would be fair in this case. The coefficients for the pollutants considered can be found in Table 3.1. It is important to note that the coefficients are also influenced by temperature and pressure, so this table is just an example of how the coefficients could look. The coefficients are often the subject of new studies and can be calculated through different methods; thus, they are always up for discussion. For these, a review study of Massman et al. has been used [39].

Diffusivity in Air for various pollutants	CO	NO	NO_2
Diffusion Coefficients ($cm^2 s^{-1}$)	0.1807	0.1988	0.1361

Table 3.1: The different diffusion coefficients for pollutants in Air at 20°

The module is based on equations that can be seen in Equation 3.2 and Equation 3.3. The set of equations is mainly built around the conservation of mass principle. The variable $\frac{\partial c_i}{\partial t}$ represents the rate of concentration (c_i) of species i with respect to the time, t. This variable is needed when modelling a time-dependent study. $\nabla \cdot \mathbf{J}_i$ is the divergence of the flux of species i. The concept of flux in this method can be seen as the rate of flow of a pollutant species through a surface. The variable thus measures how much the flow diverges or converges; if the flow diverges, the flux is seen as positive and, of course, vice versa. The next variable, $\mathbf{u} \cdot \nabla c_i$, accounts for the advection of species i by the velocity field $\mathbf{u}$. R_i represents all the sources and sinks of pollutant i, in other words, the jet engines and the domain outlets. In Equation 3.3, the flux is further defined. $-D_i \nabla c_i$ consists of two components. $-D_i$ is the diffusion coefficient of species i, as mentioned in Table 3.1. While ∇c_i is the concentration gradient of species i. This equation is also known as Flicks'law, which describes the movement of particles from a higher concentration to a lower concentration and is directly related to the concentration gradient of, in this case, the pollutant [61].

$$\frac{\partial c_i}{\partial t} + \nabla \cdot \mathbf{J}_i + \mathbf{u} \cdot \nabla c_i = R_i \tag{3.2}$$

$$\mathbf{J}_i = -D_i \nabla c_i \tag{3.3}$$

In addition, Transport through convection is modelled. This refers to the movement of substances due to bulk motion or flow. In this process, particles are carried along with the moving fluid, leading to the transfer of mass momentum from one location to another. The mechanism of convection involves the transfer of heat or mass through the movement of fluid particles driven by temperature or concentration gradients. This means that the different species are dispersed because of the high-velocity flow exiting the jet engine.

One aspect that is not included in the transport of diluted species is the chemical evolution of the plume. When pollutants are emitted from the engine, they react with the ambient air, which alters the concentration balance in the plume itself. For example, NO_x concentrations would initially be high directly from the engine. However, this decreases as the pollutant oxidises with the surrounding air, causing a significant drop in concentration [35].

3.3. Variables

In this section, the different variables that are used in the COMSOL model will be discussed. The variables can be seen as the model's input parameters and, therefore, greatly impact the outcome of the results. The model consists mainly of three types of variables:

- **Aircraft Specific**: These variables describe the operational conditions of the aircraft. These include the geometry of the jet engine and the parameters describing the flow and velocities that govern the engines' thrust. The variables responsible for the emissions of pollutants are also included in this category of variables. The aircraft-specific variables allow for an extensive comparison of different types of aircraft that are taking off and departing Schiphol Airport.
- **Ambient Conditions**: The second category are the ambient conditions. These are mainly meteorological factors that allow for a representation of the atmospheric state at the time that is specific to the conditions of the measurement. These variables impact not only the plume evolution but also the accuracy of the sensors used and are, therefore, of great importance.

3.3.1. Aircraft Specific

The aircraft-specific variables are described here. The units of the variable are also specified. Also, where these variables can be found is discussed.

- **Engine Diameter** $[m]$: The engine diameter specifies how wide the aircraft engine is that is being modelled. The diameter is shown in Figure 3.5; here, it can be seen that the two outmost points from the exit diameter of the aircraft engine are considered. It is important to consider the exit diameter as the flow contains the pollutants. This data on aircraft can often be found in a database provided by the European Union Aviation Safety Agency (EASA) [19]. Here, the dimensions of aircraft engines by different engine manufacturers can be found.

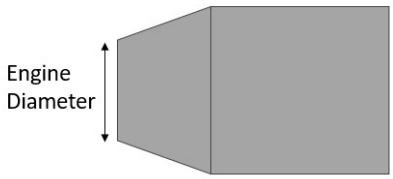

Figure 3.5: The engine diameter visualised with a top view of an aircraft jet engine

- **Engine Separation distance** $[m]$: The engine separation distance specifies how far the engines are from each other. The distance between these two has an impact on how quickly the two plumes merge into one. The exact representation of the variable is shown in Figure 3.6. The origin of both points is in the centre of each of the jet engines. Obtaining this parameter is slightly more complicated than obtaining the engine diameter. Manufacturers do not typically provide these figures, so there is no one way of finding this. For example, a detailed description of the dimensions of an A320 can be found in a modelling paper by Coetzee et al. [13].
- **Aircraft Velocity** $[m/s]$: The aircraft velocity is self-explanatory. This is the speed with which the aircraft moves along the runway. For arrivals, this speed will be lower than for departures. This speed will impact how quickly the plume evolves along the runway and how great the impact will be from ambient conditions such as the wind.

- **Exhaust Air Temperature** $[K]$: Here, the temperature of the air leaving the exhaust is considered. This is needed not only to model the temperature gradient in the flow but also to compute

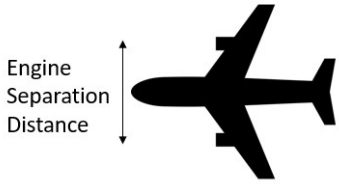

Figure 3.6: The engine separation distance visualised with a top view of the aircraft

the pressure of the flow when it is leaving the jet engine. Also, the temperature must be analysed to determine the air density under these conditions. Similar to the engine diameter information on this variable, it can be found per engine on the (EASA) database.

- **Exhaust Air Pressure** [Pa]: In addition to the temperature, the exhaust air pressure is also taken into account. There is no freely available information on how to obtain this data. Therefore, assumptions must be made to get a relatively accurate pressure that describes the jet engine's flow.

- **Mass Flow Jet Engine Outlet** [kg/s]: The mass flow from the flow exiting the jet engine is needed. This figure becomes the starting point for calculating the jet engine exit speed, which is a significant parameter in the model. An important note is that with the mass flow, not the fuel flow is used, as this parameter is often provided, but the complete mass flow, including the air, is needed. The problem, however, is that these figures are seen as confidential, so while other parameters, such as bypass and pressure ratio, are provided, the exiting mass flow is not. Therefore, it is crucial to take this into account when assessing the results and incorporate this parameter into a sensitivity analysis to quantify its effect on the plume.

- **Jet Engine Exit Speed** [m/s]: The exit speed of the aircraft's engine is, as mentioned, calculated using the mass flow of the engine's outlet. To calculate this parameter, first, the density of air is needed. This is calculated using Equation 3.4. Here, P_e and T_e are, respectively, the pressure and the temperature of the air at the exhaust.

$$\rho = \frac{P_e}{R * T_e} \tag{3.4}$$

When the air density is known, it is possible to calculate the jet engine speed using the area of the jet engine outlet. The area of the jet engine can be computed using the engine diameter (D) and Equation 3.5. This gives the jet engine area denoted with A.

$$A = \pi * (\frac{D}{2})^2 \tag{3.5}$$

Using the engine area (A), the last step can be taken to compute the exit velocity. Based on the air density (ρ). The mass flow at the exit is m_e, and using Equation 3.6, the exit speed of the jet engine can be computed, V_e.

$$V_{exit} = \frac{m_e}{\rho * A} \tag{3.6}$$

In addition to this method, there is another way to get an estimate of the exit velocity. Therefore, this method uses several assumptions and should be used with care. The first estimate is that it assumes that the speed from the jet engine is uniformly spread. This is often not the case, as the air exiting the core is usually higher than the speed leaving the fan section of the engine. It also sets the air density equal to what it would be at sea level. The formula is used in Equation 3.7. The same area of the jet engine is used as in Equation 3.5, denoted with A. $T_{aircraft}$ is the amount of thrust produced by the air raft in N. As mentioned, ρ is the density of air at sea level. Using this equation, it is possible to estimate the exit velocity of the jet engine's air.

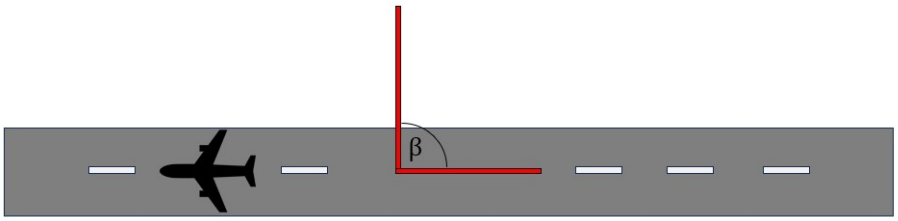

Figure 3.7: The wind angle in relation to the runway

$$T_{aircraft} = \rho * A * V_{exit} \tag{3.7}$$

- **Pollutant Emissions** [$Parts\ Per\ Million$]: This is the input parameter for the amount of pollutants that are 'released' into the plume using the transport of diluted species engine of COMSOL. The units are, in this case, parts per million (ppm). However, the concentration can also be expressed in mol/m^3. This is to be in line with the units that are used for the measurements. The convergence formula is shown in Equation 3.8. Where again the exhaust temperature (T_e) and pressure (T_e) and the ideal gas constant (R_g) which is 8.314 $J/(mol*K)$. The sensitivity analysis will discuss how this can be calculated.

$$C_{mol/m^3} = ppm * \frac{p_e}{R_g * T_e} \tag{3.8}$$

3.3.2. Ambient Conditions

Now that the variables concerning the aircraft have been discussed, the next category is the ambient conditions. The measurements at Schiphol were done on different days and times of the year. This causes a significant change in meteorological circumstances. Therefore, it is necessary to include these conditions in the model.

- **Wind Direction** [deg]: The first variable of the ambient conditions is the wind direction wind direction. The wind direction is transmitted by the METAR station at Schiphol. This station provides the meteorological conditions every half hour, including the wind direction. The angle is translated to the reference frame parallel to the runway, as seen in Figure 3.7. The wind angle is denoted with β.

- **Wind Speed** [m/s]: The METAR station also provides the wind speed at Schiphol. The wind speed, in combination, determines how quickly the plume reaches the measurement station and, thus, how quickly the plume can be seen on the sensors. The wind direction is split up into the part along the runway (x-value) and perpendicular (y-value). This is seen Equation 3.9, U is the wind speed received from the METAR station and the same for the wind angle β.

$$U_{x-wind} = U * cos(\beta), \quad U_{y-wind} = U * sin(\beta) \tag{3.9}$$

- **Speed of sound** [m/s]: Since a high Mach number flow is chosen to represent the jet plume, the speed of sound is needed. Most of the speeds that are input parameters must be done as a Mach number. The formula for this is shown in Equation 3.10. Here γ is the heat capacity ratio, and for air, this is equal to 1.4. The ideal gas constant is again needed, R_g, which is 8.314 $J/(mol*K)$. T is the temperature of the ambient air at the time of the measurement, and M is the molar mass of air 28.9647 g/mol.

$$V_{sound} = \sqrt{\gamma * R_g * T * M} \tag{3.10}$$

- **Corrected wind angle** [deg]: The aircraft is moving at a certain speed along the runway. This causes a deviation in the wind angle when trying to model the flow of air in the domain. This means that not only the wind angle β is needed but also an additional angle α, which incorporates the

velocity of the aircraft. The different velocities are shown in Figure 3.8. Here, it is seen that the velocity of the plane is causing the air to move in the opposite x-direction, causing a deviation. It is important to note that this angle is only needed to model the initial velocity and direction of air that is already in the domain, not the air coming in through the boundaries.

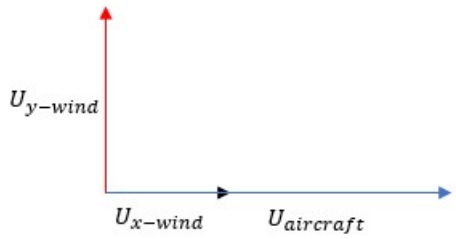

Figure 3.8: A schematic representation of the air velocities in the domain

The angle α can then be calculated by adding the velocities in the x and y direction and taking the arctan as is seen in Equation 3.11.

$$\alpha = \text{arctan}(\frac{U_{y-wind}}{U_{x-wind} + U_{aircraft}}) \tag{3.11}$$

- **Initial air velocity** $[m/s]$: In the last variable, the corrected wind angle was needed for the initial condition of the air that is already in the domain. This air also needs a velocity. Again, the wind velocity and the aircraft's velocity are required for both the x and y directions. The same schematic can be used as in Figure 3.8. An absolute velocity must be calculated and corrected for the speed of sound calculated in Equation 3.12.

$$V_{air} = \frac{\sqrt{U_{y-wind}^2 + (U_{x-wind} + U_{aircraft})^2}}{V_{sound}} \tag{3.12}$$

- **Total Air Pressure** $[Pa]$: The air pressure at the exhaust is a combination of ambient and aircraft conditions; hence, it is placed here. The pressure at the exhaust of the jet engine can be calculated using the isentropic relation. This relationship plays a role when flows start to approach the speed of sound [44]. Therefore, it can be used to calculate the exhaust air pressure. The complete relationship is found in Equation 3.13. The total air pressure is denoted with p_t, and p_e is the pressure at the exhaust of the jet engine. The γ is again the heat capacity ratio. M_{exit} is the velocity at the exit of the exhaust corrected for the speed of sound; this is done in Equation 3.14.

$$\frac{p_t}{p_e} = \left(1 + \frac{\gamma - 1}{2} M_{exit}^2\right)^{\frac{\gamma}{\gamma - 1}} \tag{3.13}$$

$$M_{exit} = \frac{V_{exit}}{V_{sound}} \tag{3.14}$$

- **Total Air Temperature** $[K]$: The same method can be used for calculating the total air temperature. Again, the isentropic relation is used as in Equation 3.13. Equation 3.15 is the relation between the temperature at the exhaust (T_e) and the total air temperature (T_t).

$$\cdot\frac{T_t}{T_e} = \left(1 + \frac{\gamma - 1}{2} M_{exit}^2\right)^{-1} \tag{3.15}$$

3.4. Time-Dependent Study

The type of study used in COMSOL to simulate the plume is a time-dependent study. This type of study involves, as the name suggests, anal zing phenomena that evolve over time. The reason for starting with a time-dependent study is to analyze when the plume becomes fully developed. A fully developed plume is characterised by several properties:

1. **Stable Concentration Pattern**: When the plume reaches its fully developed state, the concentration pattern becomes stable and well-defined. This means that the plume maintains its shape and has clear boundaries which separate the polluted air and the ambient air. Translating this to the model means that the concentration inside the plume converges to a specific shape as time passes.
2. **Reduced Turbulence**: As the plume is further away from the aircraft jet engine, the turbulence within the plume reduces. This is mainly due to the initial kinetic energy from the engine dissipating over time and distance. Therefore, the plume becomes smoother with fewer turbulent fluctuations in velocity and concentration.
3. **Horizontal and Vertical Spreading**: A developed plume spreads both horizontally and vertically as it moves across the domain. The crosswind accounts for the horizontal spread while. Therefore, the wind must have time to play a constant role in the plume's evolution to obtain a steady shape.

The starting point of researching a fully developed plume is to determine the range of time steps over which the plume is simulated. This is done by looking at the data from the measurement. This data contains the time that the aircraft was close to the measuring equipment on the Polderbaan so that it would be directly in front of the sensors. In addition, the time of the plume's arrival is noted. T is when the sensors start to indicate an increase in concentration, marking the start of the plume. A snippet of what the data looks like can be seen in Figure A.2. Using these two-time points, an estimate can be made of what would be an acceptable time range on which to base the study. The difference between the time points indicates how long the plume has to evolve. This leads to the simple equation shown in Equation 3.16, where $t_{arrival}$ is the time when the plume arrives at the measurement station and $t_{closest}$ the time when the aircraft was closest to the sensors.

$$t_{evolution} = t_{arrival} - t_{closest} \tag{3.16}$$

When researching this evolution time through the use of the measurement data, a few key things are noticed. First of all, time is heavily dependent on wind velocity and direction. For experiments with a significant crosswind, for example, 8 m/s, the evolution time lies between 30 seconds and 1.5 minutes. When the crosswind drops to around 3.5 m/s, the evolution time increases to around 3 minutes. This is both for arrivals and departures. The data also includes plumes that arrive after around 6 minutes, so there is a large spread. A range of 0 to 200 seconds is chosen to stay within the average evolution time, as seen in Equation 3.17. This means the plume is simulated until 200 seconds, and each second, the data is outputted; this is not the timestep that is used in the simulation.

$$T_{range} = (0, 1, 200) \tag{3.17}$$

3.4.1. Relative Tolerance

When using a time-dependent study in COMSOL, there is a parameter that plays a crucial role in controlling the accuracy of the simulation. This is the relative tolerance. This parameter governs the permissible level of the relative error in the simulation result compared to the exact solution. The lower the relative tolerance, the higher the computational cost and the accuracy of the simulation will be. For this model, the relative tolerance is set at 0.005, which means that the relative error in the computed solution does not exceed 0.5%. This number was chosen based on COMSOL's suggestion. The program analyses the different physics and domains u ed and then suggests a number.

3.4.2. Plume Visualization

Analysing when the plume is fully developed or not starts with visualisation. When looking at the domain shown in Figure 3.2, a few things can be seen. The plume will be simulated for a total of 200 seconds, and for each second, an output will be generated and stored in the data sets. Now, these data sets cover the entire domain. However, these two surface plots are difficult to compare and analyse and, more importantly, do not entirely explain what needs to be studied. The surface plot can be seen in Figure 3.9. The plume must be assessed at a height of 190 meters from the centre of the runway of the Polderbaan. Therefore, a horizontal line is drawn at 190 meters from the centre and at the same height as the measurement station. This allows for an analysis of the concentration during the different time points at that distance. Figure 3.10 illustrates how the line is setup.

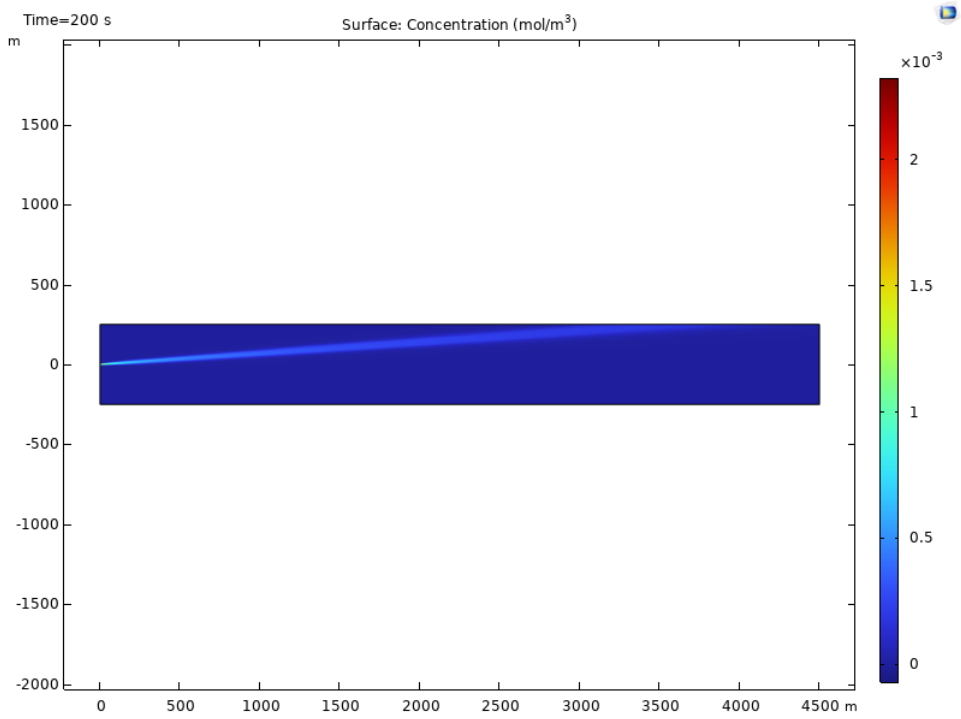

Figure 3.9: Concentration surface plot of the simulated plume

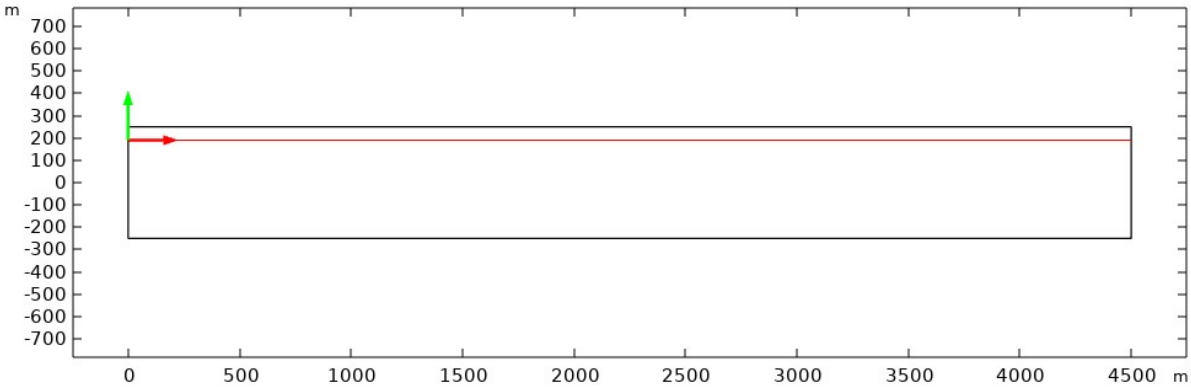

Figure 3.10: The horizontal line drawn in the domain at 190 metres from the centre,

The next step is to simulate the plume for a set of base variables, which can be found in Figure A.1. This simulation is done for the pollutant CO_2 with an input concentration of 200 ppm. The concentration figure does not greatly matter as the geometry of the plume is assessed, not necessarily the values of the concentration. If the plume is simulated for 200 seconds, this results in Figure 3.11

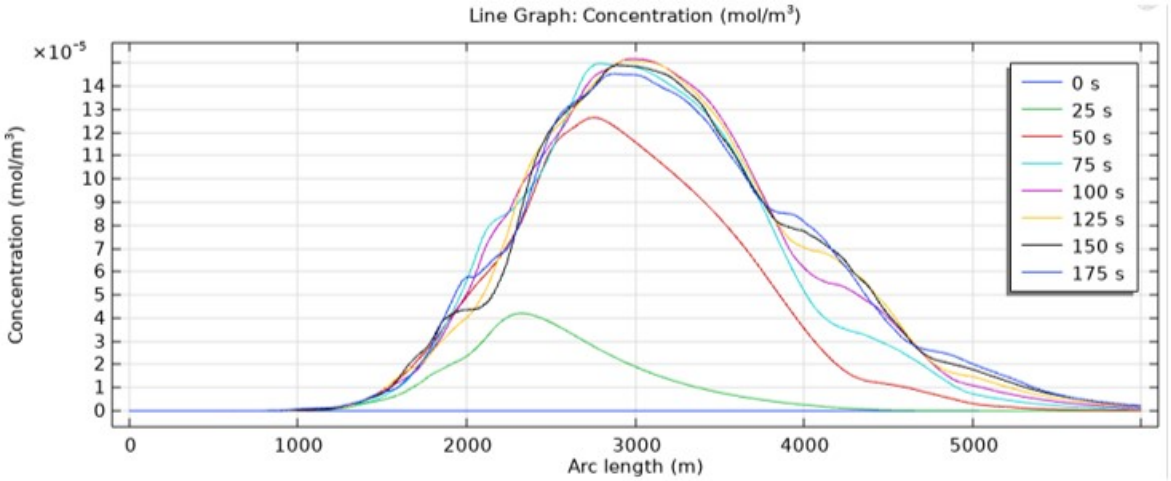

Figure 3.11: The concentration of the plume simulated along the y=190 line for different time steps.

In Figure 3.11, the concentration plume can be seen at the same height as the measuring station. At t=0 seconds, it is seen that the plume has not reached the measuring station, and therefore, the concentration line is equal to 0. This changes after 25 seconds. Here, the first phase of the plume can be seen. A small Gaussian shape is observed. At 50 seconds, the concentration peak is still rising, and the overall shape has become much more significant, indicating that the plume has not yet been fully developed. Looking at 75 seconds, the plume development is approaching a steady state; the changes between the different time points are decreasing and converging to the same peak value. This is confirmed by looking at the plumes from 100 seconds and later. The plume shape does not drastically change, and the peak value can be seen as relatively constant. This also means that after 100 seconds, it does not significantly matter which time point is chosen. To ensure that the simulation also suffices for measurement experiments at low wind speed, when the plume arrival time is larger, the plume is selected to be evaluated at 200 seconds. Therefore, all the plumes extracted from the model will be extracted after 200 seconds.

3.5. Plume Identification

Now that it has been determined that the plume will be simulated for 200 seconds, it is possible to start the methodology on how the plume can be identified. Identification is meant to accurately depict the cross-section of the plume that passes the measurement station.

3.5.1. Plume starting point

The plume starting point is essential as this defines from what point the plume in the simulation can be seen as present. The beginning for this is the plume using the horizontal cross section at 190 meters shown in Figure 3.12 known as the 'raw plume'. Looking at this figure, a few things can be seen. The width of the plume is enormous, around 2000 metres. This indicates that this is not the correct way of dissecting the plume. The cross-section that most accurately visualises how it passes the sensors is likely to be a vertical cross-section.

The raw plume, however, needs to be identified when it first crosses the 190-meter mark, which indicates when it has reached the sensors. This value along the arc length becomes the starting point where a new cross-cross section can be created. To understand what the beginning of the plume is, a threshold must be constructed. This threshold marks the start of the plume. As can be seen from Figure 3.12, this threshold must be a concentration value. The method must be used on every plume; thus, it needs to be relative to the maximum value of the plume. The maximum can be used to calculate a threshold. When the plume has reached a percentage of the plume's maximum, this can be used as a benchmark. The percentage needs to be chosen somewhat arbitrarily and using more qualitative than quantitative reasoning. The measurement equipment used is heavily affected by the background pollution, while the methods used by Jeff in a previous thesis tried to completely isolate an aircraft pollution plume from a background pollutant plume; this is not a simple task [38]. The starting domain

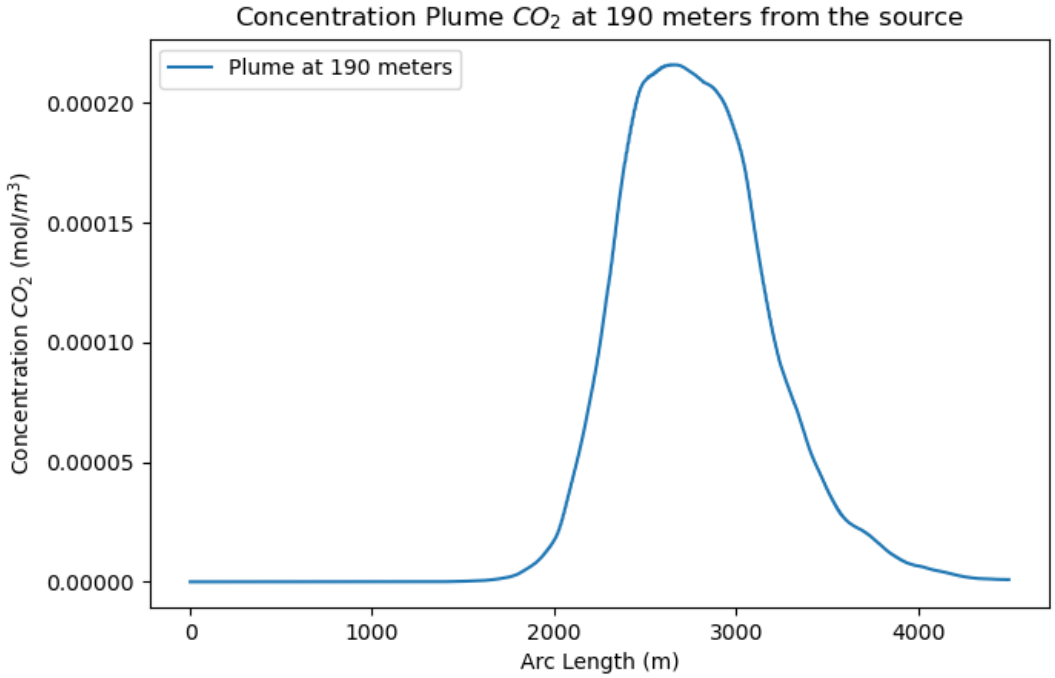

Figure 3.12: The horizontal cross-section of the plume.

for the COMSOL model can be seen as completely clean air. Therefore, setting a tiny percentage of the maximum concentration as the starting point of the plume would be unfair when looking at the conditions of the experiments. Thus, the percentage is set at 2.5%. The threshold calculation can be seen in Equation 3.18.

$$C_{threshold} = 0.025 * max(C_{plume}). \tag{3.18}$$

The starting point of the plume at the arc length is when this threshold concentration is reached. Using interpolation, the point along the arc can be calculated. Interpolation is used because often, no value on the concentration line is exactly 2.5% from the maximum. This is done using the $SciPi$ package in Python. When the interpolation process is finished, this results in Figure 3.13. The threshold concentration value is reached at the red dot. The arc length at this point is equal to 1849 meters. This value is used to identify the plume further.

3.5.2. Point and Direction

The starting point of the plume has been determined and can be used to evaluate further the plume's cross-section. The different cross-sections are extracted using a function built into Comsol called the 'Point and Direction'. This function requires two input parameters: a point through which the line passes and a direction. This direction can be seen as an angle given to the line. The fact is set as the starting point of the plume determined in section 3.5. Determining the direction requires a different method. The method is built on the corrected wind angle, α, described in subsection 3.3.2. The corrected angle is built on the speed of the aircraft and the ambient wind speed. These two factors greatly influence how quickly the plume 'bends' towards the measurement station. To create similar plots for plumes that are subjected to different aircraft and wind speeds, the line plot must be drawn perpendicular to the plume. This is shown in Figure 3.14. The red line along the plume indicates the direction which must be taken into account when extracting a perpendicular plume. The red line that crosses the plume is perpendicular towards its counterpart and illustrates that along this line, the plot must be created.

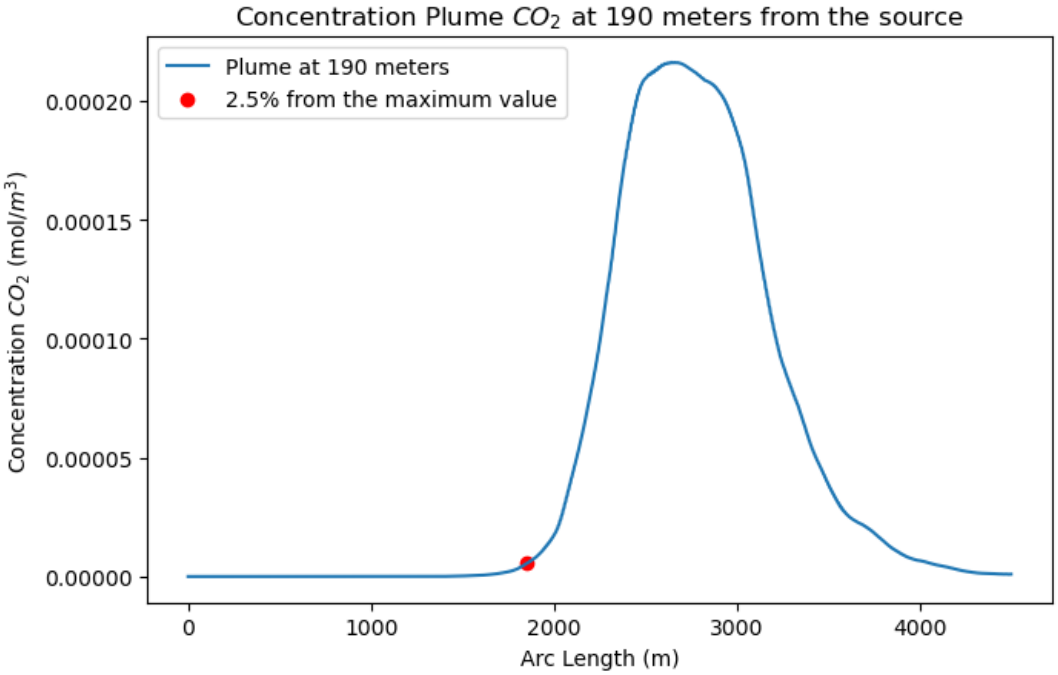

Figure 3.13: The start of the plume marked with the red circle

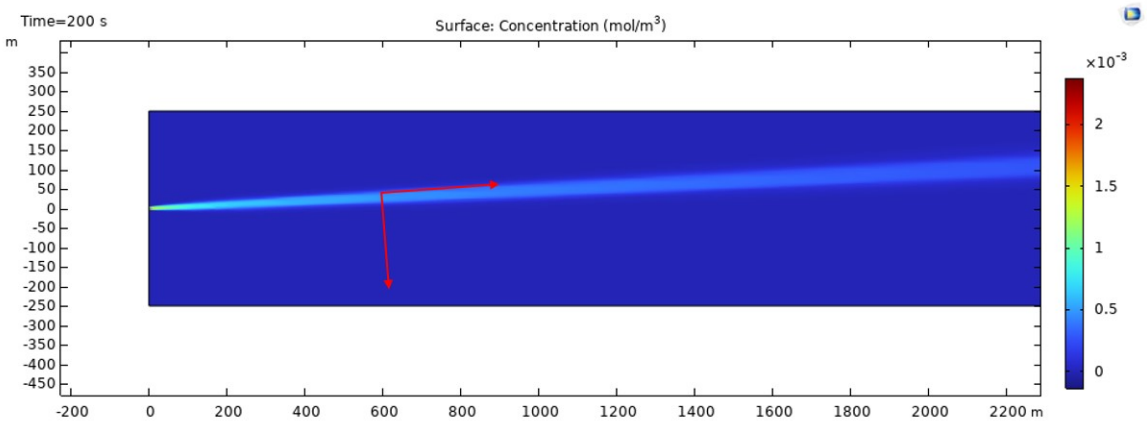

Figure 3.14: The plume direction visualised for the extraction of the line plot

The direction is, as mentioned, computed using the corrected wind angle α. The direction needs to be quantified in both the x and y directions in Comsol. This is done using Equation 3.19 and Equation 3.20.

$$x_{direction} = \cos(\alpha - \frac{\pi}{2}) \tag{3.19}$$

$$y_{direction} = \sin(\alpha - \frac{\pi}{2}) \tag{3.20}$$

The factor $\frac{\pi}{2}$ is used to create the perpendicular aspect. Now that both the point and direction of the line plot are constructed, it is possible to develop the plot with the new plume. This is done in Figure 3.15. The plume here is seen to have a width of about 150 metres and a relatively flat concentration peak.

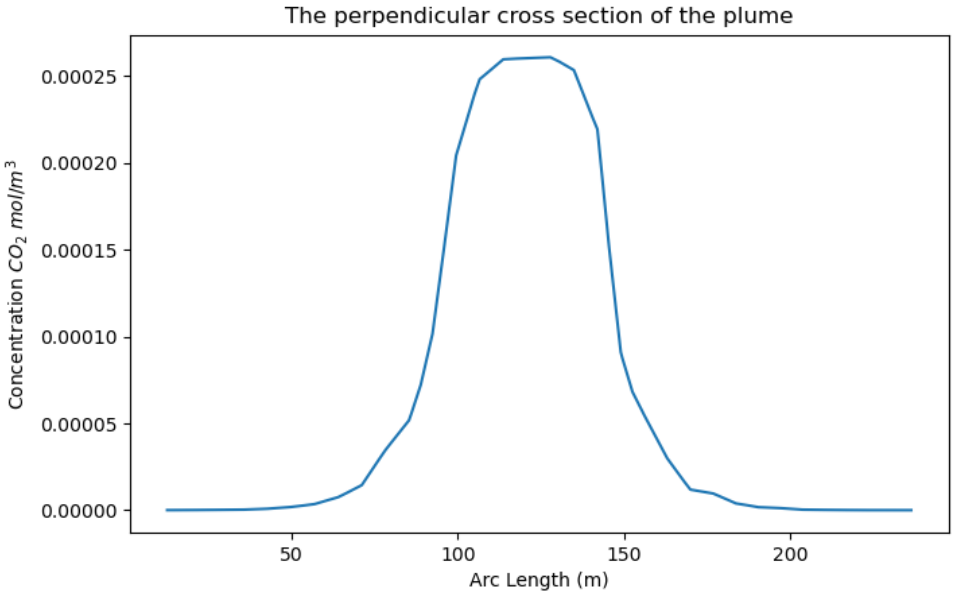

Figure 3.15: The plot created perpendicular to the edge of the plume

Now, this plume can be compared to the raw plume that was used until this point, shown in Figure 3.12. Figure 3.16 shows this. The newly created plume is shifted towards the middle of the raw plume to create a better illustration of the differences between the plumes. The first thing that is noticed is that the horizontal raw' plume is much wider than its counterpart. Around 2000 metres versus 150. As a result, the area of the raw plume is much larger. Also, the peak value of the perpendicular cross-section is higher due to the way of extracting the middle of the plume being closer to the jet engine inlet, thus containing a higher concentration gradient. The perpendicular cross-section will be used for further analysis.

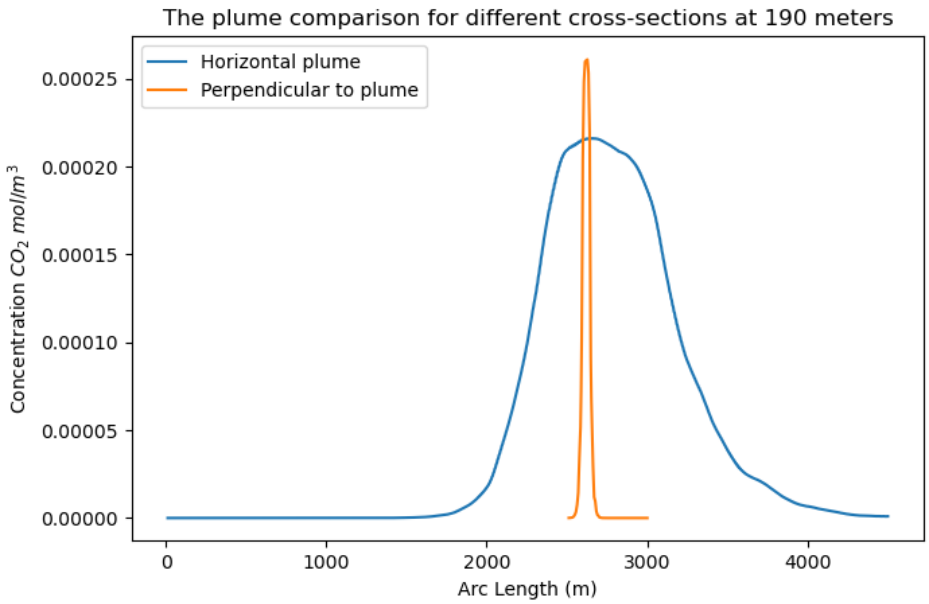

Figure 3.16: The different cross sections of the plume compared

3.6. Plume Analysis

Now that the plume cross section has been constructed, the next step can be taken. That is to identify characteristics of the plume that can be used for further analysis and comparison with the results from the measurements. A plume is considered that will be used for the rest of his section to illustrate how the method for analysing will be set up. This plume is seen in Figure 3.17.

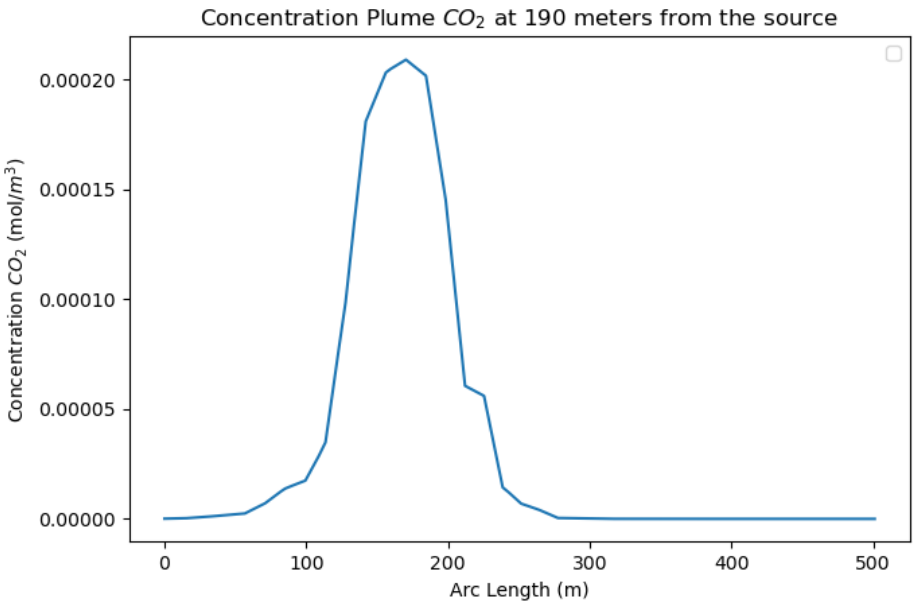

Figure 3.17: The starting plume used for further analysis

3.6.1. Plume Width

One aspect of the plume that can be used to compare plumes from simulations and measurements is the width. This is based on whether the model can accurately model the dispersion of pollutants and the evolution of the plume. If the width of the plumes from the simulation and the measurements differ significantly, this could explain why the concentration values differ. A more enormous plume would lead to a lower peak concentration value. If the plume widths were similar but the concentration values differed significantly, this would indicate that the input parameters surrounding the concentration values would need to be reviewed. Now, to determine the plume's width, the plume's beginning and end points must be computed. This is done in the same way as was done for the starting point. The start of the plume is set at the moment when the concentration reaches 2.5% of the maximum value, and the ending is set at the same point but then after the peak. The formula for the width is seen in Equation 3.21. The length of which the concentration reaches 2.5% after the peak ($L(C_{end})$) is subtracted with the starting point ($L(C_{start})$).

$$L_{width} = L(C_{end}) - L(C_{start}) \tag{3.21}$$

The plume width is visualised in Figure 3.18. The area marks both the start and the ending of the plume, which will used in the comparisons.

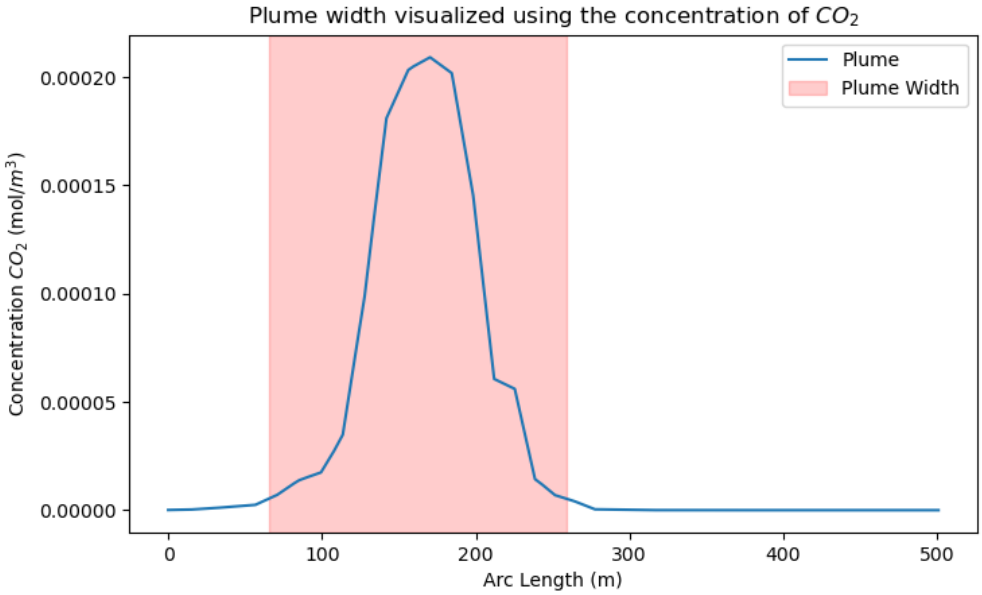

Figure 3.18: The plume width used for analysis is shown within the plot.

3.6.2. Maximum Concentration

In addition to plume width, another aspect needs to be considered. This is the maximum concentration value. This value can be used to assess whether the model can accurately model the pollutants' dispersion and whether the methods for calculating the input parameters regarding the pollutants are without flaws. The maximum can simply be used through a Python command which is marked in the plot, shown in Figure 3.19. The maximum value is a critical value in the model and, therefore, is prone to numerical inaccuracies inherent to the model's method, such as the relative tolerance and the mesh chosen for the domain.

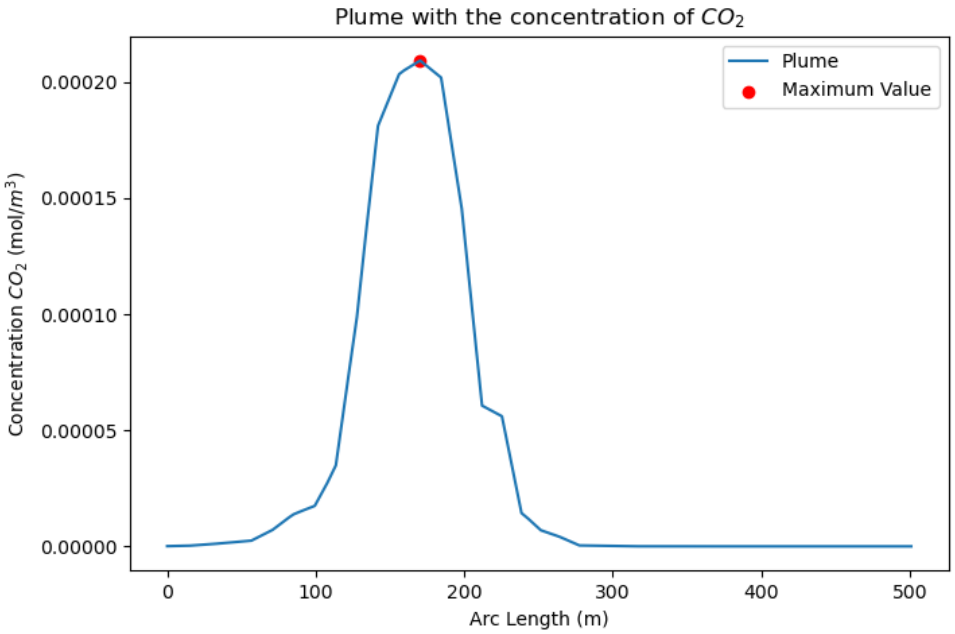

Figure 3.19: The plume with the maximum value marked in the plot.

4

Model Sensitivity Analysis

In this chapter, a sensitivity analysis of the model will be performed. The mode will be subject to changes in different ambient and operating conditions to evaluate its effects on the plume geometry and concentration gradient. This can be used in the analysis of the results when the model is compared with the measurements to explain any discrepancies that are found. The sensitivity analysis will be done with several base parameters, which can be found in Figure A.1. The ambient conditions are also stated. The wind direction will be set to 90 degrees, thus perpendicular to the runway. The speed of the wind will be equal to 5 m/s. All the variables will be kept constant during the sensitivity analysis except for the parameter investigated; this ensures that the results only reflect the influence of the variable studied.

4.1. Curve Fitting

Before delving into the different variables for analysis, curve fitting must be discussed. Curve fitting is a technique that can be used to find the best fitting curve or function to represent a set of data. In this case, the data is from the plumes. The function that is used is chosen to closely match the behaviour of the data set. Due to the fact that the results from the sensitivity analysis vary in relationship, it is essential to select a versatile function. The chosen curve fit is seen in Equation 4.1. This function is defined as an exponential decay model; as was said, this is chosen as it can represent all kinds of different datasets. Here, the y represents the dependent variable, for example, the maximum concentration or the plume width. The x is seen as the independent variable, for example, the wind speed. In addition, there are three other parameters, a, b, and c, which determine the amplitude, decay rate, and offset of the exponential decay curve. These parameters are adjusted to capture the relation of the various data points carefully and to be able to draw conclusions from the sensitivity analysis.

$$y = a * e(-b * x) + c \tag{4.1}$$

4.2. Mesh Analysis

The first aspect that is used for the sensitivity analysis is the mesh. The mesh in COMSOL refers to the discretisation of the domain into smaller elements. These elements can have different geometric shapes depending on if the domain is 2d or 3d. For 2d, these elements have a triangular shape. Dividing the domain into these smaller shapes allows numerical solutions to calculate the plume at each component. An example of the mesh is shown in Figure 4.1.

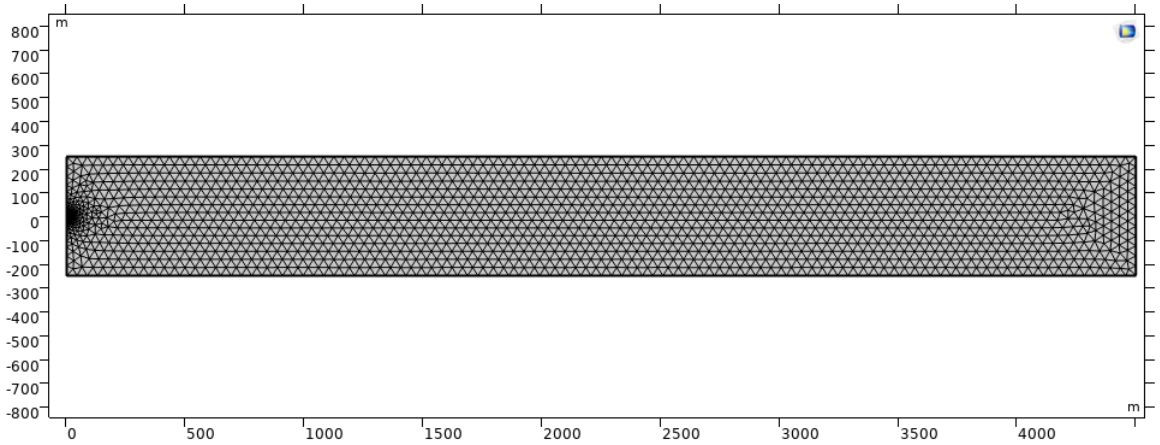

Figure 4.1: The domain shown with a mesh applied

A few things need to be discussed before delving into the analysis. Looking at Figure 4.1. At the beginning of the domain, especially the area surrounding the outlet of the jet engines. The mesh is finer. A finer mesh provides a higher spatial resolution. This allows for a more accurate representation of the physics that takes place in the model as the smaller elements capture finer gradients in the parameters flowing through the model. The refinement at the beginning of the flow is done by CO SOL self and can be seen as an automatic step to ensure a sense of accuracy. The rest of the mesh in the domain can be seen as uniform, as each element has the same size throughout. COMSOL offers different preset resolutions. The resolution ranges from extremely coarse to extremely fine. These can be seen in Table 4.1.

Mesh Type	**Number of elements (#)**
Extremely Coarse	1715
Extra Coarse	3497
Coarser	5660
Coarse	12119
Normal	19563
Fine	29854
Finer	133579
Extra Fine	509210

Table 4.1: The different preset resolutions offered by COMSOL

Table 4.1 shows the name of the preset that is used on the domain, and the number of elements indicates how many triangles the domain is divided into. Note that this is also dependent on the length of the domain, which varies with the crosswind. The number of elements from this table originates from a domain with a length of 4500 meters. In section A.3, the domains with different resolutions can be seen. Different mesh types are tested to investigate the effect of the mesh on the plumes in the simulation. The plumes are simulated and plotted in Figure 4.2.

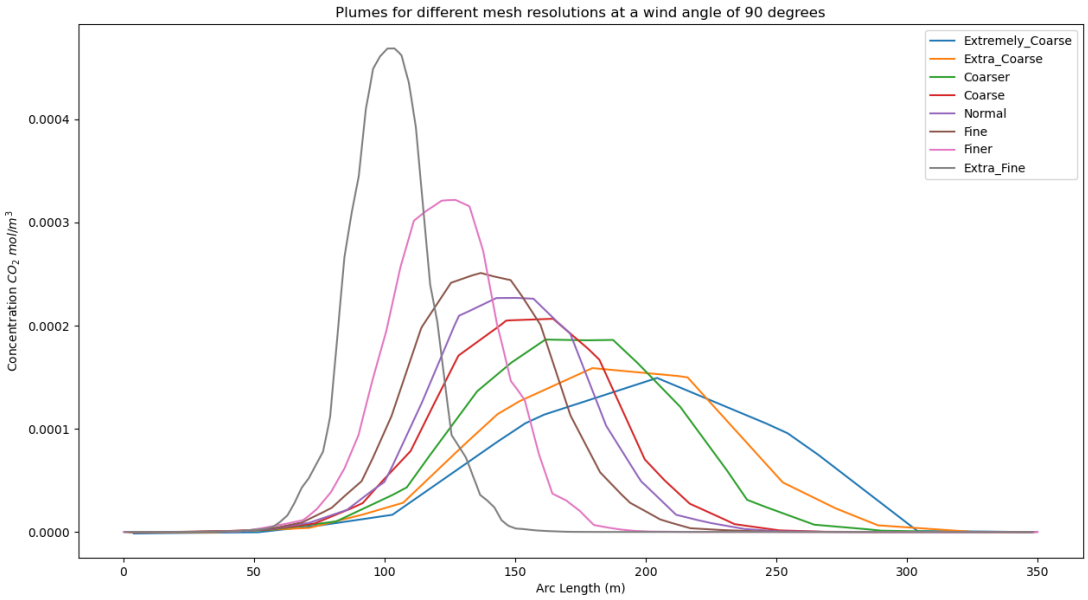

Figure 4.2: The plumes simulated with different mesh resolutions applied to the domain

Several things are to be seen in Figure 4.2. The first is that the plume becomes much thinner as the mesh increases in number of elements. The finest mesh results in the highest peak of concentration measured. Another aspect is that the jaggedness of the line increases as the mesh resolution decreases. This is because a lower mesh results in larger elements, which causes more significant concentration differences between each component.

A plot can also be created only to show the maximum concentration. This plot can be seen in Figure 4.3. A few things can be seen here, such as the converging nature of the curve. The steepness of the curve in the first few points does not continue throughout and is seen to flatten, especially considering the last two points of the plot. This means that refining the mesh has its limits in obtaining a more accurate solution. The difference between the peak concentration of the extra fine mesh and the extremely coarse is around 300%. This illustrates the effect the mesh has in the early stages.

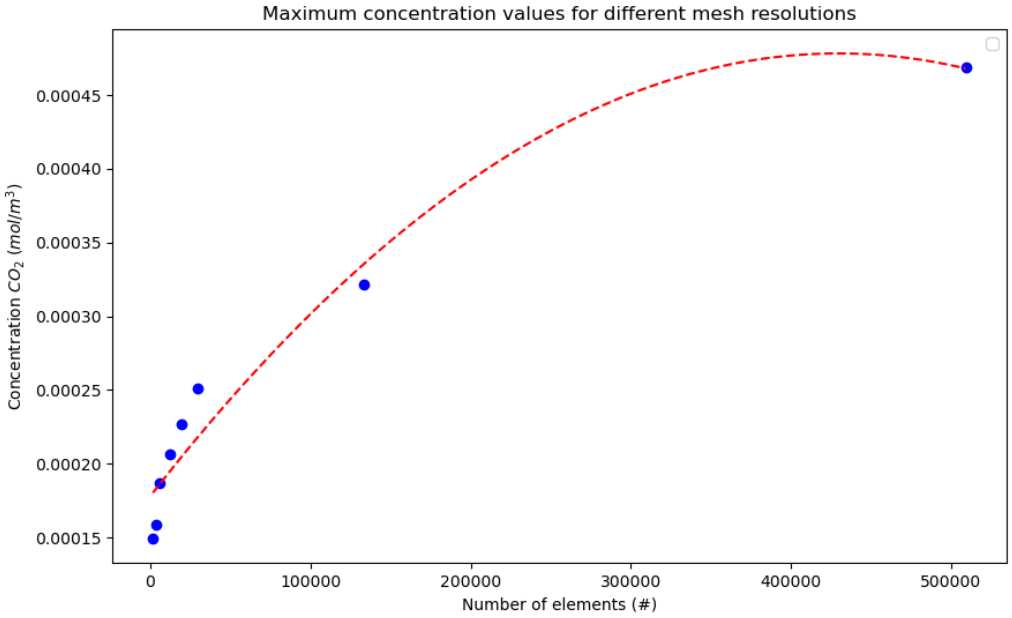

Figure 4.3: The maximum concentration of the plumes simulated with different mesh resolutions applied to the domain

The same thing is done for the plume width. Figure 4.4. For the lowest mesh, the plume starts with a width of 236 and for the finest mesh, this results in a width of 83 meters. The same converging relation can be seen as it was with the maximum concentration values. The width cannot endlessly decrease and, therefore, is seen to travel to its stable point.

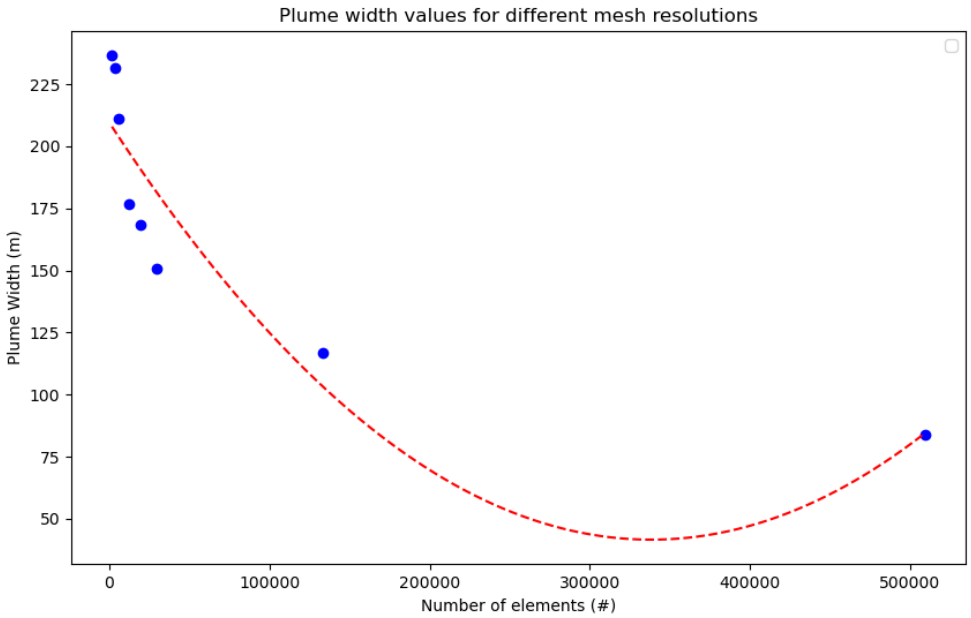

Figure 4.4: The plume width of the plumes simulated with different mesh resolutions applied to the domain

Now, looking at the conclusions from the plot, it could be said that a mesh should be applied as fine as possible to the domain. However, it should be noted that a fine mesh has consequences for the

applicability of the model. The mesh is one of the most significant drivers of the computational cost. Therefore, it is vital to research its effects. A plot is created that shows how long it took for a plume to be computed for the different meshes, seen in Figure 4.5. The finest mesh results in a simulation which takes around 2 hours and 40 minutes. This needs to be accounted for when trying to model a large set of aircraft arrivals and departures. A side note is that computational time is particular to the computer used and the RAM available. When simulations are done on other computers, they may result in faster or slower simulations.

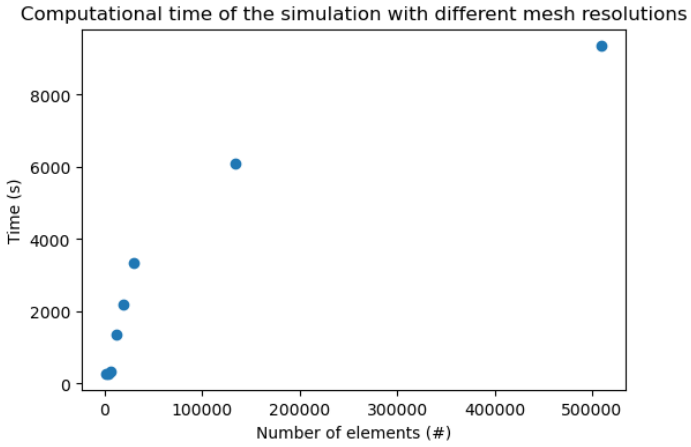

Figure 4.5: The time needed for the model to simulate the plume

4.3. Adaptive Mesh Refinement

The meshes that have been used until now are seen as uniform meshes (except for the small area surrounding the jet outlet); however, there are also other methods to construct a mesh that is more appropriate to the physics simulated. One of these methods is adaptive mesh refinement. This technique can be done through COMSOL, which adjusts the mesh resolution based on the characteristics of the simulation. These simulation characteristics include the geometric features of the domain and the parameters defined by the user. The most used method in adaptive mesh refinement is similar to the uniform mesh. This method involves the division of elements into smaller subelements. However, this time, COMSOL monitors the simulation by analyzing parameters such as velocity and concentration gradients and deciding where additional mesh refinement is most beneficial. COMSOL calculates errors between the elements and uses this to refine the mesh further. The method can be seen in Figure 4.6. The mesh is refined at the locations where the plume travels across the domain, resulting in a more accurate simulation.

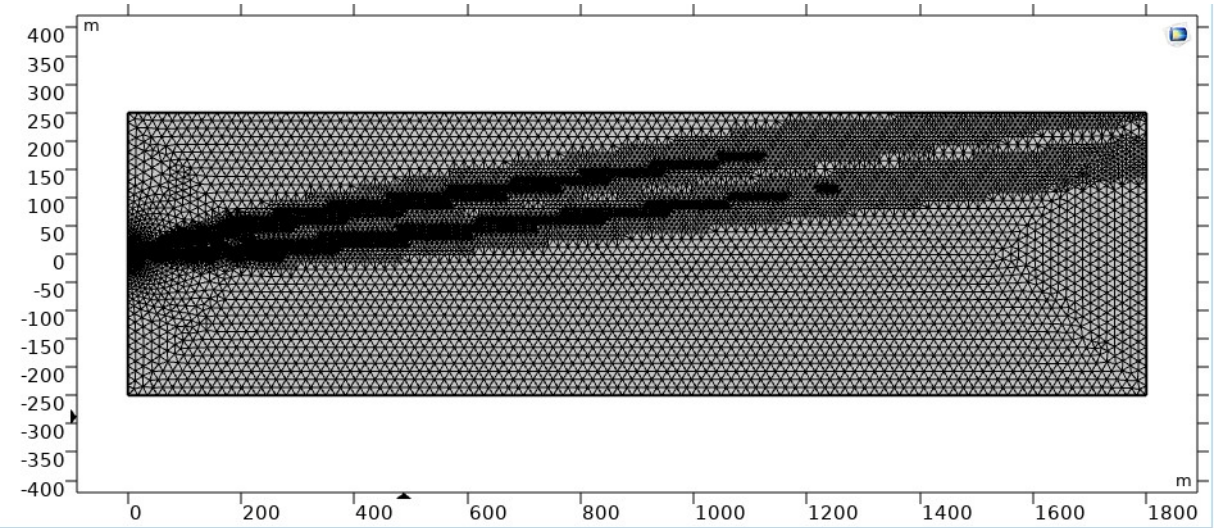

Figure 4.6: The adaptive mesh refinement shown in the domain

The comparison between the uniform mesh and the adaptive refinement method allows for a better understanding of the effect of using this type of method. The same plume characteristics can be compared: plume width and maximum concentration. Starting with the maximum concentrate, which is seen in Figure 4.7. A note that due to the computational cost of the last two mesh categories, these have been removed in this plot. The data resulting from the adaptive mesh follows the same trend as that from the uniform mesh. However, all the values of the adaptive mesh are higher than those of the uniform one. This is because the mesh is even more refined at the location where the plume is or was, and a more accurate solution, in this case, leads to a higher peak concentration. From this plot, it can be calculated that, on average, per mesh type, the adaptive mesh refinement method leads to a 24.0% higher peak concentration.

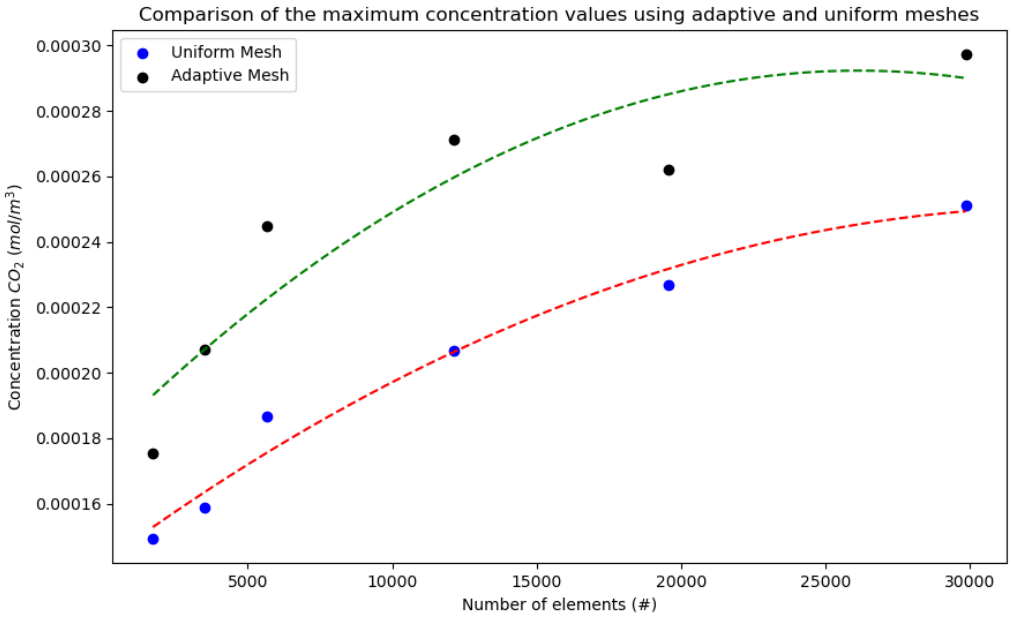

Figure 4.7: The maximum concentration of the plume when comparing the adapted mesh to its uniformly shaped counterpart

The same comparison is done for the plume width. It is resulting in Figure 4.8. Similar to Figure 4.7, a clear difference can be seen from starting from the first mesh type. Again, both follow the same

converging trend, and the difference stays stable. The plume width of the adaptive mesh is smaller throughout. The average difference per mesh type is equal to 21.6%.

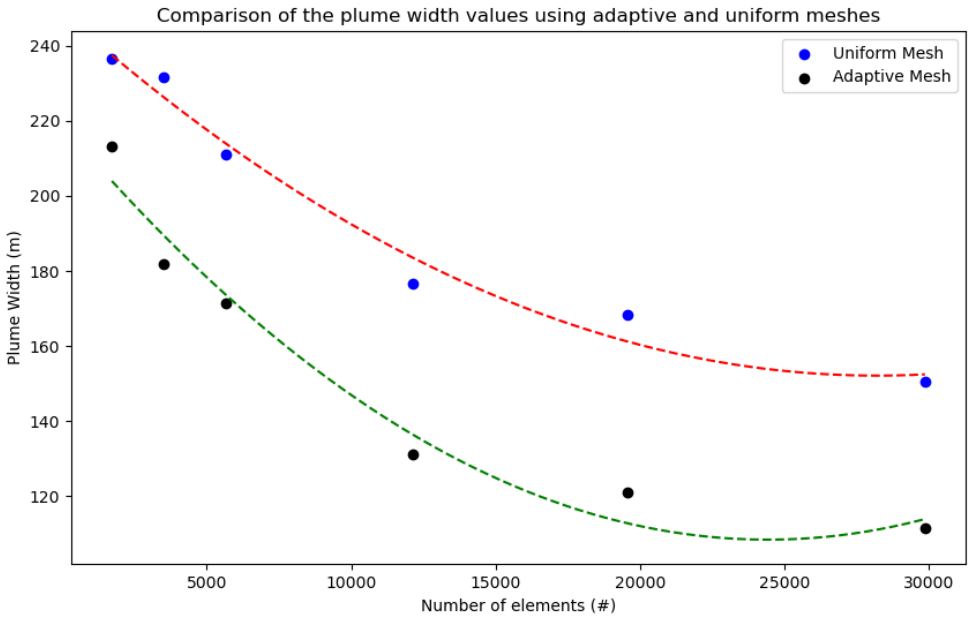

Figure 4.8: The plume width of the plume when comparing the adapted mesh to its uniformly shaped counterpart

From this mesh analysis, a few things can be concluded. A uniform mesh has a significant influence on the evolution of the plume and can result in triple the maximum concentration and width measured in the simulation. In addition, an adaptive mesh refinement method can be used. This influences both values by around 20%, which is quite significant. This confirms that from now on, this method should be incorporated into the simulations that are done. To create a balance between the computational cost and accuracy, a normal mesh category is chosen. How this might affect the results is as follows: In Figure 4.7 and Figure 4.8, the normal mesh category can be seen as the 1st to last point. Comparing this with the point at the next mesh category, the following is seen. The plume width differs by 9.1% while the peak concentration differs by 12.9%. These figures indicate how a finer mesh might impact the result and can be used when looking at ways to improve the results.

4.4. Engine Separation Distance

The next variable studied is the engine separation distance, as discussed in subsection 3.3.1. First, a suitable range must be found that accurately represents the type of aircraft landing at the Polderbaan. The data on the exact separation distance is not as easy to find as one may think. As this metric is often not shown, data like wingspan, height, and length are mostly found. The data from the ADS-B collected at the measurements also includes the Icao code with which the aircraft type can be found. One of the smaller aircraft that can be seen in the data is the Embraer 175. This is the smallest aircraft in the fleet of KLM [33]. While in the drawings, an exact figure is given to determine the separation distance, it is possible to extrapolate using the dimensions that are given. This gives a distance of around 6 meters. Another aircraft that is often seen in the data is the Boeing 737. For the Boeing 737 MAX, the distance is 9.64 meters [7]. There are also larger aircraft, such as the Boeing 787 Dreamliner. Here, a distance of 18.9 meters is shown [8]. Using the different data obtained, the range can be set. This is seen in Table 4.2.

Similar to the mesh analysis, the plots based on the plume width and peak concentration are created. This results in Figure 4.9. What can be seen from this plot is that the width increases as the distance between both engines increases. When the engines are farther apart, a few things happen. Then, the engine closest to the runway causes its own plume to reach the measurement station quicker as less

Engine Separation Distance (m)	8	10	12	14	16	18	20

Table 4.2: The different engine separation distances considered in the sensitivity analysis

distance has to be travelled. In addition, the engine that is farther from the station requires more time to travel. This effect causes an increase in plume width. If the effect is quantified, it can be seen that for each distance increase of 2 meters, the width becomes 1% larger on average. The plot regarding the effect on the concentration can be seen in Figure A.19.

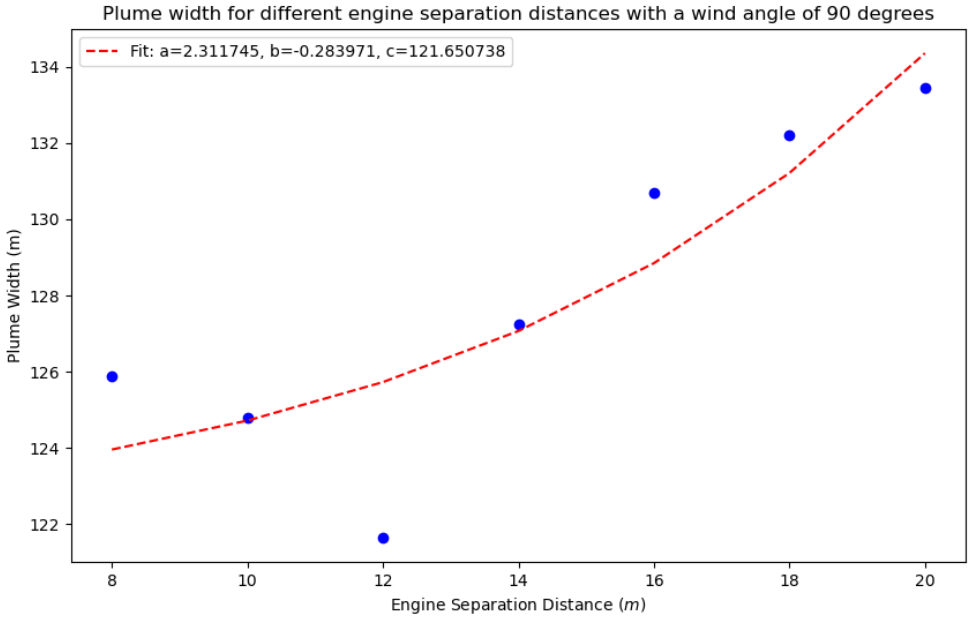

Figure 4.9: The plume width when comparing the distances between the engines

The same can be done with the peak concentration. The plot is seen in Figure A.19. The larger distance allows for more mixing with the surrounding air. This causes more dilution of the pollutants, which results in a lower peak concentration, resulting in Figure A.19. Another way of looking at it is that due to the fact that the engines are farther apart, pollutants are less likely to accumulate in the middle, resulting in a lower peak concentration. On average, the peak concentration decreases with 1.2%.

4.4.1. Non Gaussian Shape

The engine separation distance allows for an extra property that can be investigated. Until now, all the plumes simulated took a Gaussian shape. This meant that each plume had a single peak concentration value. When the engine separation distance increases, there becomes a point when the plumes of each engine do not have enough time to merge before reaching the measurement station. This would then result in a double-peak plume. Looking at the normal separation distances seen in aircraft, no non-gaussian shape can be found. Therefore, an extreme value is looked at to see when this phenomenon happened. Through trial and error, the distance is increased until two peaks can be observed in the concentration plot. This method leads to a separation distance of 73 meters, far larger than any aircraft that is landing at the Polderbaan. The plot can be seen in Figure 4.10. The plot clearly shows the two different peaks, each caused by the different engines.

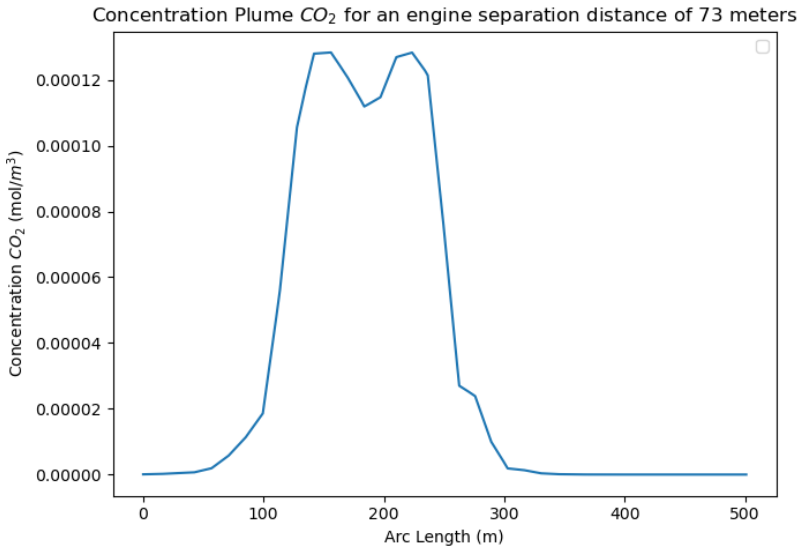

Figure 4.10: The concentration plot for a separation distance when the curve first shows a non-gaussian shape

4.5. Engine Diameter

When studying the various jet engines used in aircraft, one of the most obvious parameters is the engine diameter. The diameter determines the size of the flow entering the domain and is, therefore, an influential parameter. The different diameters of aircraft can be found in various sources, such as databases maintained by the EUSA or open source [19, 42]. In addition to finding the diameters of the engines, the first step is to determine which aircraft type has which engine. Aircraft engines are often updated, and newer models allow for greater efficiency, so aircraft may change engines from time to time. This means that it is important to establish which exact engine the aircraft is using when it lands at the Polderbaan. This can be done using the ICAO code; this code can be used to track the aircraft type and engine using the open source databases [52]. In order to obtain the range to be used for the analysis, the different aircraft are evaluated. When looking at the smaller aircraft that land at Polderbaan, one stands out: the Embraer 175. This aircraft has two CF34-8E6 engines with a diameter of 53 inches. This is the smaller end of the spectrum. On the other hand, if you look at the larger engines, the GE90-115B has the largest diameter at 157 inches. This type of engine is used by the Boeing 777-306ER [52], also seen at the Polderbaan. Now that the smallest and largest diameters are established, a range can be created, as seen in Table 4.3.

Engine Diameter ($Inch$)	50	60	70	80	90	100	110	120	130	140	150	160

Table 4.3: The various engine diameters used for the sensitivity analysis

The relation of plume width and engine diameter can be seen in Figure 4.11. A clear linear relation is observed as the plume increases with the diameter, as is expected; however, maybe not as much as was thought before. For each increase of 10 inches of diameter, the plume width increases by around 2.20%. The reason that this is not extremely large is likely due to several causes. Since the engine diameter stands at the origin of the plume, it has a long time to evolve before arriving at the measurement station. During this time, other effects such as wind speed and aircraft velocity have a significant amount of time to play a dominant role in the evolution.

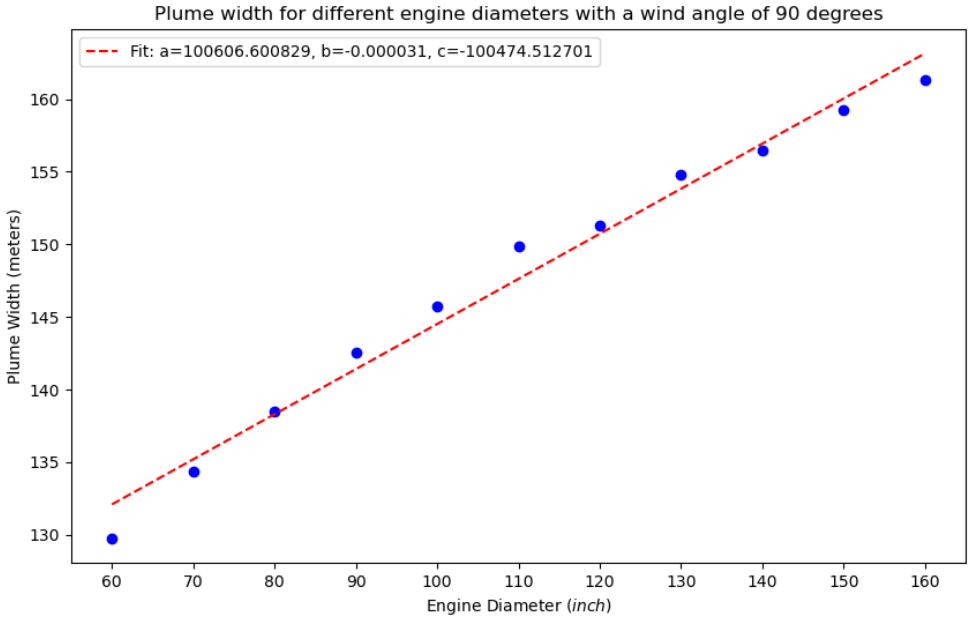

Figure 4.11: The width of the plume when comparing the different engine diameters

4.6. Aircraft velocity

The aircraft's velocity impacts the airflow around the aircraft itself. Therefore the air that is already inside the domain. This will influence the plume as this speed is added to the initial momentum given by the jet engine. Therefore, it is essential to include this in the sensitivity analysis. The aircraft's speed is heavily dependent on whether the aircraft is arriving or departing. The speed, like many other parameters, can be extracted from the ADS-B data. An example of the data snippet is shown in Figure A.10. It can be seen that, as expected, the velocity is significantly lower for arrivals as opposed to departures. In addition, the spread of the velocities for arrivals is lower. It can be seen that smaller aircraft like the Embraer 175 approach with a speed of 45 m/s while a Boeing 737 approaches with 70 m/s. This spread is not as present for departures. Here, aircraft mainly take off with a speed between 70 and 80 m/s. This leads to the following range being used for the analysis, as in Table 4.4.

Aircraft Velocity (m/s)	50	55	60	65	70	75	80

Table 4.4: The range of speed of the aircraft used

The plume width evolution can be seen in Figure 4.12. A clear correlation can be seen. The plume width increases with the aircraft speed, as is expected when looking at the peak concentration values. Each interval in velocity causes a 3.36% increase in plume width. At the same time, the largest delta in the set is 22.17%.

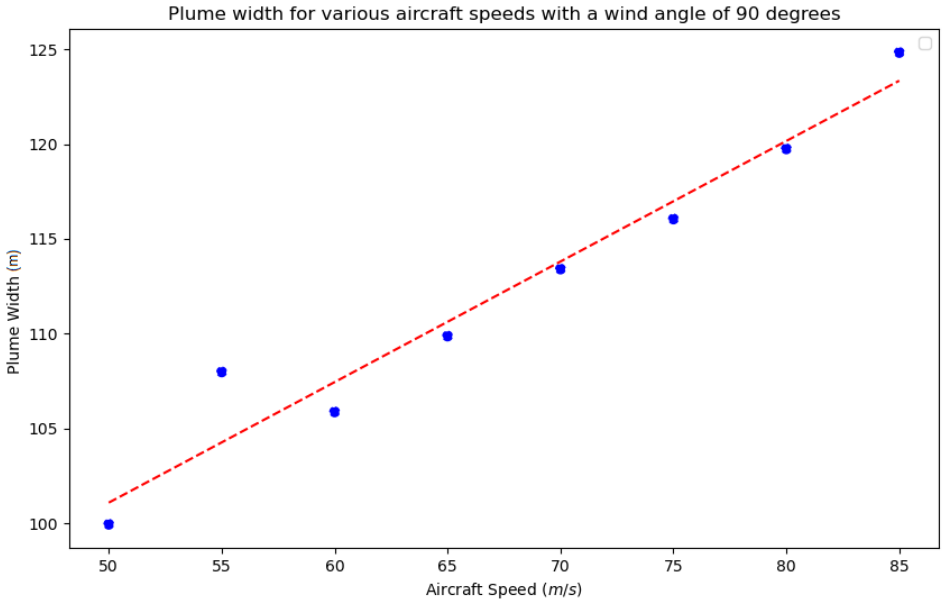

Figure 4.12: The width of the plume when comparing the different speeds aircraft travel at

Now, what causes this relationship? From an intuitive standpoint, one could argue that the plume should become thinner as the velocity increases because the air blows the plume faster down the runway. However, this is not what is seen in the plots. The plots illustrate a phenomenon that plays a crucial role in the shaping and evolution of the plume, called entrainment. This process describes how surrounding air is drawn into the jet exhaust [40, 55]. At lower velocities, the plume stays relatively narrow. However, when the velocity of the aircraft increases, a few things happen. Due to the velocity, a lower air pressure is created in the wake of the plane. This wake then serves as a vacuum, causing the surrounding air to be drawn into the exhaust. The surrounding air then mixes with the exhaust plume, causing an increase in width and a decrease in peak concentration. This is the entrainment phenomenon. The entrainment here is thus unrelated to the engine operating settings and solely on the aircraft speed. The results show that the entrainment plays a crucial part in the dispersion of the jet plume. As with previous parameters, the complete plumes can be found in Figure A.14, as well as the peak concentration plot in Figure A.15.

4.7. Pollutant Concentration

The main parameter that dictates the pollutant dispersion is the input parameter surrounding the amount of pollutants exiting the aircraft. Until now, the pollutant CO_2 was set at 200 ppm. This number was based on evidence found in the literature. However, since different engines are used, these include different emission factors and thus a varied input parameter of pollutants emitted. At this moment, the exact number of contaminants does not significantly influence the results of this section. The plume geometry and peak concentration are mainly studied, and how this relates to the change in parameter. Therefore, absolute value is not the main focus here. This leads to a quite straightforward range shown in Table 4.5.

Concentration Pollutant (ppm)	100	200	300	400	500	600	700	800	900	1000

Table 4.5: The amount of pollutant emitted by the engine

The plot containing the maximum concentrations seen in Figure 4.13 is less critical in this analysis. This is mainly shown to see that a linear relation can be seen as expected when increasing the input concentration. The complete plumes are in Figure A.17. Each increase of 100 ppm results in a peak value that is 31% higher than its predecessor.

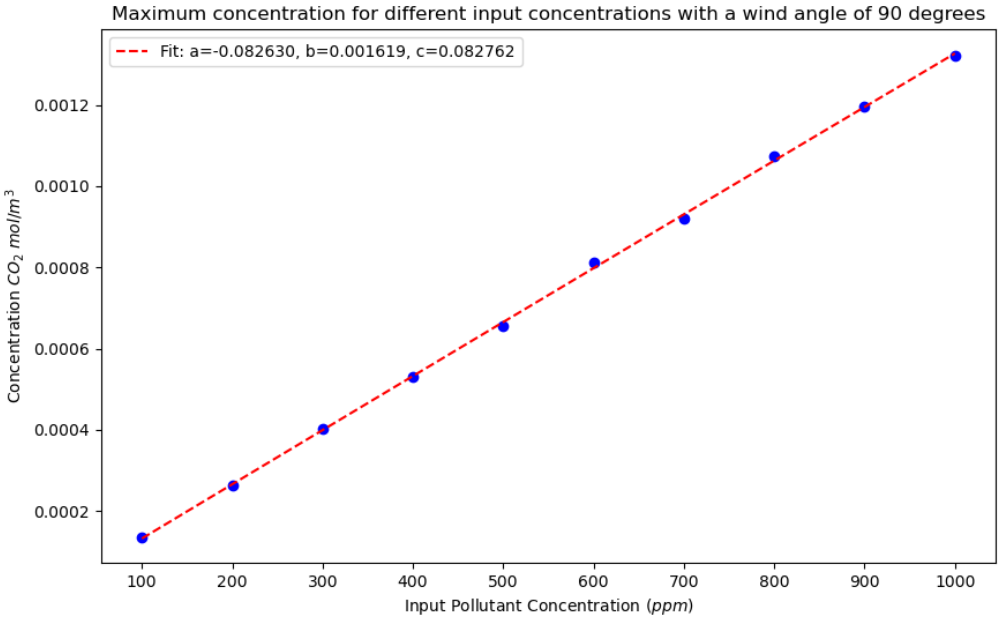

Figure 4.13: The maximum concentration of the plume when comparing the different pollutant input parameters

The more relevant figure for this variable analysis is Figure 4.14. As can be seen, no trend line has been drawn. This is because this can be seen as a relatively stable relationship. The amount of pollutants does not impact how wide the plume becomes. This is confirmed by looking at the largest delta between the widths. This is equal to 4.3%. However this could also be caused by the methodology in which the 2.5% of the peak concentration is used to create the boundaries of the plume width. This could be seen as a flaw in how the plume width is perceived when looking at aircraft with different input concentrations.

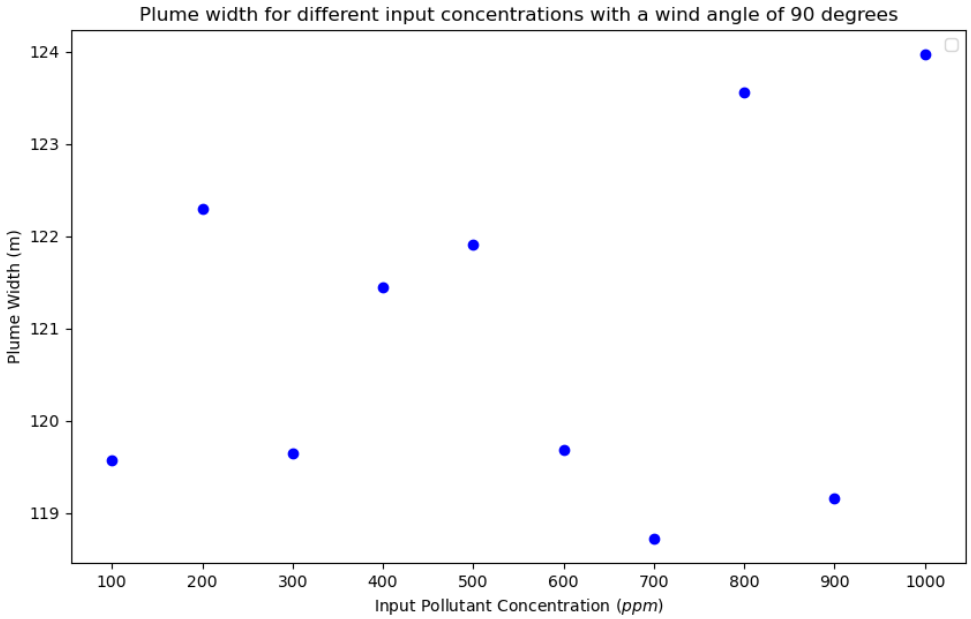

Figure 4.14: The plume width when comparing the different pollutant input parameters

4.8. Jet Engine Exit Speed

Staying in the category of aircraft-specific variables, the following parameter is the exit speed of the jet engine's air. This parameter is, of course, significantly dependent on the type of jet engine used. This speed influences how fast the air travels across the runway and, thus, when it bends across to reach the measuring station. Two main things need to be looked at to determine an acceptable range. Firstly, if it is considered arrivals or departures, as mentioned in Table 2.1 for an approach, the thrust setting is around 30% of the maximum, while for take-off, this is equal to 100%. This greatly influences the speed at which the air leaves the turbine. In addition, larger aircraft need to use a jet engine, which in turn has a higher maximum thrust, allowing for an increase in the velocity with which the air is pushed out, as established in Equation 3.7. The first step is to construct a range of thrust boundaries for the aircraft landing at the Polderbaan. For this, the emissions databank of ICAO is used [28]. This databank consists of a large set of information on emission factors from jet engines used on various aircraft. This also includes the maximum thrust, seen in Figure A.13. Filtering the data on what engine produces the largest thrust, the following is seen: The engine is made by General Electric Company and has the engine identification 'GE90-115B'; it has a maximum rated thrust of 513,9 kN. This type of engine is used on a Boeing 777, which can be identified in the measurement data and, therefore, serves as an upper boundary. A sidenote for this is to be used as an upper boundary. It is considered to be a departure, as only then all of the possible thrust is used. The same can be done to estimate the lower boundary, looking at the engines with the lowest thrust. One of these engines is the CF34, which is often used on Embraer 170 jets This aircraft is also seen landing on the Polderbaan. The thrust is equal to 64 kN; this time, an approach is considered, so around one-third of the thrust is used Using Equation 3.6, the following can be computed: the lower exit speed is equal to 50 m/s, and the highest is 290 m/s These numbers are rounded off to ensure a smooth analysis Using these boundaries the total range is seen in Table 4.6.

Exit Speed (m/s)	80	110	140	170	200	230	260	290

Table 4.6: The different exit velocities of the air leaving the jet engine

Starting with the plot of the different plume widths. As seen in Figure 4.15. When looking at Figure 4.15, it can be seen that the width decreases as the velocity of the air leaving the jet engine increases. A higher velocity means the flow carries more momentum and thus causes the pollutants to spread out less. The following can be seen when looking at how much the width is affected. For each increase of 30 m/s, the plume decreases by 2.22%. The complete plumes are seen in Figure A.20 and peak concentration values in Figure A.16.

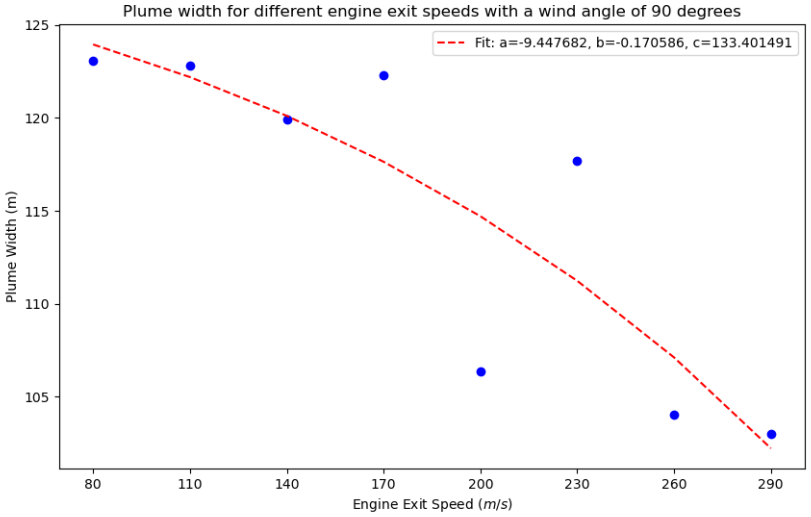

Figure 4.15: The plume width for different exit velocities

Figure A.16 illustrates the relationship between the exit velocity and the peak concentration. As expected from the results from Figure 4.15, an increase in peak concentration can be seen. The concentration does seem to increase significantly more compared to the width. The peak value grows to 8.43% with each step. Looking at the plots generated, it can be seen that the velocity has a large impact on the evolution of the plume. However, this has to be put into context, as the range of velocities considered is extreme. Starting with the approach engine velocity of the smallest aircraft and ending with the departing velocity of the largest aircraft engine. Taking this into consideration, the effect of this variable is considerable but not extreme.

4.9. Wind Speed

One of the most essential ambient parameters is the wind speed. This parameter dictates the trajectory of the plume and governs how quickly the plume reaches the measuring station This, in turn, determines how long the plume has to develop, which can be seen in the geometry and the peak concentration The wind is also the only force that works perpendicular to the plume and is, therefore, attractive to test As mentioned before, the wind direction is set at 90 degrees This is done as the wind in other directions can also be translated into a crosswind component and, therefore, is indirectly also in this analysis From the measurements, a wide range of wind speeds can be seen These are both for arrivals and departures Looking at the maximum wind speed of a measurement day, which lies around 9,7 m/s at the top value, can be seen on which the parameter range is based On the lower side, this value lies at around 2.5 m/s however this is not solely crosswind Most often, the wind is not completely perpendicular to the runway Therefore, the lower range is set at 1 m/s This results in Table 4.7.

Wind Speed (m/s)	1	2	3	4	5	6	7	8	9

Table 4.7: The amount of pollutant emitted by the engine

Several things can be seen when investigating the effect of the wind speed on the plume width. Figure 4.16 shows the results. The relationship is relatively linear and can be seen as quite strong. Per step that the wind speed increases, the plume width decreases by 3.49%. The largest delta in this data set is equal to 29.1%. This is a significant amount and illustrates that the wind speed has a crucial impact on the development of the plume.Figure A.11 and fig: Figure A.12 show the results of the complete plumes and peak concentration values respectively.

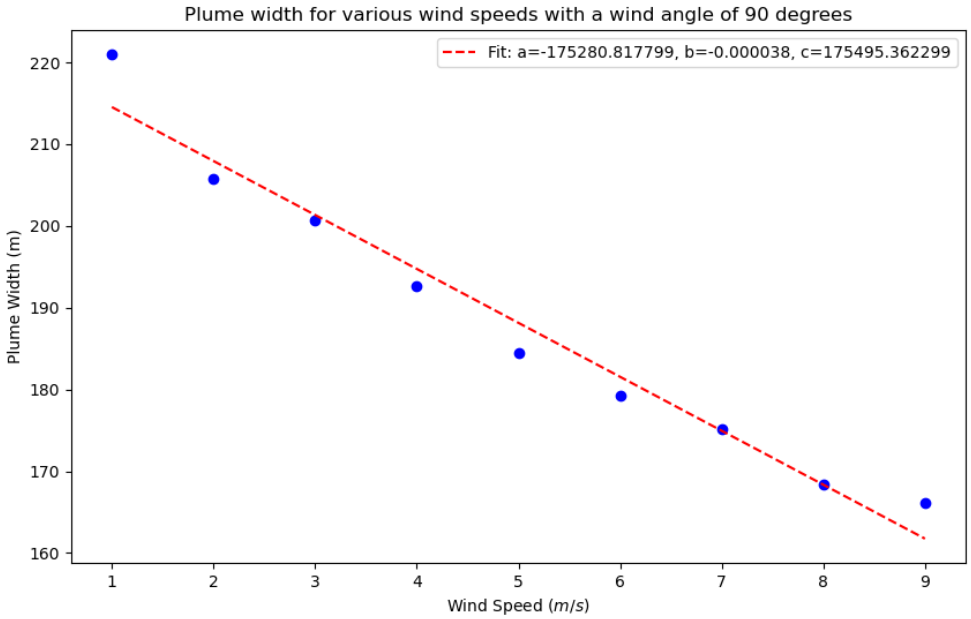

Figure 4.16: The plume width of the plume for different crosswind velocities

4.10. Concentration Threshold

Unlike the other sections of the sensitivity analysis, this portion does not involve an operational or ambient variable. In subsection 3.5.1 and subsection 3.6.1, the starting point and width of the plume were discussed. This used a concentration threshold to mark the starting and ending points of the plume to start the analysis. In addition, the starting point was also used in the point and direction function and thus where the plume was 'cut' through. Using this methodology affects the geometric properties of the plumes, which leads to a possible deviation from the results compared to the measurements. Therefore, it is important to quantify these effects. As was seen, a threshold concentration of 2.5% was used for the sensitivity analysis until now. Smaller and larger thresholds will be used to evaluate how they affect the plume identification and extraction method. The different thresholds as a percentage of the maximum concentration used can be seen in Table 4.8. For example, a threshold of 0.5% means that where the plume concentration is 0.5% of its peak, it will be seen as the location where the point of direction function will be used to create a perpendicular view to the plume. In addition, the same threshold will be used to calculate the plume width. Therefore, it cannot be said that a 1% threshold change results in a 1% plume width change.

Concentration Threshold	0.5%	1%	1.5%	2%	2.5%	3%	3.5%	4%	4.5%	5%

Table 4.8: The different percentages used to calculate the concentration threshold .

The effect of the concentration threshold on the plume width is seen in Figure 4.17. The plume width decreases as the threshold increases. This is as expected. The main point of this analysis is to research how much the width decreases. Each half percentage point makes the width decrease by 2.66%.

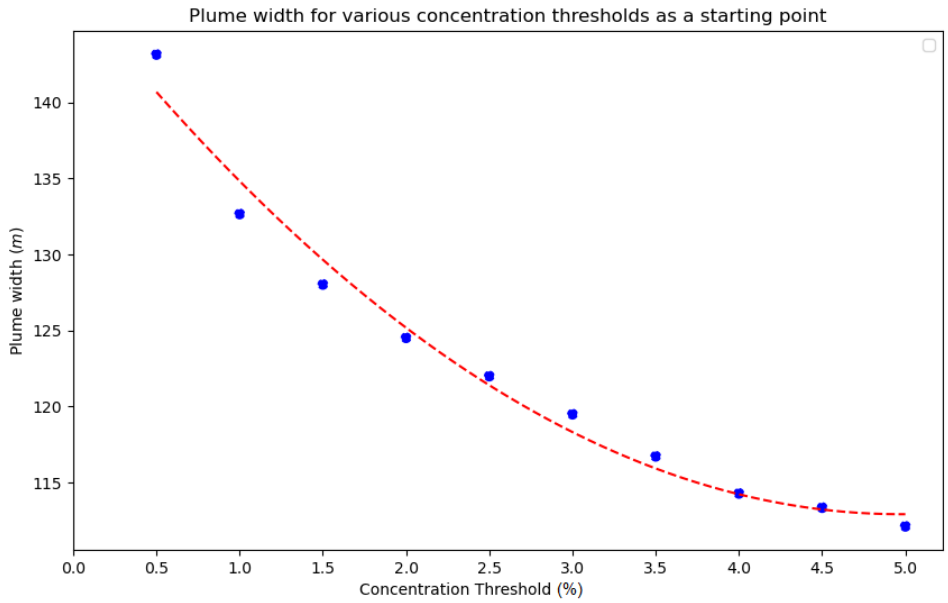

Figure 4.17: The plume width when using the various thresholds to extract the plume

Now, for this variable, it is also interesting to observe the peak concentration value, as this also varies. This is due to the fact that the threshold determines where it is decided that the plume has reached the measuring station. Therefore, a change can be seen in Figure 4.18. The effect of the threshold chosen on the concentration is less significant than that of the plume width. Each step accounts for a 0.77% decrease. This is caused by the fact that a larger threshold means that the plume is extracted at a location further along the runway, giving the pollutants a chance to disperse even more.

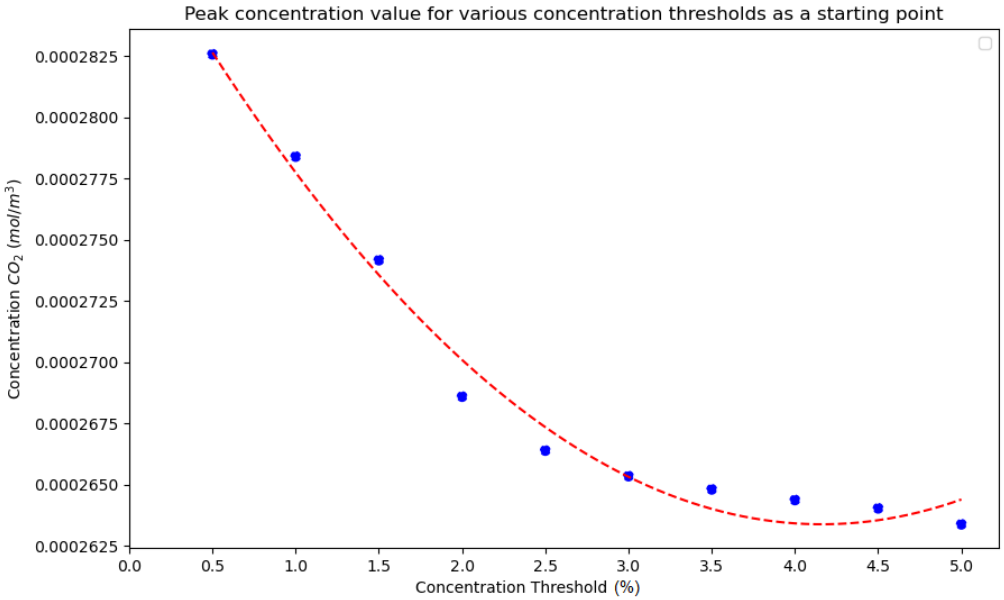

Figure 4.18: The peak concentration when using the various thresholds to extract the plume

The results show that, especially for plume width, the threshold used matters significantly. However, it must be used with caution as taking a small threshold can only be done when the data collected from the measurements is accurate and unaffected by other background pollution, which is almost never the case.

4.11. Concentration Input

As is the case with almost all models, the results are only as good as the input parameters. Now, when assessing the air quality and evaluating the peak concentration, the input parameters surrounding this play a crucial role. The parameter was briefly discussed in subsection 3.3.1. However, this did not include how the parameter is quantified. The method that is used is done through using the ICAO emissions databank [28]. The databank contains the emissions factors of different pollutants, specifically NO_x and CO. In Figure A.21, a table is found. Here, it is also seen that the emission factor depends on the operating condition of the engine. In Table 4.9, the different modes are defined. As can be seen, the focus will be on the take-off (T/O) and the approach (App).

Operating Conditions Specified	
T/O	Take-off
C/O	Cruise
App	Approach
Idle	-

Table 4.9: The different engine operating modes defined in the ICAO databank

The next step is to determine how the emission factor can be used to compute the input parameter. The emission factor is defined as how much gram pollutant is emitted per kg fuel burned. Therefore, the fuel usage must be used to determine this. To do this, it is possible to use the same databank as is used for the emission factor. For each operating condition and engine, the fuel flow in kg/sec can be seen. This means that if it is known how long the engine is running, an estimation can be made for how much is emitted. This is shown in Equation 4.2.

$$C_{i,j,k} = EI_{i,j,k} * FF_{i,j,k} * T_i * n \tag{4.2}$$

The variables in Equation 4.2 are as follows. C is the concentration emitted. EI is the emission

factor in g/kg and FF the fuel flow. Lastly, the T is the time the engine spends in a specific mode. These parameters are specific to certain characteristics. The mode the engine is in is denoted with i. The type of engine is defined by j, and k shows which pollutant is considered. Finally, n is the number of engines on the aircraft.

Almost all the variables used in Equation 4.2 can be found in the ICAO emissions databank. An exception is the time the engine spends in a specific mode T_i. This time is difficult to define. The problem is to translate a dynamic event, an aircraft landing or taking off, to a static plume. The starting point is to investigate the dimensions of the Polderbaan further. This is seen in Figure 4.19.

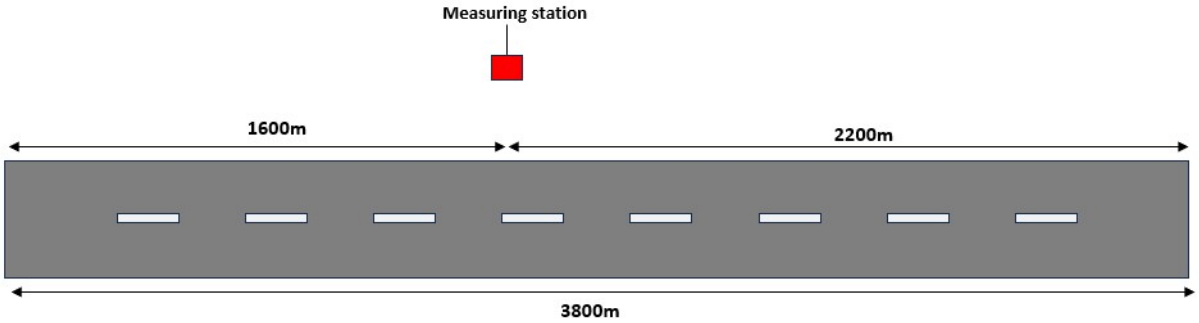

Figure 4.19: The different geometric distances defined needed for the analysis

Figure 4.19 shows the Polderbaan in relation to the measurement station. In order to be able to estimate the T_i, two different cases are created. The two different cases are as follows:

- **Full Runway**: The first case is to base the time in mode on the total length of the runway. The total length of the Polderbaan is 3800 metres [54]. This distance can be used as a starting point when evaluating T_i and is the same for arrivals and departures.
- **Runway Cutoff**: The second case is to base the time in mode on the relative cut of the length of the runway in relation to the measurement station. In other words, the length of the runway is equal to the distance up until the aircraft is parallel to the measurement station. This is dependent on whether the aircraft is departing or approaching since the measurement station is not exactly in the middle. For approaching aircraft, this distance is set at 1600 meters, and it is done by analyzing the Polderbaan through Google Maps. For departing aircraft, the distance is 2200 meters.

After using one of the different cases, the same method can be used to calculate. The velocity of the aircraft is needed to determine how long it is on the runway. This is as mentioned in subsection 3.3.1 able to be extracted from the ADS-B data. For this, it is assumed that the velocity is constant. While this is a hefty assumption, it is necessary to have a validated comparison between the static plume, in which a constant aircraft velocity is needed, and the real-life LTO cycle. If a variable velocity were chosen, the results from the model would be less valuable; thus, it is chosen not to. Using the aircraft velocity, $V_{aircraft}$, the time in mode can be computed using in Equation 4.3. The length of the runway, L_{runway}, depends, as mentioned, on which case is used and if the aircraft is departing or arriving.

$$T_i = \frac{L_{runway}}{V_{aircraft}} \tag{4.3}$$

Now that all the information is gathered to calculate the concentration one more thing is needed. The concentration that flows from Equation 4.2 is in grams. For the model, this input must be in ppm. This can be done in the equation seen in Equation 4.4. From Equation 4.2 the $C_{i,j,k}$ can be recognised, which is also used in Equation 4.2. R is the ideal gas constant and T the ambient temperature. The molar mass of pollutant k is denoted with M_k. The volume, V, is the volume of the jet engine.

$$ppm = \frac{R * T}{P * M_k} * \frac{C_{i,j,k}}{V} \tag{4.4}$$

4.12. Influence of reverse thrust

From the measurements done in Schiphol, it is known that some aircraft use reverse thrust. This influences the number of pollutants emitted by the aircraft. On average, the aircraft uses reverse thrust for around 16 seconds [49]. During this period, the thrust of the engine is increased to around 60%, resulting in needing an emission factor that cannot be categorized as an approach. This means that this influences the input concentration parameter. The equation to calculate the parameter under the influence of reverse thrust is seen in Equation 4.5. The average duration of the reverse thrust process is subtracted from the entire time in mode, T_i. This 16 seconds is then added in the second part of the equation; here, the fuel flow and emission factor are set at the take-off mode. The two parts are added to create a new input concentration parameter.

$$C_{i,j,k} = (EI_{i,j,k} * FF_{i,j,k} * (T_i - 16) + EI_{T/O,j,k} * FF_{T/O,j,k} * 16) * n \tag{4.5}$$

While in the experiments, no note is made which aircraft when used reverse thrust, it is still valuable to quantify this effect and see the difference in the results of the model. This is done for both cases of determining the runway length. In order to analyse this effect carefully an aircraft must be chosen for which the different parameters can be established. The aircraft considered is a Boeing 737NG; the engine used on this aircraft is a CFM567-B24. This is shown in Table 4.10.

Boeing 737NG Parameters	**Arrivals**	**Departures**
Aircraft Velocity (m/s)	71	82
Fuel Flow (kg/s)	0.316	1.103
EI CO (g/kg)	2.2	0.4
EI NO_x (g/kg)	10.1	25.3

Table 4.10: The different input parameters of the Boeing 737NG

The parameters used in Table 4.10 can be used to calculate the pollutants emitted in grams, for both the entire runway and the cutoff case. Using Equation 4.2 and Equation 4.5.

Full Runway Case	**No Reverse Thrust**	**Reverse Thrust**
Approach		
CO (g)	37.166	33.10
NO_x (g)	170.62	566.05
Departures		
CO (g)	20.57	N.A
NO_x (g)	1325.53	

Table 4.11: The concentration calculated for the full runway case .

In Table 4.11 the full runway case is considered. Reverse thrust results in a higher amount of NO_x emitted, while for CO, this number decreases. This is as expected as CO is only produced in higher amounts when a lean fuel mixture is used. Reverse thrust uses a rich fuel mixture, and thus, the total amount of CO decreases when looking at the entire runway.

Runway Cut-off Case	**No Reverse Thrust**	**Reverse Thrust**
Approach		
CO (g)	19.11	15.05
NO_x (g)	87.78	483.19
Departures		
CO (g)	8.824	
NO_x (g)	558.117	

Table 4.12: The concentration calculated for the runway cutoff case

For the runway cutoff case, the pollutant parameters are shown in Table 4.12. As expected, these values are lower compared to the full runway, as less time is modelled for the aircraft to emit pollutants.

The results of both cases also show the ratio of how much pollutant is emitted less or more when reverse thrust is observed. Note that this is only done for a single aircraft type, so figures may differ when various engine types are considered. However, for this test, reverse thrust causes a 10.9% drop in emitted CO when considering the full runway case. Looking at NO_x, a more extreme difference is observed. This shows that around 3.3 times more NO_x is produced. The full runway case was chosen to calculate the amount of species emitted.

4.13. Ratio NO_2/NO

The ICAO emissions database only provides information on the emission factors of NO_x, so it is necessary to understand the ratio of NO_2 to NO. As NO leaves the engine, it has the opportunity to oxidise and turn into NO_2, the longer the plume has to travel, the higher the ratio of NO_2/NO will be [23]. This means that considering the experimental setup, it is necessary to look at the ratio when the plume is about 190 metres from the runway. Several studies have looked at the ratio at this distance. Including the work of Rik Goudswaard [22]. The results of the different studies are shown in Table 4.13. The results show that the ratio should be between 0.6 and 0.7. As the study by Stacey et al. covered most of the plumes, a ratio NO_2/NO of 0.6 is chosen.

Ratio NO_2/NO	**Location Measurement**	**Author**
0.6	170 meters from the runway at London Heathrow	Stacey et al. [56]
0.6	200 meters from the runway of Athens International Airport	Bossioli et al. [9]
0.7	190 meters from the Polderbaan runway at Schiphol	Rik Goudswaard [22]

Table 4.13: Different studies to establish the ratio of NO_2/NO that can be used for this project

4.14. Plume Cross-section

In subsection 3.5.1, the starting point of the plume was determined. This was done using a horizontal line 190 metres parallel to the runway to identify the plume's beginning. This was set at 2.5% of the maximum concentration value. However, the plume can also be drawn through different points of the plume. This means the point which is used for the point and direction function is not necessarily the starting point. In Figure 4.20 three different points are shown. The first point (F) is used before 2.5% of the peak concentration. The endpoint (E) is calculated using the same method as the beginning but is set after the peak of the plume. The middle point (M) is, as the name suggests, precisely in the middle of the beginning and end points. These three points will result in plumes that differ in plume width and, thus, in concentration. Therefore, it is valuable to try to quantify this effect.

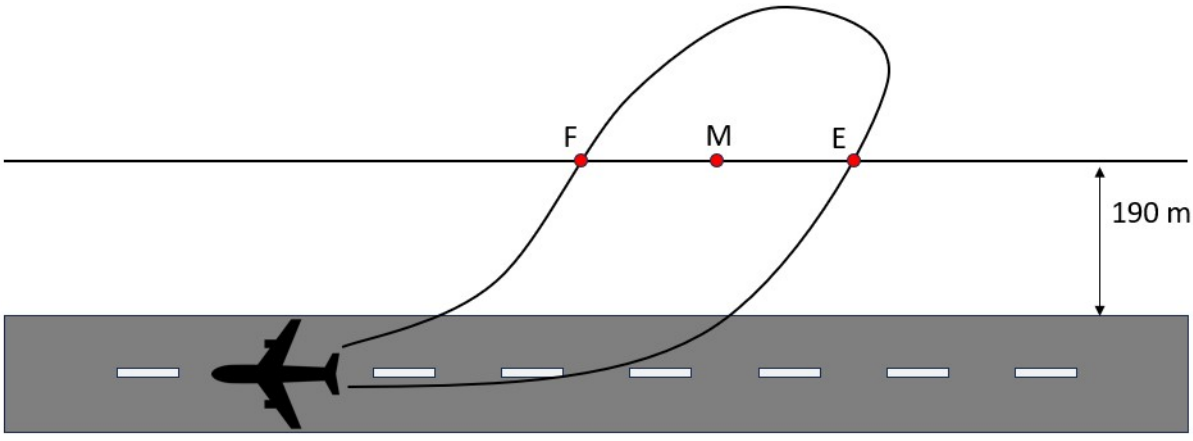

Figure 4.20: The different points that can be used as a starting point

The starting point to evaluate this is to simulate a plume which can be used for the analysis. For this plume, a windspeed of 5 m/s is chosen exactly perpendicular to the runway. Then, the different points are used, which are used in the point and direction function of COMSOL in order to extrude the section

perpendicular to the edge of the plume as was shown in Figure 3.14. This leads to Figure 4.21. It can be clearly seen that the plume which uses the first point for the cross section is much thinner compared to the other plumes. The plume becomes wider as the point moves along the horizontal axis of the plume. The plume that uses the endpoint can be seen as the widest. In line with this is the decrease in peak concentration.

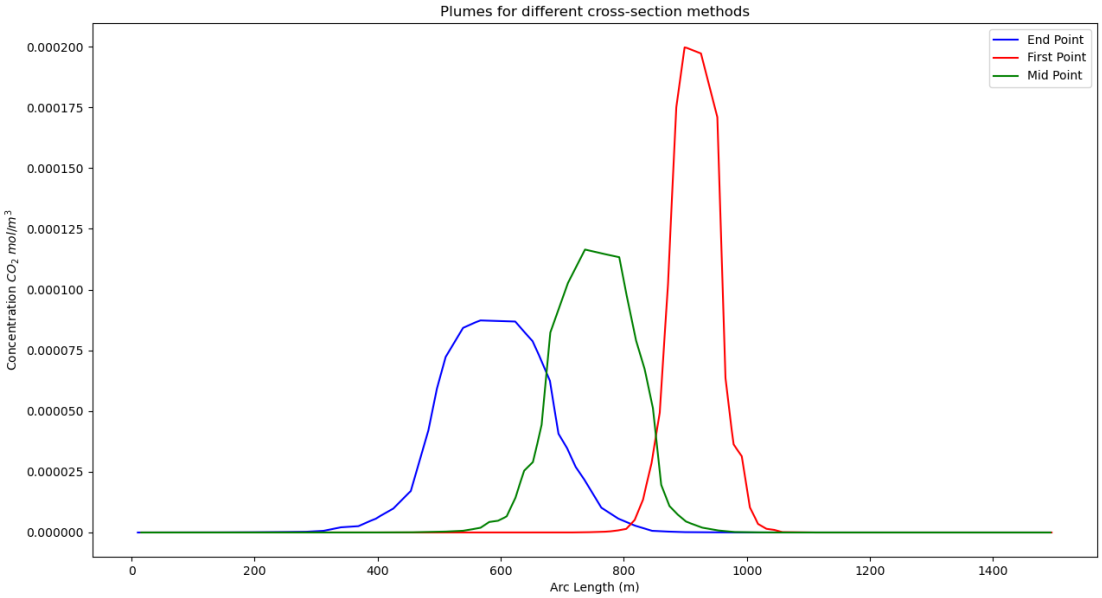

Figure 4.21: The different cross sections of the plumes

From Figure 4.21, the difference in width can be clearly seen. The exact widths are shown in Figure 4.22. The starting width using the first point extraction is equal to 198 meters. When moving up to the midpoint, the width increases to 344 meters. Finally, the largest width is as expected when the endpoint of the plume is used, this results in a width of 484 meters. This shows that choosing a different cross-section can result in almost a doubling of the plume width.

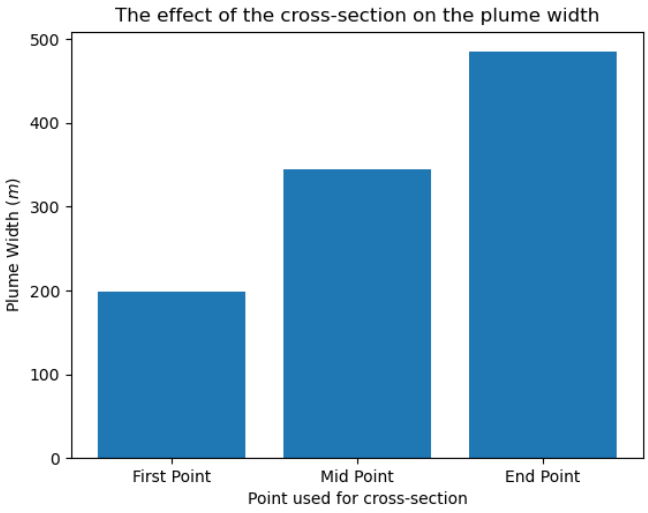

Figure 4.22: The different plume widths when different cross-section points are applied

The same plot can be generated to determine the effect on the peak concentration value. This leads to Figure 4.23. The peak concentration for the first point equals 8.731E-5 $mol/m^3\ CO_2$, while for the mid and endpoint, this is respectively 1.997E-4 and 1.1164E-4 $mol/m^3\ CO_2$.

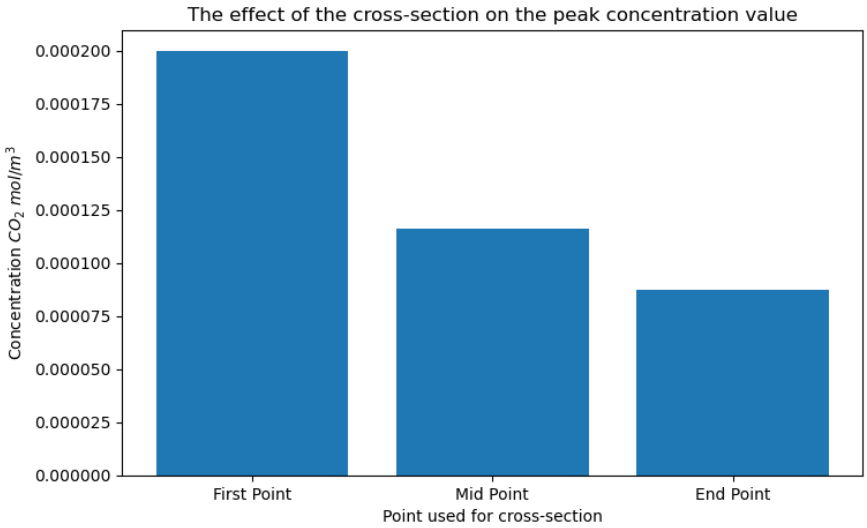

Figure 4.23: The different peak concentration values when different cross-section points are applied

As was seen in the section 4.9, the wind speed most significantly impacted the plume width from all the different parameters. This makes it interesting to create an analysis of the effect of the crosswind on the different cross sections. The difference for one wind speed shown in Figure 4.21, illustrates the large variance. The same range is chosen as in section 4.9, seen in Table 4.14.

Wind Speed (m/s)	1	2	3	4	5	6	7	8	9

Table 4.14: The amount of pollutant emitted by the engine

The entire plumes can be seen in Figure A.22. Firstly, the plume width is looked at. Figure 4.24 shows the relation. As expected, the plume becomes wider as the crosswind is lower. It also can be seen that the spread between the points used for intersection increases as the wind speed decreases.

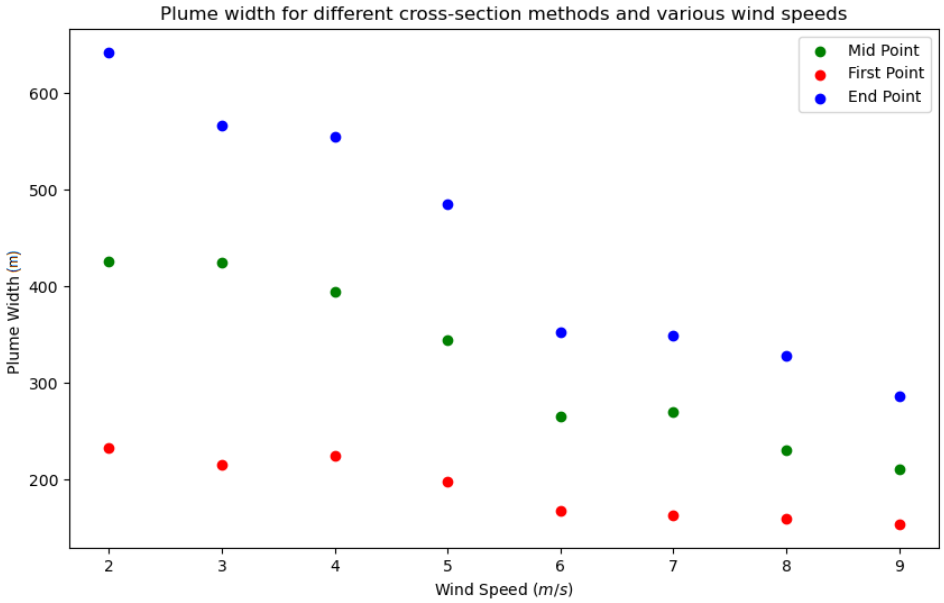

Figure 4.24: The different plume width values when various cross-section points are applied

When looking at the plumes at $2m/s$ and $9m/s$ the difference in spread can be clearly seen if. The relationship can be more carefully observed in Figure 4.25. The plot shows how the growth in plume width differs for the various wind speeds. In Table 4.15. The increase in plume width from using the first point compared to the midpoint is 36.8 % when the wind is equal to 9 m/s. When the velocity drops to 2 m/s, the growth in plume width is 82.8%. Comparing the first point method with the endpoint, the growth in plume length for 2 m/s results in a plume that is 2.75 times larger when the endpoint is used. For 9 m/s the increase is equal to 85.96%.

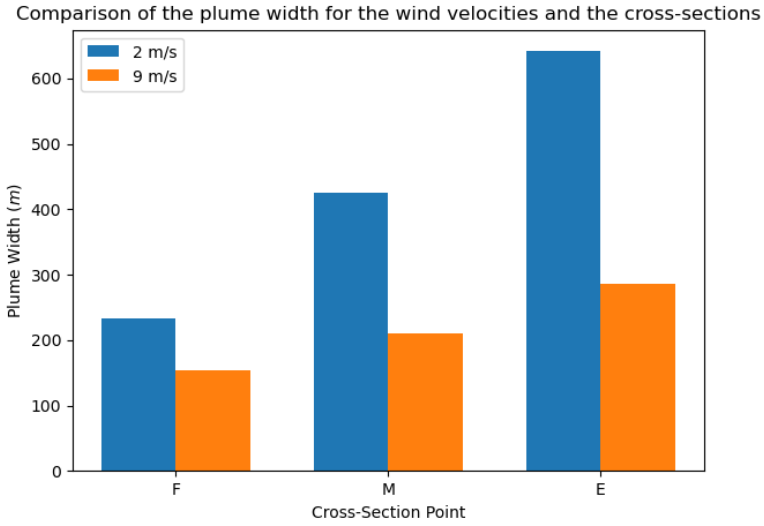

Figure 4.25: A bar chart with the plume width values when various cross-sections and wind speed points are applied

Plume Width	2 m/s	9m/s
First Point	232	153
Mid Point	425	210
Endpoint	642	285

Table 4.15: The plume widths extracted from the bar chart in Figure 4.25

5

Model Comparison With Measurements

In this chapter, the main aim is to validate the accuracy of the created COMSOL model by comparing the simulation outcomes with the experimental data collected at the Polderbaan in Schiphol. The insights gained here will illustrate the efficacy of the model. The results will consist of two main sections: Plume width and Concentration. Each of these sections will be subdivided into arrivals and departures. The data will be subjected to different statistical tests to conclude the effects of the other ambient and operational conditions.

5.1. Plume Width

In this section, the plume widths of the simulations and measurements are compared to assess how well the model can evaluate the plume evolution in terms of geometry. The plume widths for the simulation are calculated using the methodology described in subsection 3.6.1 with a threshold of 2.5% of the maximum concentration value. The methodology used is described in subsection 2.11.1, which is based on the plume duration time and the crosswind speed. An important note to remember is that the data on which this methodology is based is the particulate matter data collected by the partector as seen in subsection 2.10.1. Similar to the sensitivity analysis, the plume widths are plotted against different ambient and operational conditions to observe the possible effects.

5.1.1. Departures

The plumes of 94 different departures from the Polderbaan are simulated and compared with the measurement. Each simulation is modelled according to the aircraft specifications and ADS-B data obtained during the measurement. The ambient conditions obtained from the METAR station at Schiphol are added. The full list of different aircraft can be seen in Figure B.1. All aircraft analysed are of twin-engine type.

Wind Velocity

The experiments and the simulations were conducted under various wind conditions. The plume widths of the model and measurements can be seen in Figure 5.1. In this plot, it can be immediately seen that the model cannot reflect the measurements perfectly.

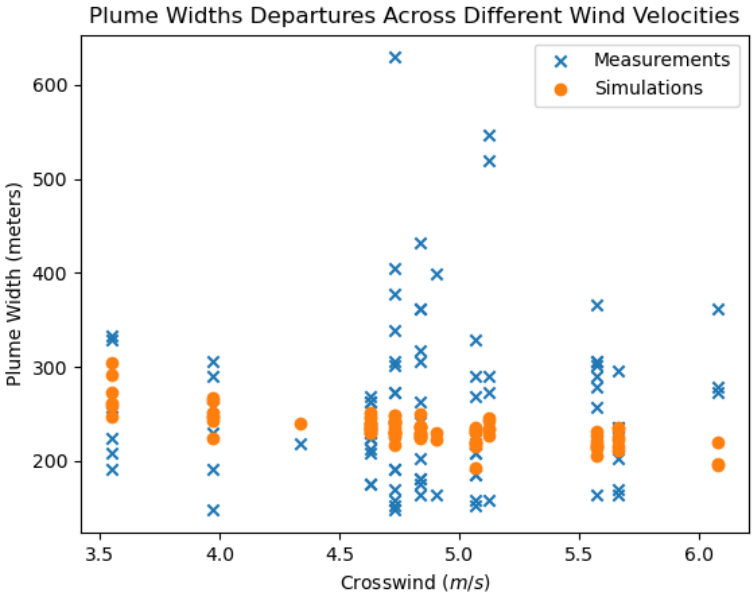

Figure 5.1: A comparison of the plume width under various wind conditions

The aim of Figure 5.1 is to be able to reflect on what influence the wind has on the plume width. Each measurement point (denoted with the X's) is a different aircraft departing under a different set of ambient conditions; as mentioned, the full list can be seen in Figure B.1. In this figure, it looks like the wind does not have a significant effect, but to be sure, a linear regression line is created for both the simulations and the measured data. The methodology behind this can be seen in subsection 2.12.5. The regression lines can be seen in Figure 5.2. The red line is the regression line calculated for the simulation data, and the blue line is the measured data. The coefficients of the regression lines can be found in the legend of the plot. Starting with the regression line for the simulations. This line shows a decreasing trend for the plume width as described in section 4.9. The data shows that wind speed is a dominant factor in determining the plume width in the model. The coefficient of determination (R^2) is also given, which is 0.58. There is some disagreement in the literature as to what value can be considered acceptable, meaning that the regression curve accurately represents the data [18, 15]. However, as wind speed is not the only variable used in the model, a coefficient of determination of 0.58 indicates a relatively strong relationship. The same cannot be said for the regression line for the measurements. The line shows a slight increasing trend, which would be remarkable given the results of the model. However, the coefficient of determination is 0.01, which means that the fit is not optimal, and therefore, no conclusions can be drawn from this relationship.

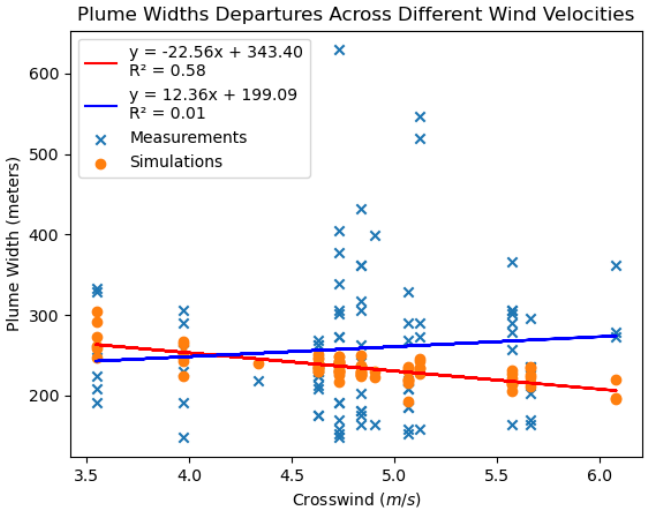

Figure 5.2: A comparison of the plume width under various wind conditions with added regression lines

Now that the effect of the wind speed has been discussed for departures, it is possible to look at the other variables regarding the operating conditions. This is seen in Figure 5.3.

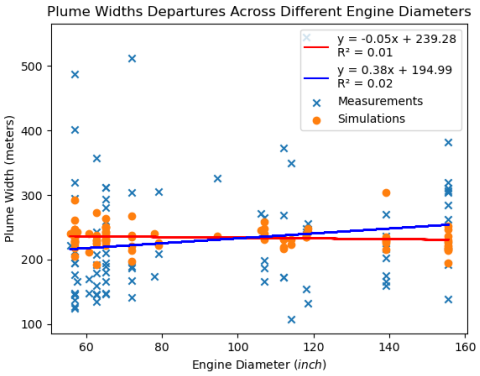

(a) A comparison of the plume width under various engine diameters with added regression line

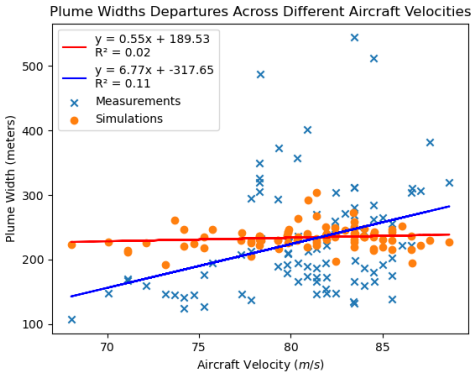

(b) A comparison of the plume width under various aircraft velocities with added regression line

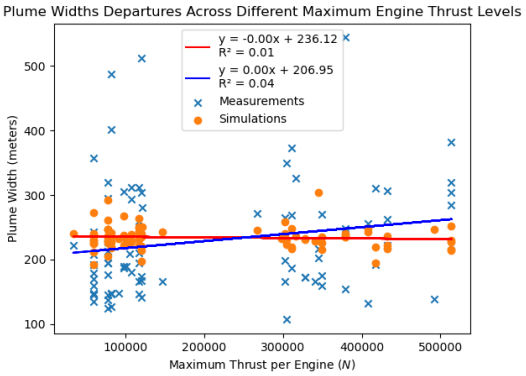

(c) A comparison of the plume width under various engine maximum thrust levels with added regression line

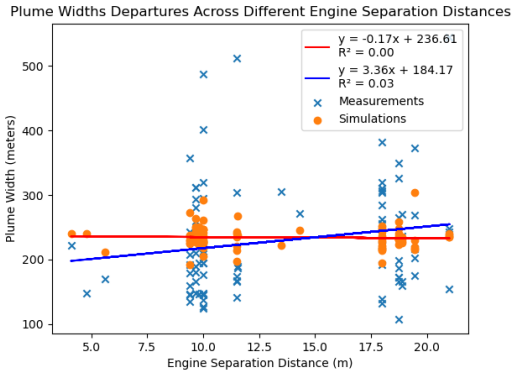

(d) A comparison of the plume width under various engine separation distances

Figure 5.3: The effect of different aircraft operating conditions on the plume width simulated and measured for departures

Engine Diameter

The next variable to be examined is engine diameter. Looking at the departures, there is a range of 18 different diameters. It is important to note that this does not mean 18 different engines, as many versions of engines are designed to have the same diameter. The different diameters that occur in the measurements and simulations are shown in Table B.1. Using the same method as for the wind speed and adding a regression line to the identified possible relationships, this gives Figure 5.3a. The first observation is that the linear regression line for the model is almost flat, with β_1 of -0.05. This would suggest that there is no relationship. This is supported by the coefficient of determination of 0.01, which means that a good fit was not found. The same can be seen for the measurements, while the regression line has a β_1 of 0.38, the coefficient of determination shows that no good fit was found. Therefore it can be said that the engine diameter does not have a significant effect on the plume width.

Aircraft Velocity

Within departures, aircraft tend to have small speed differences during take-off. This is confirmed by the ADS-B data received. It is therefore included in this analysis. The sensitivity analysis showed that it had a significant effect on the plume. So it would be interesting to see if this is the case here. The results are shown in Figure 5.3b. The model does not show a clear relationship. However, there is a slight trend in the measurements. It can be seen that the plume width increases as the aircraft speed increases. The fit is not perfect, as the coefficient of determination is only 0.11, but considering that there are many different variables involved, it does carry some weight.

Thrust Level

This variable was not included in the sensitivity analysis as it was indirectly observed through the effect of the engine exit velocity in section 4.8 on the plume. However, it was decided not to include engine exit speed in this analysis as the speed is relatively the same for all aircraft in the same mode (arriving or departing). Therefore thrust is used to see if it has an effect on plume width. Thrust values are taken from the ICAO emissions database [28]. It is important to note that the thrust levels shown are the maximum possible thrust, which is consistent with the ICAO Mode Directions [26]. The resulting plot is shown in Figure 5.3c. The regression line is flat, similar to Figure 5.3a. This indicates no clear relationship, again supported by a coefficient of determination of 0.01 and 0.04; in other words, no fit was found.

Engine Separation Distance

As shown in Figure B.1, there are many different types of aircraft used for departing plume width analysis. The design of the aircraft results in different engine separation distances. The set of aircraft used for this section of the results leads to 17 different engine separation distances. These can be seen in Table B.2. Exploring the possible relationship of this parameter to plume width leads to Figure 5.3d. The plot is consistent with the results from thrust level and engine diameter, and no real effect is observed. The regression line is flat, and a coefficient of determination of 0.00 is found for the model and 0.04 for the measurements. This indicates that no fit has been found.

Box Plot

Now that the different effects of the different variables have been identified, the next step is to directly compare the results obtained from the measurements and the simulations. This is done using a box plot. A box plot is a graphical representation that summarises the distribution of a set of data. It shows the variability and trend of the data. The body of the plot, called the box, represents the interquartile range, which extends from the first quartile (Q1) to the third quartile (Q3). Within the box, a line shows the median value of the data. Extending from the box are whiskers that reach the smallest and largest values within 1.5 times the interquartile range of Q1 and Q3, respectively, representing the range of the bulk of the data. Points outside the whiskers are considered outliers; these outliers are significantly higher or lower than the so-called bulk of the data. The plot is shown in Figure 5.4. At first sight, the variability in plume widths is much greater in the experiments than in the simulations. This is confirmed by looking at the standard deviation of both datasets. For the simulations, the standard deviation is 17.33 metres. For the measurements, it is 300.46 metres. The median of both datasets is very close to each other; for the simulations, it is 233.86 metres, and for the experiments, it is 229.34 metres. The different statistical values of both datasets can be seen in Table 5.1.

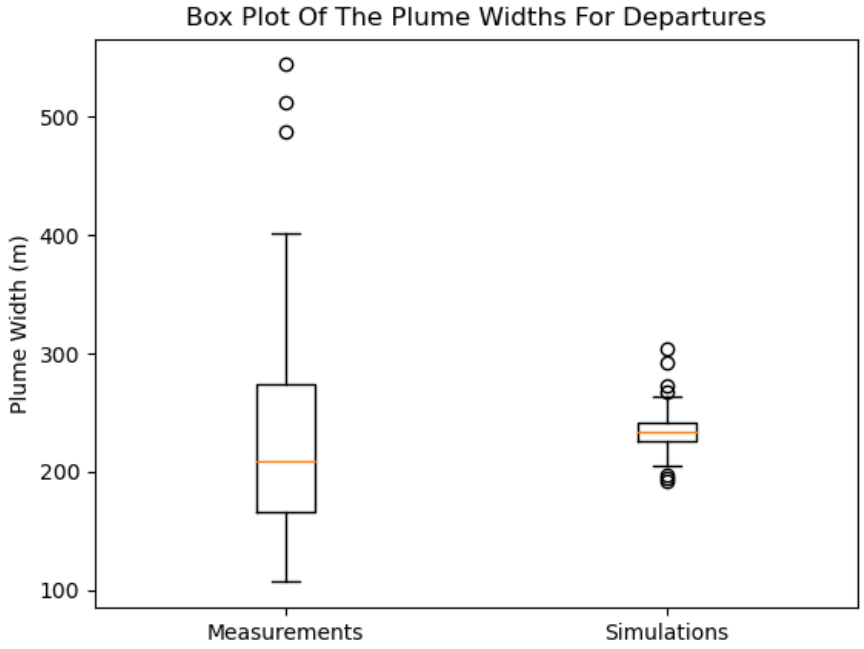

Figure 5.4: A box plot of the plume widths regarding departures

Statistics Plume Width Departures	Mean (m)	Median (m)	σ^2 (m^2)	σ (m)
Simulation	234.33	233.36	300.46	17.33
Measurements	229.34	208.86	7404.92	86.05

Table 5.1: The different statistical values of the plume widths regarding departures

Errors

Now that an overview of the plume widths of both simulation and measurement has been established, it is time to examine the error between the two sets. We start with the mean absolute error. This parameter is one of the easiest ways to observe how well the simulation is able to capture the plume width. The mean absolute error (MAE) between the model and the simulations is 72.96 metres. Another error that is looked at is the mean squared error (MSE); this method is more sensitive to larger errors. This is also seen in the result, the MSE is equal to 8232.15 metres, meaning that the larger errors have heavily influenced it. The last error considered is the Root Mean Squared Error (RMSE). This is 90.73 metres. In addition to the errors, it would also be interesting to see if the model has a tendency to over or under-estimate the plume width. This can be done using the mean bias error (MBE). If this deviation is positive, then the model is more likely to overestimate the plume width than vice versa. Looking at the mean bias deviation, it can be computed to be equal to 4.99, which means that for departures, the model overestimates the width by an average of 4.99 metres. All values can be found in Table 5.2.

Error & Bias Plume Width Departures	MAE (m)	MSE (m^2)	RMSE (m)	MBE (m)
	72.96	8232.15	90.73	4.99

Table 5.2: Table with the different errors and bias of the model considering plume width and departures

While the mean bias error gives some indication of how the model is performing there, it would also be valuable to see how the model performs when looking at different plume sizes. This can be seen using the Bland-Altman plot shown in Figure 5.5. From this plot, it can be seen that the model tends to overpredict when the plumes are smaller, as the difference in the lower left-hand area becomes negative when the mean widths of the measurement and simulation are also smaller. This trend is

reversed when the mean width of the pair increases. In this case, the model starts to underpredict the plume width compared to the measurements. This means that there is no clear systemic bias.

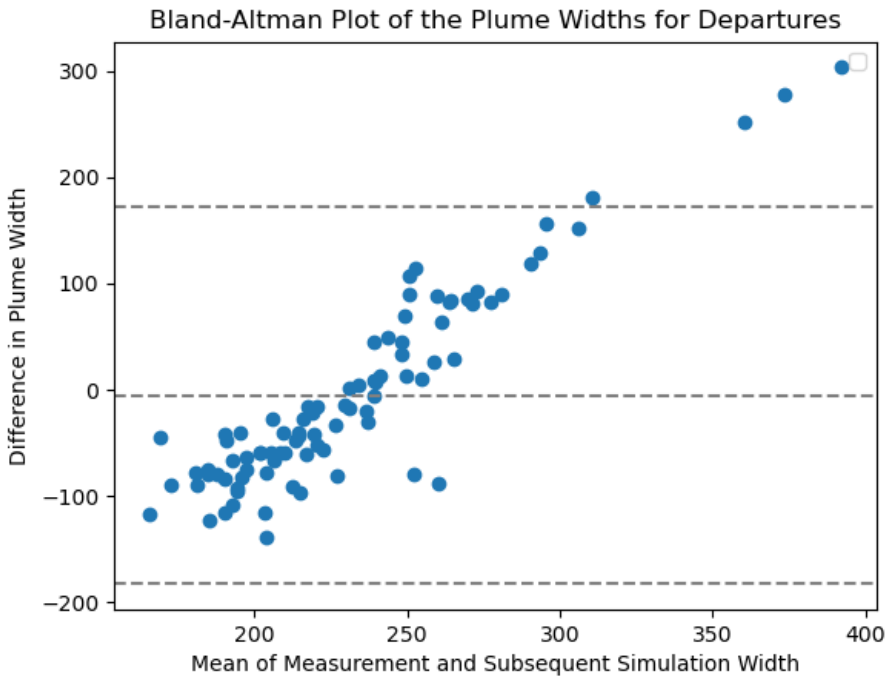

Figure 5.5: The Bland-Altman plot of the different plume widths for departing aircrafts

5.1.2. Arrivals

The plumes of 118 different arrivals from the Polderbaan are simulated and compared with the measurement. The same method is used as for departures, which means that each simulation is modelled according to the aircraft specifications and ADS-B data obtained during the measurement. The environmental conditions obtained from the METAR station at Schiphol have also been added. The full list of different aircraft can be seen in Figure B.1. The results of the plume width comparison can be found in Figure 5.6.

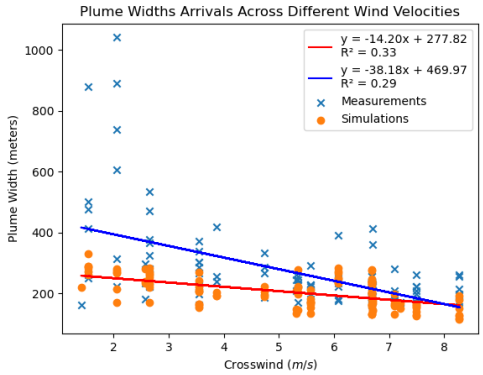

(a) A comparison of the plume width under various wind conditions

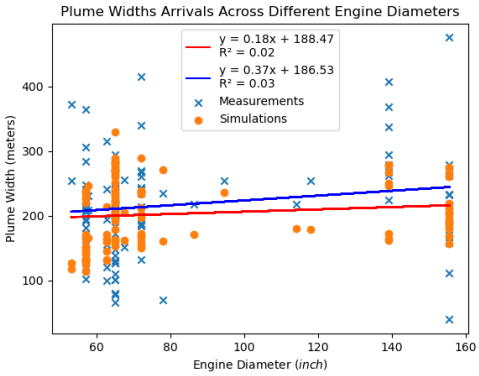

(b) A comparison of the plume width under various engine diameters

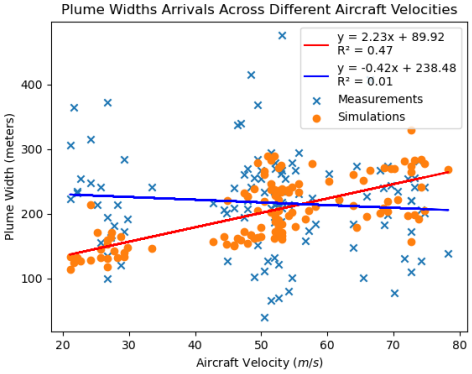

(c) A comparison of the plume width under various aircraft arrival velocities

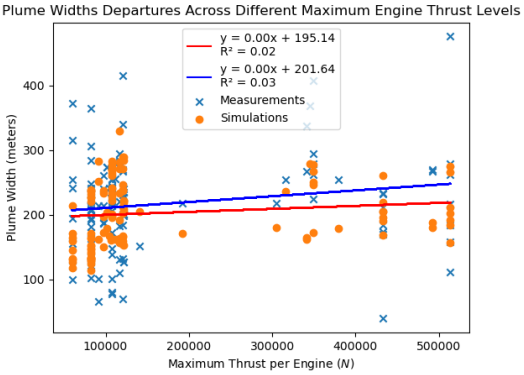

(d) A box plot of the plume widths regarding departures

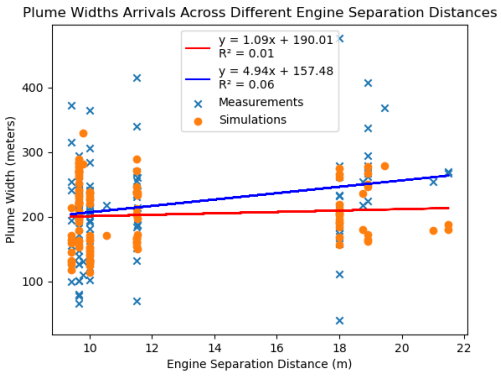

(e) fig: width arrivals separation regression

Figure 5.6: The effect of different aircraft operating conditions on the plume width simulated and measured

Wind Velocity

The analysis for the arrivals is started again with the crosswind wind speed. The plume widths of the model and the measurements can be seen in Figure 5.6a. Similar to the departures, the discrepancies between the model and the measurements are clearly visible. The linear regression line shows a downward trend, which is in line with the results for departures. The coefficient of determination is 0.33, indicating that the regression line is not perfect. However, when combined with the results from the departures, it can be said that the crosswind is a dominant factor for the model in controlling the plume width. The results from the measurements show an upward trend. A similar trend was found for the departing plumes. Contrary to the trend found in Figure 5.2, for arrivals, a downward trend can

be observed. This seems logical as the crosswind increases, the plume would pass the monitoring station more quickly and, therefore, have a smaller width. The coefficient of determination is equal to 0.29, meaning the relation found manages to describe the dataset accurately to some degree. However, since this relationship was not found for departures, one should be cautious when trying to draw conclusions from it.

Engine Diameter

Investigating the influence of the engine diameter is next. Looking at the arrivals, a range of 14 different diameters can be found. The different diameters that occur in the measurements and simulations are shown in Table B.3. The plot with the regression lines is shown in Figure 5.6b. As expected, there is no clear relationship. This is consistent with the results for departures. Both regression lines show an almost flat curve with a β_1 of 0.18, indicating a slight upward trend. However, the two exit coefficients show that no good fit was found. Combining these results with those from the departures, it can be said that engine diameter does not significantly affect plume width.

Aircraft Velocity

A slight trend was observed in the measurements when analysing departures. Although the trend was not supported by a high R^2, it would be more relevant if a similar trend were found for arrivals. The results are shown in Figure 5.6c. The first thing to notice is that the range of aircraft velocities is much wider when compared to departures. For departures this range was between 70-85 m/s. For arrivals, the range is 20-80 m/s. The trend for the model is clearly seen, with increasing velocity the width becomes larger. This is consistent with the results of the sensitivity analysis. Due to the smaller range for departures, this trend was not observed. It can also be seen that the regression line has a relatively strong coefficient of determination of 0.47, which means that the fit is acceptable. The regression line for the measurements shows no influence from speed. Combining this with the results from the departures, it can be said that speed has no real influence at this time.

Engine Thrust Level

The different thrust levels did not affect the plume width for departures. So we now need to look at arrivals. This can be seen in Figure 5.6d. There is no significant relationship, as shown by the flat regression line and the low coefficient of determination.

Engine Separation Distance

Table B.4 shows the different engine separation distances that occur. The results are plotted in Figure 5.6e. Again, the regression curve can be seen to be flat with a low coefficient of determination, meaning that engine separation distance has no real effect on plume width.

Box Plot

The influence of the different operating and environmental conditions on the arrival plume width is similar to that for departures. Except for wind speed, no real relationship is found, and the dominant parameter, especially for the model, is the crosswind. Looking at the overall distribution of plume widths for arrivals produces the same box plot. This can be seen in Figure 5.7. One thing that can be seen when comparing this figure with Figure 5.4 is that the spread of simulation widths is greater. Looking at the reasons for this, a couple of things can be seen. Firstly, the speed spread of arriving aircraft is greater than that of departing aircraft. Smaller aircraft are able to break more quickly, resulting in a lower speed. In addition, the use of reverse thrust can reduce the speed of an aircraft even faster. The statistics can be seen in Table 5.3. The mean and median of both data sets are close together, similar to the departures. However, as mentioned above, the variance and standard deviation of the simulations are larger. For arrivals, the variance is 2417.23, and the standard deviation is 49.16. Similarly to departures, the mean and median of the two simulations are relatively close. The standard deviation and variance of the measurements are close to those of the departures.

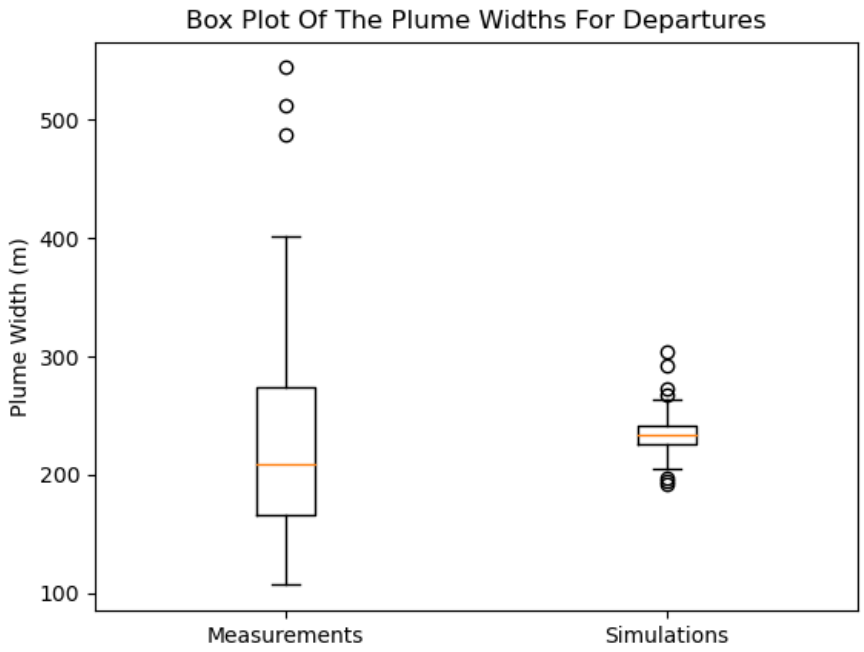

Figure 5.7: A box plot of the plume widths regarding arrivals

Statistics Plume Width Departures	Mean (m)	Median (m)	σ^2 (m^2)	σ (m)
Simulation	203.14	201.92	2417.23	49.16
Measurements	217.17	217.54	5360.66	73.21

Table 5.3: The different statistical values of the plume widths regarding arrivals

Errors

The errors of the plume widths for arrivals can be seen in Table 5.4. The mean absolute error is equal to 79.04 metres, which is slightly larger than the MAE of the departures, 72.96. As a result, the MSE and RMSE are also significantly larger. The MBD for departures was calculated to be 4.99, which means that, on average, the plume width was overestimated. For arrivals, it is -14.03, which means it underestimates the plume width.

Error & Bias Plume Width Arrivals	MAE (m)	MSE (m^2)	RMSE (m)	MBD (m)
	79.04	10226.77	101.12	-14.035

Table 5.4: Table with the different errors and bias of the model considering plume width and arrivals

It has been established that the model underestimates the plume width. Incorporating the Blant-Altman analysis allows for a more nuanced view of whether the model does this for larger or smaller-sized plumes. Table B.3 shows that the bias is not really clear. Due to the increased variance in width for both the simulation and measurement, no significant relation can be found. For smaller plumes, the model could overpredict or underpredict the width, and the same could be true for larger plumes.

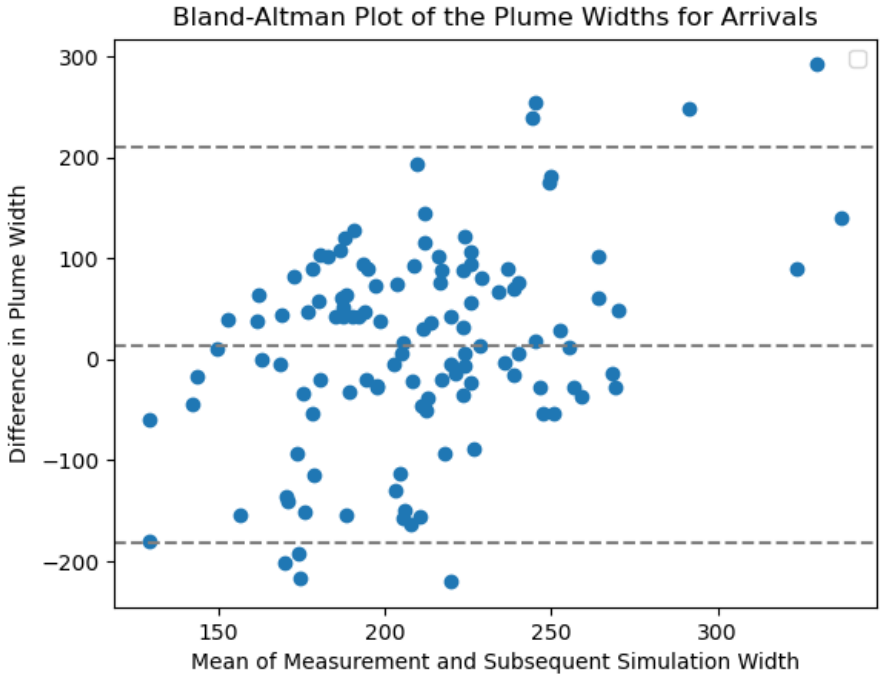

Figure 5.8: The Bland-Altman plot of the different plume widths for arriving aircraft

5.1.3. Discussion

Starting with the results of the arriving and departing aircraft seen in Table 5.5. The mean of the simulation and the measurements are very close to each other, with values of 203.34 and 217.17 metres, respectively. This shows that the model is able to accurately predict the width over multiple arrivals. The same can be seen for departures, where the mean difference is only 5.33 metres, indicating a high level of accuracy. Where the difference begins is when looking at the variance and standard deviation. The variance for the simulation of departures is 300.46, whereas for arrivals, it is 2417.23. One reason for this significant difference is the wide range of different aircraft speeds observed in the experiments. For departures, these values were much closer together than for arrivals. The measurement shows a very significant variance for both arrivals and departures, with departures being larger at 7404.92 compared to 5360.66. This shows that the model is not able to correctly simulate the variance in the different plumes that occur. There could be several reasons for this. One reason is that the parameters in the model are constant, i.e. wind speed and direction are constant, as are aircraft speed and engine speed. The changes in these parameters could affect the evolution of the plume and cause a large variance which is seen. The standard deviation follows this trend as expected. The measurements have a significant standard deviation and for the simulation this is only the case for the arrivals.

The errors shown in Table 5.6 illustrate the performance of the model. The model is slightly better at predicting the plume width of departing aircraft. The MAE is lower and the MSE is lower, indicating that not only is it performing better on average, but the size of the errors is smaller compared to arrivals. For both models it is difficult to say whether there is a systemic bias or not. For arrivals, the width is underpredicted by an average of 14.035 metres, and for departures, it is overpredicted by an average of 4.99 metres. As the variance of the measurements is so large, it cannot be said that the model has a tendency to over- or underpredict.

Results Plume Width Analysis	Operating Mode	Statistics			
		Mean (m)	Median (m)	σ^2 (m^2)	σ (m)
Simulation	Arrivals	203.34	201.92	2417.23	49.16
	Departures	234.33	233.36	300.46	17.33
Measurements	Arrivals	217.17	217.54	5360.66	73.21
	Departures	229.34	208.86	7404.92	86.05

Table 5.5: The results of the plume width simulation and measurements.

Results Plume Width Analysis	Operating Mode	Errors (Simulation versus Measurements)			
		MAE (m)	MSE (m^2)	RMSE (m)	MBD (m)
Simulation	Arrivals	79.04	10226.77	101.12	-14.035
	Departures	72.96	8232.15	90.73	4.99

Table 5.6: The errors of the simulations compared to the measurements regarding plume width.

5.2. Concentration

After completing the plume width analysis, the next step is to assess how the model is able to predict the concentration values. The concentration values compared are the maximum values of the plume seen in both the simulation and the measurements. Similarly to the plume width results, different engine types and aircraft types were considered. All the aircraft types in this analysis are twin-engine airplanes. As was mentioned earlier, three main pollutants are used for analysis: CO and NO and NO_2. The input concentration parameter is calculated using the method described in section 4.11 and specifically Equation 4.2. The rest of the parameters are the same as those used for the plume width analysis.

5.2.1. Arrivals

Starting with the arrivals. A total of 40 arrivals were studied in order. The different aircraft models can be found in Figure C.1.

CO concentration values

The first pollutant that is looked at is CO. The different measured and simulated values can be seen in Figure 5.9. The spread in values measured is larger than is seen in the simulated values. This trend is similar to what was seen in the plume width results. A large spread in plume widths was seen, which logically results in a larger spread of concentration values. The opposite is the case for the simulation results, as similar plume widths will lead to a smaller bandwidth of concentrations measured.

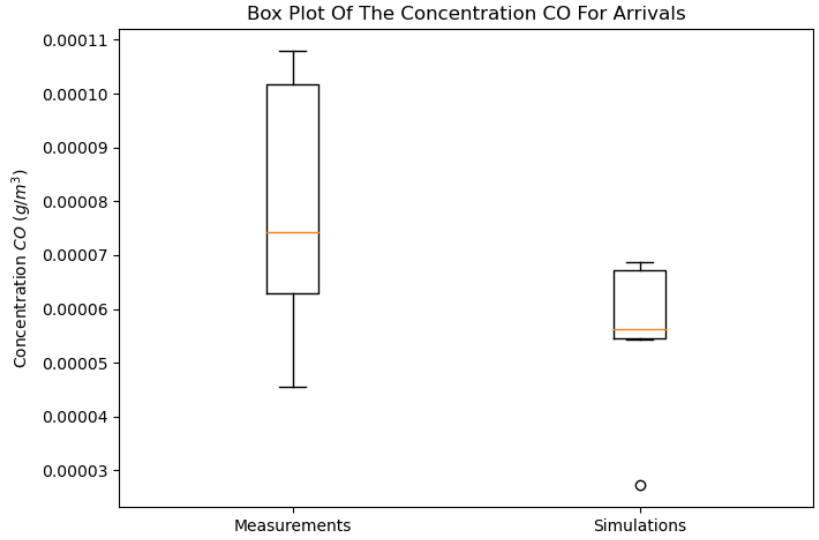

Figure 5.9: The Box plot illustrating the distribution of the concentration CO measured and simulated

The initial trend of the box plot can be seen in Table 5.7. It is seen that both the mean and the median of the measurements are around 20 $\mu g/m^3$ higher as opposed to the simulation. The spread can be best seen through the standard deviation. For the measurements, this is almost twice as high compared to the simulation.

Statistics Concentration CO Arrivals	Mean ($\mu g/m^3$)	Median ($\mu g/m^3$)	σ^2 ($\mu g^2/m^6$)	σ ($\mu g/m^3$)
Simulation	57.19	56.17	$1.44e^{-5}$	12.01
Measurements	78.21	74.34	5.31 e^{-5}	23.05

Table 5.7: The different statistical values of CO concentration regarding arrivals

The errors between the different simulation and measurement pairs are seen in Table 5.8. The mean average error is 25.72 $\mu g/m^3$. It is also seen that the model has a stronger tendency to underpredict the concentration values. The mean bias deviation is equal to 25.72 $\mu g/m^3$.

Error & Bias* CO *Concentration	MAE ($\mu g/m^3$)	MSE ($\mu g^2/m^6$)	RMSE ($\mu g/m^3$)	MBD ($\mu g/m^3$)
	25.72	$83.88e^{-4}$	28.96	-21.02

Table 5.8: Table with the different errors and bias of the model considering CO and arrivals

NO concentration values

The next pollutant is NO as was mentioned in Table 4.13. A ratio is needed as the ICAO emissions database only provides information on NO_x emittance. In contrast to CO, this pollutant undergoes chemical evolution. In the model, this is not taken into account, and therefore, it should be taken into account when assessing and discussing the results. The box plot of the simulations and measurements is seen in Figure 5.10; some outliers have been removed from this box plot, which will be explained later. The trend that can be observed is that the concentration of NO is simulated to be higher than can be seen from the measurements.

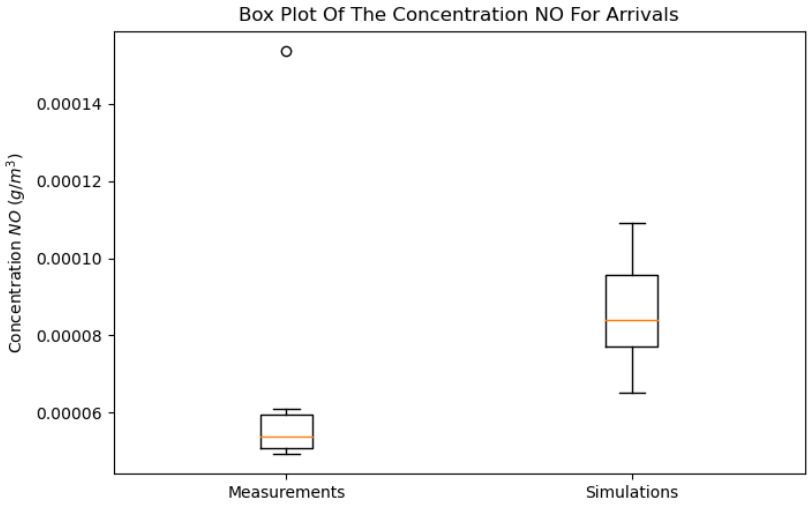

Figure 5.10: The Box plot illustrating the distribution of the concentration NO measured and simulated

The mean NO concentration of the model is equal to 86.534 $\mu g/m^3$, see Table 5.9. This is considerably higher than the results of the measurements. This is also due to the fact that the measurement results of CO are similar to those of NO, while the emission factor of NO_x for each engine is significantly higher than the emission factor of CO. This change is seen in the model but not necessarily in the measurement results.

Statistics Concentration NO Arrivals	Mean ($\mu g/m^3$)	Median ($\mu g/m^3$)	σ^2 ($\mu g^2/m^6$)	σ ($\mu g/m^3$)
Simulation	86.53	83.94	$1.10e^{-4}$	33.18
Measurements	66.42	53.79	2.11 e^{-5}	14.53

Table 5.9: The different statistical values of NO concentration regarding arrivals

The errors shown in Table 5.8 are also considerably higher compared to the CO errors in Table 5.8. This is as expected as the model is driven by higher emission factors while this is not observable in the measurements.

Error & Bias* NO *Concentration	MAE ($\mu g/m^3$)	MSE ($\mu g^2/m^6$)	RMSE ($\mu g/m^3$)	MBD ($\mu g/m^3$)
	37.93	$18.52e^{-4}$	43.05	20.08

Table 5.10: Table with the different errors and bias of the model considering NO and arrivals

NO_2 Concentration values

The last pollutant is NO_2. For this pollutant, similar results are expected as for NO. This pollutant is also driven by higher emission factors, which will lead to higher results from the model. The ratio established in Table 4.13 is used to create the distinction between NO and NO_2. This leads to the distribution seen in Figure 5.11. The estimated emissions are indeed higher than the measurement suggests.

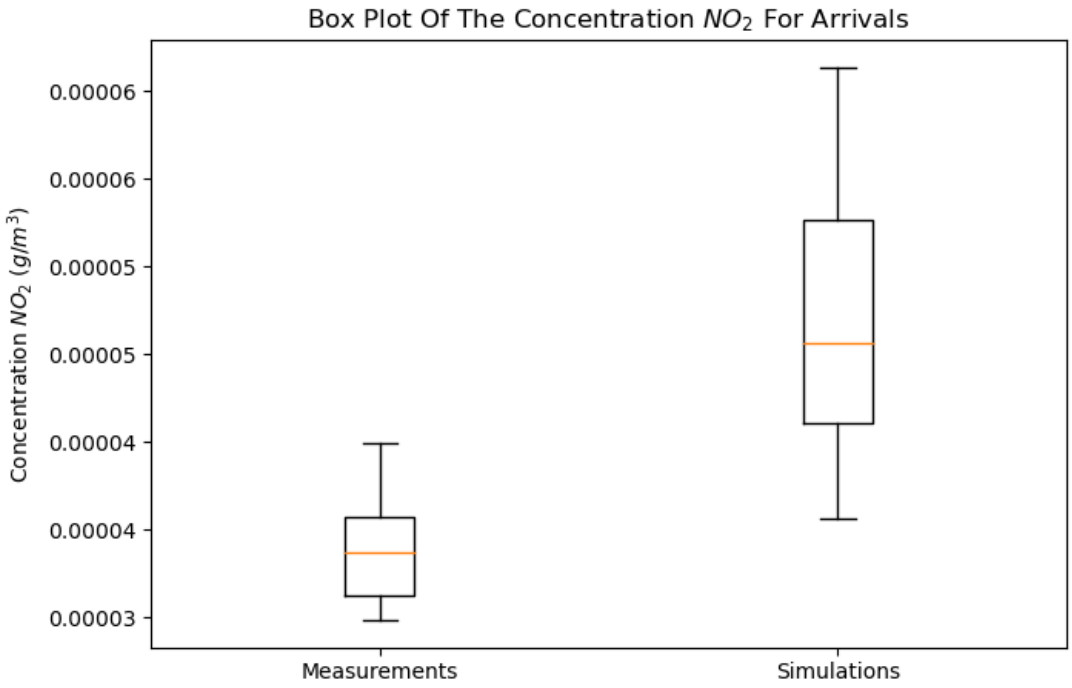

Figure 5.11: The Box plot illustrating the distribution of the concentration NO_2 measured and simulated

The model computes a higher mean concentration NO_2, 52.31 $\mu g/m^3$, which is 13.31 $\mu g/m^3$ higher than the average, which can be seen in the measurements. Both the measurements and model show a lower concentration NO_2 as is in line with the ratio NO_2/NO.

Statistics Concentration NO_2 Arrivals	Mean ($\mu g/m^3$)	Median ($\mu g/m^3$)	σ^2 ($\mu g^2/m^6$)	σ ($\mu g/m^3$)
Simulation	52.31	50.61	74.10e^{-5}	8.61
Measurements	38.99	38.69	12.02 e^{-5}	14.53

Table 5.11: The different statistical values of NO_2 concentration regarding arrivals

The errors are seen in Table 5.12; the mean average error is smaller; this is likely due to the ratio of the pollutants that were established. This means that less NO_2 is emitted, resulting in a smaller error.

Error & Bias* NO_2 *Concentration	MAE ($\mu g/m^3$)	MSE ($\mu g^2/m^6$)	RMSE ($\mu g/m^3$)	MBD ($\mu g/m^3$)
	13.31	2.54e^{-4}	15.96	13.31

Table 5.12: Table with the different errors and bias of the model considering NO_2 and arrivals

5.2.2. Discussion

In the beginning, it was stated that certain outliers were excluded. During the process of simulating and comparing results, a discrepancy was found. It was briefly touched upon already but the pollutant levels of the model are severely driven by the emission factor and fuel flow, as was seen in Equation 4.2. This leads to a very significant disagreement between the model and the measurements. This is best shown through the comparison of the data from two engines. The first engine is a CF34-8E5, this is a smaller engine with a diameter of 62.7 inches and is used for the Embraer 190STD. The other engine is the GE90-94 used on a Boeing 777. All data from the emissions databank for both engines can be seen in Table 5.13. There are several things that are important to notice. For the GE90-94B, a larger fuel flow is seen almost 6 times as large as for the CF34-8E5. In addition the emission factor for NO_x

is almost 4 times as big. This means that per second, the GE-94B emits 198.22 grams of NO_x while for the CF34-8E5, this is only 9.6304. The large engine emits around 20.5 more pollutants per second.

Engine Type	EI_{CO}	EI_{NO_x}	Fuel Flow
CF34-8E5	0.64	14.77	0.652
GE90-94B	0.12	56.41	3.514

Table 5.13: The emissions data of the CF34-8E5 and GE90-94B engine

Taking into account the insights from Table 5.13, the next step is to see what these differences have on the simulated and measured data. This is seen in Table 5.14. It is seen that the simulated plume value for the GE90-94B is drastically larger for NO_x emissions compared to the CF34-8E5 engine. However, this is not the case for the measurements. A similar plume concentration is measured for both engines. This causes a severely skewed analysis. This skewness is not limited to the GE90-94B engine but all engines which are relatively large pollutant emitters. These outliers are removed from the analysis. This means that a natural maximum thrust limit of 120kN for engines occurs, which is used for the analysis. This limit allows for a meaningful comparison of smaller engines. A side note is that this effect does not seem to occur for CO. No outliers for this pollutant are observed meaning that the input concentration method works more sufficiently when assessing CO.

Engine Type		CO	NO	NO_2
CF34-8E5	Measured ($\mu g/m^3$)	63	154	45
	Simulated ($\mu g/m^3$)	56	82	50
GE90-94B	Measured ($\mu g/m^3$)	56	48	38
	Simulated ($\mu g/m^3$)	74	580	349

Table 5.14: Simulation and Measurement data of the two engines that are being compared

The need for this time limit on engines shows that the model is extremely sensitive to the input parameter. This, combined with measurements that seem to show that a large engine does not necessarily mean a high concentration value, results in data that are difficult to compare.

5.2.3. Departures

From the arrivals, it can be seen that the model can produce plumes that carry significantly more pollutants compared to the measurements. This is due to the method surrounding the input concentration parameter. Therefore, it is interesting how this affects departures, where certain emission factors are even higher. A total of 38 departures have been looked at in this analysis. The aircraft types are seen in Figure C.2.

CO Concentration Values

The results in Figure 5.9 showed the model underpredicted the CO concentrations compared to the measurements. The results for Figure 5.12 are shown. The model shows that it produces less CO compared to arrivals. This is in line with the theory that for departures, a richer fuel ratio is used, resulting in less CO. The measurements are also lower compared to arrivals. Indicating that both values are in line with as to what is expected. The model is however lower in its estimation.

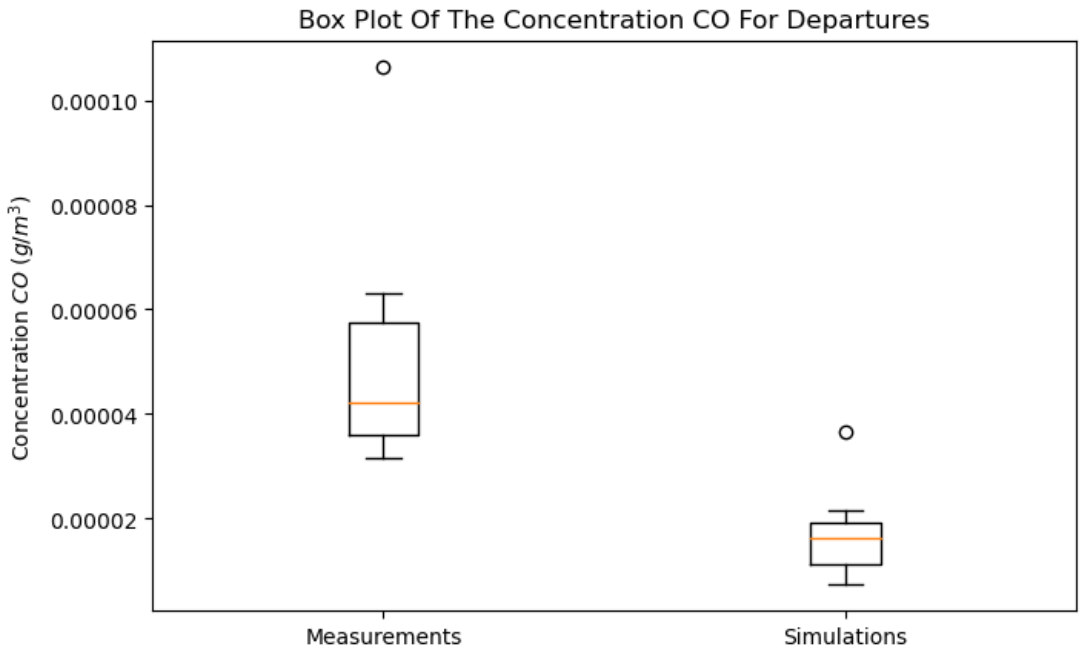

Figure 5.12: The Box plot illustrating the distribution of the concentration NO measured and simulated

The initial observations are confirmed by looking at the statistics seen in Table 5.15. The mean concentration at the experiments is around 7 $\mu g/m^3$ lower when assessing departures versus arrivals. The simulation mean has decreased significantly more with around 40 $\mu g/m^3$. The standard deviation is smaller for both simulations and measurements. This can be seen as logical due to the fact that less pollutant is expected to be emitted.

Statistics Concentration CO Departures	Mean ($\mu g/m^3$)	Median ($\mu g/m^3$)	σ^2 ($\mu g^2/m^6$)	σ ($\mu g/m^3$)
Simulation	16.83	16.37	$6.52e^{-5}$	8.07
Measurements	50.40	47.09	4.50 e^{-4}	21.22

Table 5.15: The different statistical values of CO concentration regarding arrivals

The errors have increased for CO compared to arrivals. The MAE is now equal to 33.35 $\mu g/m^3$ as seen in Table 5.16. For arrivals, the MAE is 25.72 $\mu g/m^3$. This is mainly driven by the model, which used lower emission factors for CO while the experiments showed a slight but not extreme decline. This is supported by a significant mean bias deviation of -33.56 $\mu g/m^3$.

Error & Bias* CO *Concentration	MAE ($\mu g/m^3$)	MSE ($\mu g^2/m^6$)	RMSE ($\mu g/m^3$)	MBD ($\mu g/m^3$)
	33.35	$16.44e^{-4}$	40.55	-33.56

Table 5.16: Table with the different errors and bias of the model considering NO_2 and arrivals

NO Concentration Values

The results from NO are expected to also cause outliers for engines that produce a significant amount of pollutants. When assessing the amount of pollutants, departures should show an increase of pollutants as is predicted in subsection 2.3.3. The box plot is shown in Figure 5.13. The box plot originally contained outliers caused by the large turbofan engines. This was around 15% per cent of the total data. When removing these leads to this box plot. It is also important to consider this when quantifying the errors.

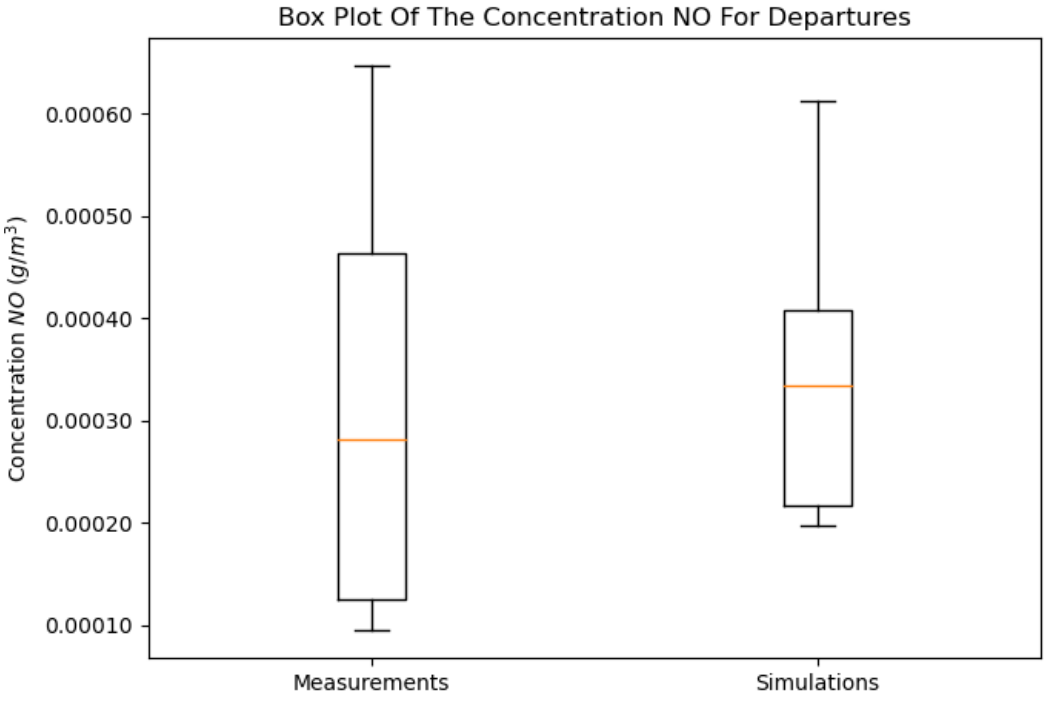

Figure 5.13: The Box plot illustrating the distribution of the concentration NO measured and simulated for departures

The amount of NO emitted has drastically increased for both the measurement and simulations when comparing it to arrivals. The mean NO of the model is 343.66 $\mu g/m^3$, seen Table 5.17. The experiments show a similar figure with 313.89 $\mu g/m^3$ of NO. This is as expected as for departures, a higher fuel-to-air ratio is used, leading to more formation of NO. The standard deviations are larger compared to arrivals, which can be seen as a result of an increase in pollutants, thus magnifying the error.

Statistics Concentration NO Departures	Mean ($\mu g/m^3$)	Median ($\mu g/m^3$)	σ^2 ($\mu g^2/m^6$)	σ ($\mu g/m^3$)
Simulation	343.66	333.79	$1.77e^{-2}$	133.06
Measurements	313.89	282.12	3.83 e^{-2}	195.76

Table 5.17: The different statistical values of NO concentration regarding arrivals

The errors are shown in Table 5.18. Due to the fact that the spread of the measurement values was larger than for the simulation, the errors are enlarged. The model had a relatively small tendency for overprediction when considering the total amount of pollutants. On average, the model overpredicted the concentration with 29.76 $\mu g/m^3$.

Error & Bias* NO *Concentration	MAE ($\mu g/m^3$)	MSE ($\mu g^2/m^6$)	RMSE ($\mu g/m^3$)	MBD ($\mu g/m^3$)
	136.74	$32.39e^{-3}$	179.97	29.76

Table 5.18: Table with the different errors and biases of the model considering NO and departures.

NO_2 Concentration Values

The same large turbofan engines are removed from the dataset. This leads to the box plot seen in Figure 5.14. It is seen that even after the outliers are removed, the model and measurements are not in total alignment. The model significantly overestimates the amount of NO_2 compared to the measurements.

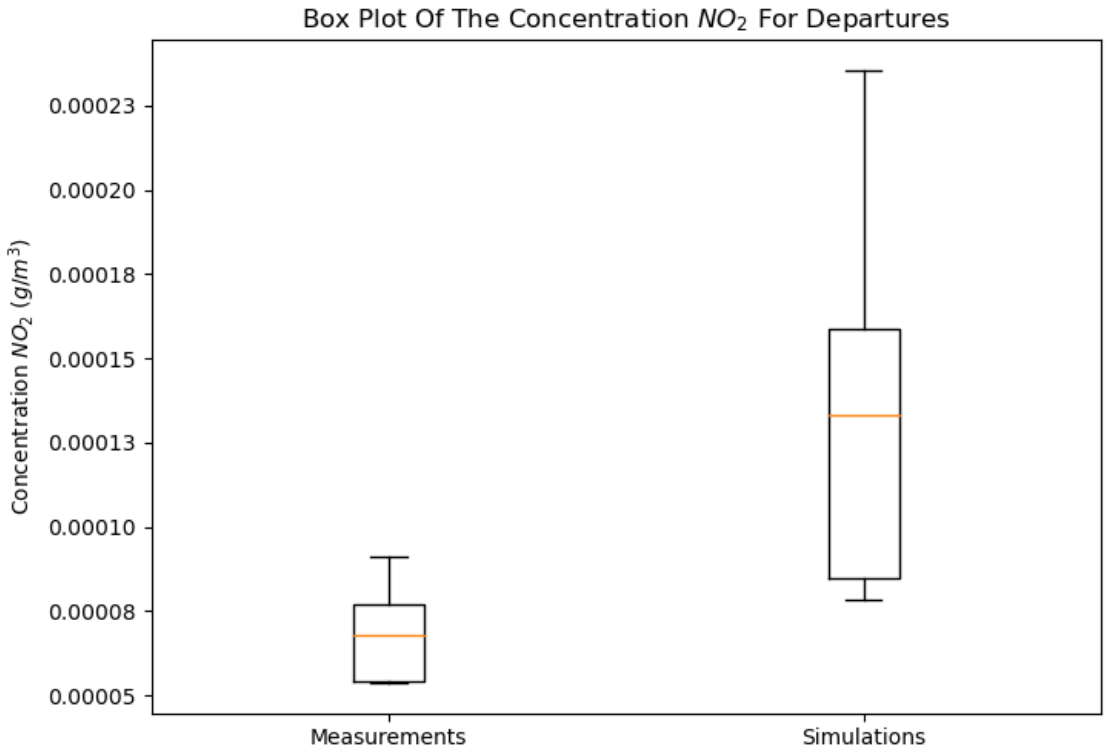

Figure 5.14: The Box plot illustrating the distribution of the concentration NO measured and simulated

The observation of the box plot is confirmed when looking at the mean of both datasets. The mean of the model shows 133.24 $\mu g/m^3$ of NO_2. This is almost double that of the measurements. Also, it is interesting to see that even without the outliers, the whiskers of the box plot are still significantly large, especially when comparing it to the box of the experiments.

Statistics Concentration NO_2 Departures	Mean ($\mu g/m^3$)	Median ($\mu g/m^3$)	σ^2 ($\mu g^2/m^6$)	σ ($\mu g/m^3$)
Simulation	134.72	133.24	$2.58e^{-3}$	50.87
Measurements	68.39	67.67	1.77 e^{-4}	13.32

Table 5.19: The different statistical values of NO_2 concentration regarding arrivals

The overprediction is also reflected in the errors shown in Table 5.20. The MAE is equal to 69.41$\mu g/m^3$. Combining this with the fact that the bias of the model is a positive quantity of 66.31$\mu g/m^3$ shows that almost all errors were due to overprediction.

Error & Bias $\mu g/m^3$ ***Concentration***	MAE ($\mu g/m^3$)	MSE ($\mu g^2/m^6$)	RMSE ($\mu g/m^3$)	MBD ($\mu g/m^3$)
	69.41	$7.07e^{-3}$	84.11	66.33

Table 5.20: Table with the different errors and bias of the model considering NO_2 and departures.

5.2.4. Discussion

As was seen for the arrival analysis, the outliers of significantly large engines posed a problem for the methodology. These were removed in order to sustain a viable comparison for the rest of the departures. Therefore, it can be said that the current method of calculating the input concentration is not a feasible solution for all types of engines. Continuing the data set with engines that are applicable to the method, several insights can be gained.

Looking at the performance of the model regarding CO, a few conclusions can be drawn. For both arrivals and departures, it can be seen that the model has a tendency to underpredict concentration. Since it is an underprediction, chemical evolution is not a suitable reason, as this would only explain if the measured concentration was lower than the model. In addition, in the model, no chemical depletion is present. However, the depletion rate of CO in the atmosphere is in the range of months, so this is unlikely to explain the difference. This means that it could be that certain operating or ambient conditions are not well integrated into the model.

NO concentration shows that the model predictions and experimental measurements align closely for departures, with the mean NO concentration from the model being 343.66$\mu g/m^3$ and from measurements being 313.89 $\mu g/m^3$. The similar values suggest that the model accurately illustrates the primary initial dispersion processes of NO. However, for arrivals, the model has a tendency to overpredict. This is not expected. During arrivals, it is expected that aircraft make use of reverse thrust, and therefore, an increase in NO could be observed. This is not the case, and the mean of the model is around 20 $\mu g/m^3$.

For NO_2, a significant discrepancy between model predictions and experimental data is seen for departures, with the model greatly overestimating the concentrations. The mean NO_2 concentration from simulations is 68.39 $\mu g/m^3$ compared to 313.89 $\mu g/m^3$ from measurements. This significant overprediction highlights potential issues with how the model and methodology handle the chemical transformation of NO to NO_2 or possibly an overestimation of initial NO emissions. The removal of large turbofan engine outliers improves the alignment but still leaves a significant overestimation by the model.

Finally, the sensors used in the experiments were low-cost devices. This means that they are likely to have some sort of bias and error. They are also susceptible to environmental factors such as temperature and humidity, which vary from experiment to experiment. The sensors may, therefore, overestimate or underestimate pollutant concentrations, leading to inaccuracies in the data collected. When comparing experimental results from these sensors with model predictions, such inaccuracies can make the model appear less accurate or hide certain trends.

6

Conclusion & Recommendations

6.1. Conclusions

In this Thesis, a computational fluid dynamics model was created using COMSOL multiphysics. The aim of this model was to simulate a plume leaving the engine during an LTO cycle. A domain was created to replicate the experimental setup accurately. The model consists of several modules, each controlling different aspects of the flow. A high Mach number flow was chosen to replicate the velocity and pressure profiles of the jet engine flow. The dilute species transport model was chosen for pollutant dispersion. After establishing a plume extraction methodology, the plume characteristics studied are the plume width and the peak concentration value. The width is chosen using qualitative rather than quantitative measures, so it is important to take this into account when evaluating the results.

The model was subjected to a sensitivity analysis, and different operating and environmental conditions were investigated. The results of this analysis show that the model is very sensitive to the mesh chosen. Especially in the early stages, it could model a plume of 225 metres using a coarse mesh down to 76 metres if a finer mesh is chosen. In the end, an adaptive mesh is chosen as this method carefully creates a fine mesh around the shape of the plume, combining accuracy with computational efficiency. Looking at the different parameters investigated, it can be seen that the largest influence is the wind speed. This causes the plume width to decrease by 3.49% for every 1 m/s increase in speed. Another important finding from the sensitivity analysis is that an increase in pollutant concentration does not cause an increase in plume width; the plume keeps the same geometric boundaries, and only the peak is increased. The question is whether this replicates real-life conditions. To try to understand this, the plume width methodology is varied. Different concentration thresholds are used, and each step of the 0.5% threshold results in a 0.77% decrease, which is not significant enough to explain no increase in plume width as the concentration is increased. This could be seen as a flaw in the internal physics of the model. Other operating conditions, such as engine diameter and engine separation distance, had some effect but were not significant compared to the other factors. Looking at the effect of aircraft speed, there is a trend of a 3.36% increase in plume width for every 5 m/s increase in aircraft speed. This effect is reflected in the results, but the question is whether this is correct. Due to the nature of the domain created in the domain, the shape of the aircraft is not taken into account. This shape will influence the airflow that would have entered the domain but is now modelled as a uniform flow related to the aircraft speed. This assumption can cause a deviation in the results as plumes from the measurements will have interfered with the turbulence wake created by the aircraft's hull.

The model's plume widths were compared with their experimental counterparts. A few things can be seen when observing the effect of the operating and ambient conditions. For departures, the model showed a strong relation with the crosswind, and a downward trend was observed, indicating that this was the dominant parameter of the model. The results shown were positive on the one hand, but on the other hand they showed that there was still room for improvement. The mean values of the experimental and model results were in close proximity to each other. For arrivals, the model showed a mean plume width of 203.34 metres, while for the experiments, this was 217.1 metres. For departures, the

model and experiments were in even better agreement, being 234.33 and 229.34, respectively. This shows that the midpoint cross-section method was not a wrong choice, as other intersection methods would lead to plume widths that would greatly vary from the experimental data. The results differ, however, when looking at figures such as the variance of the standard deviation. The variance for the measurements was 7404.92 for departures and 5360.66 for arrivals. The model shows a much smaller variance for the calculated widths, 300.46 for departures and 2417.13 for arrivals. This is confirmed by parameters such as the MAE, which is 79.04 metres for arrivals and 72.96 metres for departures. The model does not appear to be subject to such extreme variations in plume width. One reason that could explain this is that in the model, the parameters are chosen as constants, whereas in the experiments, this is not the case. Take the wind, for example; in the model, the speed and direction are modelled as constants. The METAR station only updates the wind speed and direction every half hour. This can lead to large discrepancies with the time at which the plume actually arrives. However, this does not explain the extreme variations, which are more likely to be caused by sudden increases or decreases in wind speed as the plume moves. When the plume reaches the monitoring station and is then subjected to changes, this can cause the plume to either expand as the wind speed decreases or contract as the wind speed increases.

The concentration results of the model showed that the intricate dispersion and parameter methodology could still be improved. The input concentration method that was used proved to be a viable option for jet engines that were not classified as extremely large. If these outliers were removed, the model performed acceptable. For CO, it was seen that for arrivals, the model was able to perform well; only a slight underprediction was seen. Departures saw a larger underprediction by the model, indicating that it could be that for departures, the model is not as feasible as its arrival counterpart. The results of NO make it difficult to draw clear conclusions. Assumptions had to be made on how much of the pollutant would chemically evolve to NO_2. For departures, the model was able to accurately predict the concentration. This is not quite as expected, as due to the influence of reverse thrust, it would be more likely to see the value of the measurements be higher than the simulation. The model shows an overestimation of NO_2, which could mean that too many species are assumed to evolve and are entered as input parameters.

6.2. Future Recommendations

Several recommendations could be made based on the observation and evaluation of the work done. One aspect that has been discussed is the problem of translating variable parameters from the experimental setup to constant parameters in the model. In particular, wind speed has a large effect on the model. One way to solve this is to make adjustments to the measuring station. More specifically, a wind vane and an anemometer were added. One of the final measurements added this, but the data was not used for analysis in this Thesis. It would be valuable to analyse this as well. This method allows for fewer discrepancies as one is not dependent on the METAR station, which has a resolution of 30 minutes when providing meteorological data. Using these new sensors, it is possible to observe whether wind changes occur when the plume has already reached the measurement station. An average wind speed and direction can then be considered as input. Another adjustment that can be made is to add a microphone to the station. This microphone can be used to identify aircraft using reverse thrust on arrival. This can compare and assess the impact on plume width and pollutant concentration with a 'standard' landing. These two adaptations will help improve the understanding of plume evolution and quantify the impact of LTO on air quality around airports.

There are also recommendations for the evaluation of the plume model. The first obvious step would be to extend the model to a 3D environment and evaluate the different results this would produce. However, it is important to note that this would dramatically increase the computational time required for a simulation. It would, therefore, be wise to try to run it on the supercomputer servers provided by TU Delft. A 3D model would allow for the integration of plume rise, which is impossible in the current model. The plume rise is an important part of how the plume progresses along the runway, and therefore, it would be interesting to include this. The evaluation of the different components used by the model quickly leads to the chosen turbulence model. The Spalart-Allmaras model was chosen, and based on the domain considered and the results seen, it can be considered a reasonable choice. However,

it may be interesting to modify this model and try to explore the changes observed; for example, a $\kappa - \epsilon$ or $\kappa - \omega$ turbulence model can be integrated to understand its effects. Another angle that can be explored is to try to model the aircraft as a moving point source along the runway instead of a stationary source. Currently, the LTO is translated into a stationary plume, but this neglects effects such as the plume being blown into itself by the ambient wind, causing an accumulation of pollutants. If the same 2D model is chosen to continue, there are a few modifications that could be interesting to incorporate. A simple aircraft geometry can be added to mimic the effect an aircraft has on the flow passing its hull. By adding this, it is possible to understand the effect of the flow disturbance on the plume forming behind the aircraft. Also, when looking critically at the flow exiting a jet engine, two different flows can be observed. One is the flow leaving the core, which is also the flow containing the pollutants. The other is the flow from the surrounding flow, and these two flows also have different velocities [29]. This distinction could be incorporated into the model to see what effect, if any, it will have. All simulated plumes were assumed to be fully developed. However, at higher wind speeds, the plume could reach the monitoring station faster than the time it takes to develop. Therefore, it is possible to try to replicate the study for different plume development times. It may be that the model can better reproduce the variability of the measurements if different development times are chosen. The plume width methodology could also be changed. Currently, it is set at 2.5% of the peak concentration, but this could lead to an error in the assessment of much larger peaks. It might be better to try to set a benchmark concentration value that is independent of the plume peak. This way, all plumes are treated equally.

When assessing the results from the concentrations, a few things stand out. The first recommendation would be to try different methods of establishing the input concentration parameter. Preferably, a method that is not dependent on a certain volume as this can introduce problems, as was seen with the larger engines. Also, it could be interesting to try to vary the emission factors in a way that replicates real-life scenarios. For example, departures is modelled as 100% thrust, however it could also be interesting to model this as 85%, as this is often more close to what happens during the LTO. These types of adjustments can have a big impact on concentration output and would be good to study.

Finally, due to the computational load of the simulations, not an enormous amount of landings and arrivals have been considered. For the plume width, this was 118 and 94 for arrivals and departures, respectively. When looking at the concentration, this number decreased to 41 and 38, respectively. It would be interesting to increase this number as new data analysis methods could be used. For example, it would be able to analyse the plume of the same engine during different landings. This would give a distribution on the variance a plume can have when it has the same jet engine as its origin.

References

[1] *Aircraft Thrust Reversers*. Aircraft Systems. URL: http://www.aircraftsystemstech.com/p/thrust-reversers-as-aircraft-have.html (visited on 04/26/2023).

[2] *Aviation & Emissions A primer*. FAA, 2005. URL: https://www.faa.gov/regulations_policies/policy_guidance/envir_policy/media/aeprimer.pdf (visited on 03/28/2023).

[3] Niels B. *Polderbaan*. In: *Wikipedia*. Page Version ID: 66277276. Nov. 9, 2023. URL: https://nl.wikipedia.org/w/index.php?title=Polderbaan&oldid=66277276 (visited on 12/14/2023).

[4] Steven R.H. Barrett, Rex E. Britter, and Ian A. Waitz. "Impact of aircraft plume dynamics on airport local air quality". In: *Atmospheric Environment* 74 (Aug. 2013), pp. 247–258. ISSN: 13522310. DOI: 10.1016/j.atmosenv.2013.03.061. URL: https://linkinghub.elsevier.com/retrieve/pii/S1352231013002458 (visited on 01/12/2023).

[5] Katja M. Bendtsen et al. "A review of health effects associated with exposure to jet engine emissions in and around airports". In: *Environmental Health* 20.1 (Dec. 2021), p. 10. ISSN: 1476-069X. DOI: 10.1186/s12940-020-00690-y. URL: https://ehjournal.biomedcentral.com/articles/10.1186/s12940-020-00690-y (visited on 01/12/2023).

[6] Marika Berglund et al. "Health risk evaluation of nitrogen oxides". In: *Scandinavian Journal of Work, Environment & Health* 19 (1993). Publisher: Scandinavian Journal of Work, Environment & Health, pp. 1–72. ISSN: 0355-3140. URL: https://www.jstor.org/stable/40958887 (visited on 03/28/2023).

[7] Boeing. *737 Max airplane characteristics for airport planning*. Aug. 2017. URL: https://edisciplinas.usp.br/pluginfile.php/4263376/mod_resource/content/1/B737%20Max.pdf (visited on 04/26/2024).

[8] Boeing. *787 Airplane Characteristics for Airport Planning*. Mar. 2014. URL: https://d3n8a8pro7vhmx.cloudfront.net/scec/pages/1599/attachments/original/1506567348/AEIS-Submission-SCEC-Attachment-3-787-Airport-Planning-Requirements-Mar-2014.pdf?1506567348 (visited on 04/26/2024).

[9] Elissavet Bossioli et al. "Issues related to aircraft take-off plumes in a mesoscale photochemical model". In: *Science of The Total Environment* 456-457 (July 1, 2013), pp. 69–81. ISSN: 0048-9697. DOI: 10.1016/j.scitotenv.2013.02.091. URL: https://www.sciencedirect.com/science/article/pii/S0048969713002763 (visited on 06/19/2024).

[10] Régis Briant et al. "An improved line source model for air pollutant dispersion from roadway traffic". In: *Atmospheric Environment* 45 (Aug. 1, 2011), pp. 4099–4107. DOI: 10.1016/j.atmosenv.2010.11.016.

[11] *Briggs plume rise equation*. URL: https://www.envis.org/technology/air-pollution/951-briggs-plume-rise-equation (visited on 06/12/2023).

[12] Mattia Cattaneo et al. "Airports and population density: where benefits outweigh costs". In: *Regional Studies* 57.3 (Mar. 4, 2023). Publisher: Routledge _eprint: https://doi.org/10.1080/00343404.2022.2060957, pp. 576–589. ISSN: 0034-3404. DOI: 10.1080/00343404.2022.2060957. URL: https://doi.org/10.1080/00343404.2022.2060957 (visited on 02/20/2023).

[13] Etienne Coetzee. *Modelling and nonlinear analysis of aircraft ground manoeuvres*. Jan. 1, 2011.

[14] COMSOL. *Theory for the High Mach Number Flow Interfaces*. URL: https://doc.comsol.com/5.5/doc/com.comsol.help.cfd/cfd_ug_fluidflow_high_mach.08.25.html (visited on 04/17/2024).

[15] J. A. Cornell. "Factors that Influence the Value of the Coefficient of Determination in Simple Linear and Nonlinear Regression Models". In: *Phytopathology* 77.1 (1987), p. 63. ISSN: 0031949X. DOI: 10.1094/Phyto-77-63. URL: http://www.apsnet.org/publications/phytopathology/backissues/Documents/1987Abstracts/Phyto77_63.htm (visited on 06/05/2024).

[16] N. A. Cumpsty. *Jet Propulsion: A Simple Guide to the Aerodynamic and Thermodynamic Design and Performance of Jet Engines*. Google-Books-ID: yy2YoIKDC3gC. Cambridge University Press, Aug. 14, 2003. 326 pp. ISBN: 978-0-521-54144-2.

[17] G. A. Davidson. “Gaussian versus top-hat profile assumptions in integral plume models”. In: *Atmospheric Environment (1967)* 20.3 (Jan. 1, 1986), pp. 471–478. ISSN: 0004-6981. DOI: 10.1016/0004-6981(86)90087-9. URL: https://www.sciencedirect.com/science/article/pii/0004698186900879 (visited on 11/15/2023).

[18] Alessandro Di Bucchianico. “Coefficient of Determination (R2)”. In: *Encyclopedia of Statistics in Quality and Reliability*. _eprint: https://onlinelibrary.wiley.com/doi/pdf/10.1002/9780470061572.eqr173. John Wiley & Sons, Ltd, 2008. ISBN: 978-0-470-06157-2. DOI: 10.1002/9780470061572.eqr173. URL: https://onlinelibrary.wiley.com/doi/abs/10.1002/9780470061572.eqr173 (visited on 06/05/2024).

[19] EASA. *Type Certificate Data Sheets (TCDS) | EASA*. URL: https://www.easa.europa.eu/en/document-library/type-certificates (visited on 04/15/2024).

[20] European Aviation Safety Agency. and European Environment Agency. *European aviation environmental report 2019.* LU: Publications Office, 2019. URL: https://data.europa.eu/doi/10.2822/309946 (visited on 03/30/2023).

[21] David Gillen and Holger Hinsch. “Measuring the economic impact of liberalization of international aviation on Hamburg airport”. In: *Journal of Air Transport Management*. Proceedings of the Hamburg Aviation Conference 2000 7.1 (Jan. 1, 2001), pp. 25–34. ISSN: 0969-6997. DOI: 10.1016/S0969-6997(00)00025-9. URL: https://www.sciencedirect.com/science/article/pii/S0969699700000259 (visited on 02/20/2023).

[22] Rik Goudswaard. “Characterising emission plumes of individual aircraft operations using low-cost sensor nodes”. Thesis. Delft: TU Delft, Oct. 7, 2023.

[23] Scott C. Herndon et al. “NO and NO2 Emission Ratios Measured from In-Use Commercial Aircraft during Taxi and Takeoff”. In: *Environmental Science & Technology* 38.22 (Nov. 1, 2004). Publisher: American Chemical Society, pp. 6078–6084. ISSN: 0013-936X. DOI: 10.1021/es049701c. URL: https://doi.org/10.1021/es049701c (visited on 06/19/2024).

[24] Victor Albert Walter Hillier. *Fundamentals of Motor Vehicle Technology*. Google-Books-ID: 2_QQtv4pFoIC. Nelson Thornes, 1991. 506 pp. ISBN: 978-0-7487-0531-3.

[25] Simone Hochgreb. “Chapter 6 - Combustion-Related Emissions in SI Engines”. In: *Handbook of Air Pollution From Internal Combustion Engines*. Ed. by Eran Sher. San Diego: Academic Press, Jan. 1, 1998, pp. 118–170. ISBN: 978-0-12-639855-7. DOI: 10.1016/B978-012639855-7/50045-4. URL: https://www.sciencedirect.com/science/article/pii/B9780126398557500454 (visited on 01/08/2024).

[26] ICAO. *Air Quality Manual*. 2. ICAO, 2020. URL: https://www.icao.int/publications/documents/9889_cons_en.pdf (visited on 03/30/2023).

[27] ICAO. *Future of Aviation*. URL: https://www.icao.int/Meetings/FutureOfAviation/Pages/default.aspx (visited on 01/16/2023).

[28] ICAO. *ICAO Aircraft Engine Emissions Databank*. EASA. 2023. URL: https://www.easa.europa.eu/en/domains/environment/icao-aircraft-engine-emissions-databank (visited on 11/07/2023).

[29] James F. Marchman Iii. “Chapter 2. Propulsion”. In: (Aug. 6, 2021). Book Title: Aerodynamics and Aircraft Performance, 3rd edition Publisher: James F. Marchman III in association with the University Libraries at Virginia Tech. URL: https://pressbooks.lib.vt.edu/aerodynamics/chapter/chapter-2-propulsion/ (visited on 06/16/2024).

[30] IPCC. *Aviation and the Global Atmosphere*. IPCC. URL: https://www.grida.no/climate/ipcc/aviation/111.htm (visited on 03/27/2023).

[31] Dedoussi Irene. *Air_Quality_Part_02_Dedoussi_handout - AE4462-17 Aircraft Emissions and Climate Effects (2021/22 Q3)*. URL: https://brightspace.tudelft.nl/d2l/le/content/398029/viewContent/2618836/View (visited on 04/04/2023).

[32] Doğuşhan Kılıç et al. “Identification of secondary aerosol precursors emitted by an aircraft turbofan”. In: *Atmospheric Chemistry and Physics* 18.10 (May 28, 2018). Publisher: Copernicus GmbH, pp. 7379–7391. ISSN: 1680-7316. DOI: 10.5194/acp-18-7379-2018. URL: https://acp.copernicus.org/articles/18/7379/2018/ (visited on 01/08/2024).

[33] KLM. *KLM’s Embraer 175 specifications and seat map - KLM Netherlands*. KLM’s Embraer 175 specifications and seat map - KLM Netherlands. URL: https://www.klm.nl/en/information/travel-class-extra-options/aircraft-types/embraer-175 (visited on 04/26/2024).

[34] Cedomir Kostic. “Review of the Spalart-Allmaras turbulence model and its modifications to three-dimensional supersonic configurations”. In: *Scientific Technical Review* 65 (Jan. 1, 2015), pp. 43–49. DOI: 10.5937/STR1501043K.

[35] Anne Gunn Kraabøl et al. “Modelling chemistry in aircraft plumes 1: comparison with observations and evaluation of a layered approach”. In: *Atmospheric Environment* 34.23 (Jan. 1, 2000), pp. 3939–3950. ISSN: 1352-2310. DOI: 10.1016/S1352-2310(00)00156-4. URL: https://www.sciencedirect.com/science/article/pii/S1352231000001564 (visited on 04/18/2024).

[36] David S. Lee et al. “Aviation and global climate change in the 21st century”. In: *Atmospheric Environment* 43.22 (July 1, 2009), pp. 3520–3537. ISSN: 1352-2310. DOI: 10.1016/j.atmosenv.2009.04.024. URL: https://www.sciencedirect.com/science/article/pii/S1352231009003574 (visited on 04/12/2023).

[37] Brian S. Levine and H. Oliver Gao. “Aircraft Taxi-Out Emissions at Congested Hub Airports and Implications for Aviation Emissions Reduction in the United States”. In: Transportation Research Board 86th Annual MeetingTransportation Research Board. Number: 07-2860. 2007. URL: https://trid.trb.org/View/802435 (visited on 01/08/2024).

[38] J Maes. “Quantification of Aviation’s Impact on Air Quality near Schiphol Airport using Low-Cost Gas Sensors”. Thesis. TU Delft, June 18, 2021.

[39] W. J. Massman. “A review of the molecular diffusivities of H2O, CO2, CH4, CO, O3, SO2, NH3, N2O, NO, and NO2 in air, O2 and N2 near STP”. In: *Atmospheric Environment* 32.6 (Mar. 1, 1998), pp. 1111–1127. ISSN: 1352-2310. DOI: 10.1016/S1352-2310(97)00391-9. URL: https://www.sciencedirect.com/science/article/pii/S1352231097003919 (visited on 04/17/2024).

[40] Anna Magdalena Matulka et al. “On the entrainment coefficient in a forced plume: Quantitative effects of source parameter”. In: *Non Linear proceses in Geophysics* 21 (Feb. 24, 2014), p. 1. DOI: 10.5194/npg-21-269-2014.

[41] M. Mazaheri, G. R. Johnson, and L. Morawska. “Particle and Gaseous Emissions from Commercial Aircraft at Each Stage of the Landing and Takeoff Cycle”. In: *Environmental Science & Technology* 43.2 (Jan. 15, 2009). Publisher: American Chemical Society, pp. 441–446. ISSN: 0013-936X. DOI: 10.1021/es8013985. URL: https://doi.org/10.1021/es8013985 (visited on 02/20/2023).

[42] Nate Meier. *Jet-Engine.net*. 2021. URL: https://www.jet-engine.net/ (visited on 05/29/2024).

[43] Naneos. *naneos - miniature nanoparticle detectors made in Switzerland*. URL: https://www.naneos.ch/index.html (visited on 12/19/2023).

[44] NASA. *Isentropic Flow Equations*. URL: https://www.grc.nasa.gov/www/k-12/airplane/isentrop.html (visited on 04/16/2024).

[45] NASA. *Navier-Stokes Equations*. URL: https://www.grc.nasa.gov/www/k-12/airplane/nseqs.html (visited on 01/04/2024).

[46] NASA. *Role of Mach Number in Compressible Flows*. URL: https://www.grc.nasa.gov/www/k-12/airplane/machrole.html (visited on 04/17/2024).

[47] OECD. *Non-exhaust Particulate Emissions from Road Transport: An Ignored Environmental Policy Challenge*. OECD, Dec. 7, 2020. ISBN: 978-92-64-45244-2 978-92-64-88885-2 978-92-64-90102-5 978-92-64-50119-5. DOI: 10.1787/4a4dc6ca-en. URL: https://www.oecd-ilibrary.org/environment/non-exhaust-particulate-emissions-from-road-transport_4a4dc6ca-en (visited on 04/07/2023).

[48] F. Pasquill and F. B. Smith. *Atmospheric Diffusion*. Google-Books-ID: LFgRAQAAIAAJ. E. Horwood, 1983. 448 pp. ISBN: 978-0-85312-426-9.

[49] Colin Rice. “Restricting Use of Reverse Thrust as an Emissions Reduction Strategy”. In: *Transportation Research Record* 1788.1 (Jan. 1, 2002). Publisher: SAGE Publications Inc, pp. 124–131. ISSN: 0361-1981. DOI: 10.3141/1788-16. URL: https://doi.org/10.3141/1788-16 (visited on 01/15/2024).

[50] Theo Rindlisbacher and S Daniel Jacob. “NEW PARTICULATE MATTER STANDARD FOR AIRCRAFT GAS TURBINE ENGINES”. In: *ICAO Environmental Report* 2 (), pp. 85–88.

[51] Marc J. Rogoff and Francois Screve. “Chapter 8 - Permitting issues”. In: *Waste-to-Energy (Second Edition)*. Ed. by Marc J. Rogoff and Francois Screve. Oxford: William Andrew Publishing, Jan. 1, 2011, pp. 89–116. ISBN: 978-1-4377-7871-7. DOI: 10.1016/B978-1-4377-7871-7.10008-5. URL: https://www.sciencedirect.com/science/article/pii/B9781437778717100085 (visited on 03/28/2023).

[52] *Rzjets Aircraft Database*. May 28, 2024. URL: https://rzjets.net/aircraft/ (visited on 05/06/2024).

[53] Meghdad Saffaripour et al. “A review on the morphological properties of non-volatile particulate matter emissions from aircraft turbine engines”. In: *Journal of Aerosol Science* 139 (Jan. 2020), p. 105467. ISSN: 00218502. DOI: 10.1016/j.jaerosci.2019.105467. URL: https://linkinghub.elsevier.com/retrieve/pii/S0021850219305713 (visited on 01/12/2023).

[54] Schiphol. *Schiphol | Hoe groot is Schiphol eigenlijk?* Schiphol. May 3, 2024. URL: https://www.schiphol.nl/nl/blog/hoe-groot-is-schiphol-eigenlijk/ (visited on 05/14/2024).

[55] K. R. Sreenivas and Ajay K. Prasad. “Vortex-dynamics model for entrainment in jets and plumes”. In: *Physics of Fluids* 12.8 (Aug. 2000), pp. 2101–2107. ISSN: 1070-6631, 1089-7666. DOI: 10.1063/1.870455. URL: http://aip.scitation.org/doi/10.1063/1.870455 (visited on 01/12/2023).

[56] Brian Stacey, Roy M. Harrison, and Francis D. Pope. “Evaluation of aircraft emissions at London Heathrow Airport”. In: *Atmospheric Environment* 254 (June 1, 2021), p. 118226. ISSN: 1352-2310. DOI: 10.1016/j.atmosenv.2021.118226. URL: https://www.sciencedirect.com/science/article/pii/S1352231021000443 (visited on 06/19/2024).

[57] M. E. J. Stettler. “Global Civil Aviation Black Carbon Particle Mass and Number Emissions”. In: 2015 (Dec. 1, 2015). Conference Name: AGU Fall Meeting Abstracts ADS Bibcode: 2015AGUFM.A11S..05S, A11S–05. URL: https://ui.adsabs.harvard.edu/abs/2015AGUFM.A11S..05S (visited on 04/07/2023).

[58] *Sulfur in Jet Fuel by ASTM D4294*. URL: https://www.xos.com/petroleum/sulfur-in-jet-fuel (visited on 03/28/2023).

[59] *The Reynolds-Averaged Navier-Stokes (RANS) Equations and Models*. URL: https://resources.system-analysis.cadence.com/blog/msa2021-the-reynolds-averaged-navier-stokes-rans-equations-and-models (visited on 01/04/2024).

[60] OAR US EPA. *Technical Overview of Volatile Organic Compounds*. Aug. 18, 2014. URL: https://www.epa.gov/indoor-air-quality-iaq/technical-overview-volatile-organic-compounds (visited on 03/28/2023).

[61] Daniel A. Vallero. “Chapter 6 - Physical transport of air pollutants”. In: *Air Pollution Calculations (Second Edition)*. Ed. by Daniel A. Vallero. Elsevier, Jan. 1, 2024, pp. 163–190. ISBN: 978-0-443-13987-1. DOI: 10.1016/B978-0-443-13987-1.00017-X. URL: https://www.sciencedirect.com/science/article/pii/B978044313987100017X (visited on 05/13/2024).

[62] Georgy Vedeshkin, Evgeniy Sverdlov, and Alexey Dubovitsky. “Experimental Investigation of a Low-Emission Combustor Designed for MID Power Gas Turbine”. In: (June 1, 2016). DOI: 10.12762/2016.AL11-11.

[63] WHO. *What are the WHO Air quality guidelines?* URL: https://www.who.int/news-room/feature-stories/detail/what-are-the-who-air-quality-guidelines (visited on 05/28/2024).

[64] WHO. *WHO global air quality guidelines: particulate matter (PM2.5 and PM10), ozone, nitrogen dioxide, sulfur dioxide and carbon monoxide*. Sept. 22, 2021. URL: https://www.who.int/publications-detail-redirect/9789240034228 (visited on 05/29/2024).

[65] M. C. Woody et al. “Estimates of non-traditional secondary organic aerosols from aircraft SVOC and IVOC emissions using CMAQ”. In: *Atmospheric Chemistry and Physics* 15.12 (June 25, 2015). Publisher: Copernicus GmbH, pp. 6929–6942. ISSN: 1680-7316. DOI: 10.5194/acp-15-6929-2015. URL: https://acp.copernicus.org/articles/15/6929/2015/ (visited on 01/08/2024).

[66] Steve H L Yim et al. “Global, regional and local health impacts of civil aviation emissions”. In: *Environmental Research Letters* 10.3 (Mar. 1, 2015), p. 034001. ISSN: 1748-9326. DOI: 10.1088/1748-9326/10/3/034001. URL: https://iopscience.iop.org/article/10.1088/1748-9326/10/3/034001 (visited on 01/12/2023).

[67] Yihui Yin et al. “Identification of key volatile organic compounds in aircraft cabins and associated inhalation health risks”. In: *Environment International* 158 (Jan. 1, 2022), p. 106999. ISSN: 0160-4120. DOI: 10.1016/j.envint.2021.106999. URL: https://www.sciencedirect.com/science/article/pii/S0160412021006243 (visited on 04/07/2023).

[68] Oleksandr Zaporozhets and Kateryna Synylo. “Викиди зважених часток від повітряних суден під час експлуатації в межах аеропорту”. In: *Proceedings of the National Aviation University* 69.4 (2016), p. 77. ISSN: 2306-1472. URL: https://www.academia.edu/33602570/PM_EMISSIONS_PRODUCED_BY_AIRCRAFT_UNDER_THE_OPERATIONS_AT_THE_AIRPORT (visited on 03/01/2023).

[69] Chi Zhang et al. “Characterizing particulate matter emissions in an aviation kerosene-fueled model combustor at elevated pressures and temperatures”. In: *Fuel* 241 (Apr. 1, 2019), pp. 227–233. ISSN: 0016-2361. DOI: 10.1016/j.fuel.2018.12.024. URL: https://www.sciencedirect.com/science/article/pii/S0016236118320763 (visited on 04/06/2023).

A

COMSOL Model

A.1. COMSOL Variables

Variable Name	Description	Formula Used	Example Unit
D	Engine diameter	-	1.016 m
L	Engine length	-	2.6 m
U_jet	Jet velocity	-	44.85 m/s
U_wind	Ambient Wind speed	-	10 m/s
beta	Ambient Wind Angle	-	1.5708 rad
Ux_wind	X wind velocity	U_wind*cos(beta)	6.1232E-16 m/s
Uy_wind	Y wind velocity	U_wind*sin(beta)	10 m/s
alpha	Wind angle corrected for Airplane Speed	atan(Uy_wind/(Ux_wind+U_plane))	0.12167 rad
p_ref	Reference pressure		1,01E+09
T_ref	Reference temperature		292.22 K
U_plane	Aircraft velocity	-	81.786 m/s
d_jet	Jet seperation distance	-	5.175 m
Length	Domain length	-	1500 m
Height	Domain height	-	500 m
Width	Domain width	-	600 m
a	Speed of sound	sqrt(gamma*R_air*T_ref)	342.66 m/s
U_i	Jet engine speed corrected with Airplane speed	U_jet+U_plane	126.64 m/s
gamma	Heat Capacity ratio	-	1.4
M	Ambient wind speed expressed in Mach Number	sqrt(Uy_wind^2+(Ux_wind+U_plane)^2)/a	0.24046
Mx	Wind Speed (x) expressed in Mach number	(Ux_wind+U_plane)/a	0.23868
My	Wind Speed (Y) expressed in Mach number	Uy_wind/a	0.029184
Te	Temperature Exhaust air		841.52 K
pe	Static Pressure	-	1.614E5 Pa
rhoe	Density of Air	pe/(R*Te)	1.0153 kg/m³
R	Specific Heat Capacity for air	-	188.9 J/(kg·K)
A	Area of the jet engine outlet	pi*(D/2)^2	0.81073 m²
me	Mass Flow Jet Outlet	-	59.46 kg/s
ue	Jet engine speed based on area	me/(rhoe*A)	72.234 m/s
Me	Jet engine exit speed based expressed in Mach Number	ue/a	0.2108
MCO2	Molar Mass of CO_2	-	0.04401 kg/mol
Rg	Ideal Gas constant	-	8.314 J/(mol·K)
c_co2_ppm	Concentration of CO_2 in parts per million	-	2,00E-04
c_co2_molm3	Concentration of CO_2 in mol per m^3	c_co2_ppm*pe/(Rg*Te)	0.0046138 mol/m³
R_air	Specific Gas constant for Air	-	287 J/(kg·K)

Figure A.1: All the variables used in the COMSOL model

A.2. Time Dependent Study

time_plume_arrival	t_ac_closest
2022-07-28 12:46:07.085974782+00:00	2022-07-28 12:45:30+00:00
2022-07-28 12:42:09.085974782+00:00	2022-07-28 12:41:32+00:00
2022-07-28 12:28:36.085974782+00:00	2022-07-28 12:27:59+00:00
2022-07-28 12:30:53.085974782+00:00	2022-07-28 12:30:16+00:00
2022-07-28 12:37:22.085974782+00:00	2022-07-28 12:36:45+00:00
2022-07-28 12:48:55.085974782+00:00	2022-07-28 12:48:18+00:00
2022-07-28 13:28:11.176407330+00:00	2022-07-28 13:27:31+00:00
2022-07-28 13:45:29.176407330+00:00	2022-07-28 13:44:49+00:00
2022-07-28 14:05:26.176407330+00:00	2022-07-28 14:04:46+00:00
2022-07-28 13:10:32.880183633+00:00	2022-07-28 13:09:45+00:00
2022-07-28 13:39:37.176407330+00:00	2022-07-28 13:38:57+00:00
2022-07-28 13:17:17.880183633+00:00	2022-07-28 13:16:30+00:00
2022-07-28 08:07:32.251843877+00:00	2022-07-28 08:07:01+00:00
2022-07-28 13:22:05.880183633+00:00	2022-07-28 13:21:18+00:00
2022-07-28 14:10:10.176407330+00:00	2022-07-28 14:09:30+00:00
2022-07-28 13:32:48.176407330+00:00	2022-07-28 13:32:08+00:00
2022-07-28 08:14:54.251843877+00:00	2022-07-28 08:14:23+00:00
2022-07-28 08:16:24.251843877+00:00	2022-07-28 08:15:53+00:00
2022-07-28 14:13:24.176407330+00:00	2022-07-28 14:12:44+00:00
2022-07-28 13:14:58.880183633+00:00	2022-07-28 13:14:11+00:00
2022-07-28 13:18:21.880183633+00:00	2022-07-28 13:17:34+00:00
2022-07-28 13:19:39.880183633+00:00	2022-07-28 13:18:52+00:00
2022-07-28 13:25:14.880183633+00:00	2022-07-28 13:24:27+00:00
2022-07-28 13:35:09.176407330+00:00	2022-07-28 13:34:29+00:00
2022-07-28 13:36:40.176407330+00:00	2022-07-28 13:36:00+00:00
2022-07-28 13:38:37.176407330+00:00	2022-07-28 13:37:57+00:00
2022-07-28 13:48:55.176407330+00:00	2022-07-28 13:48:15+00:00
2022-07-28 13:54:44.176407330+00:00	2022-07-28 13:54:04+00:00
2022-07-28 13:57:32.176407330+00:00	2022-07-28 13:56:52+00:00
2022-07-28 13:59:49.176407330+00:00	2022-07-28 13:59:09+00:00
2022-07-28 14:07:36.176407330+00:00	2022-07-28 14:06:56+00:00
2022-07-28 14:15:39.176407330+00:00	2022-07-28 14:14:59+00:00
2022-07-28 07:39:19.092869614+00:00	2022-07-28 07:38:45+00:00
2022-07-28 11:56:07.768885463+00:00	2022-07-28 11:55:29+00:00
2022-07-28 11:56:07.768885463+00:00	2022-07-28 11:55:29+00:00
2022-07-28 11:56:07.768885463+00:00	2022-07-28 11:55:29+00:00
2022-07-28 11:56:07.768885463+00:00	2022-07-28 11:55:29+00:00
2022-07-28 11:56:08.768885463+00:00	2022-07-28 11:55:30+00:00
2022-07-28 11:56:08.768885463+00:00	2022-07-28 11:55:30+00:00
2022-07-28 11:56:08.768885463+00:00	2022-07-28 11:55:30+00:00
2022-07-28 11:56:08.768885463+00:00	2022-07-28 11:55:30+00:00
2022-07-28 08:53:11.574931471+00:00	2022-07-28 08:52:38+00:00
2022-07-28 08:27:29.574931471+00:00	2022-07-28 08:26:56+00:00

Figure A.2: Snippit of the data with the time when the aircraft was closest to the measuring station and the time of the plume arrival

A.3. Mesh Resolutions

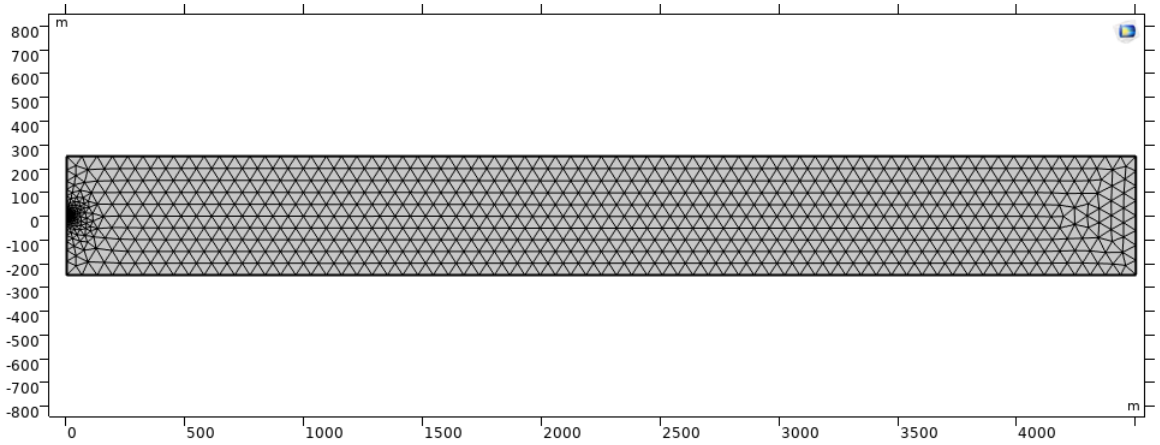

Figure A.3: An extremely coarse mesh applied to the domain

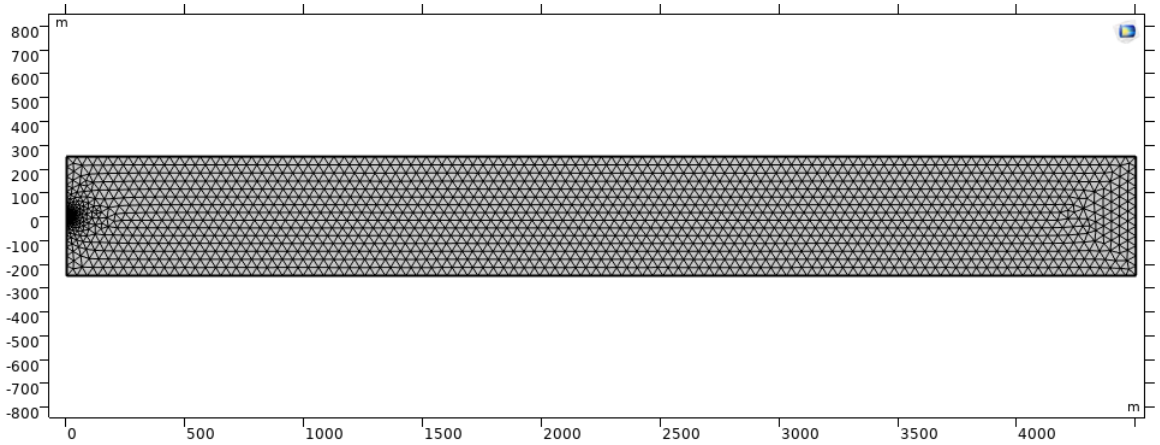

Figure A.4: An extra coarse mesh applied to the domain

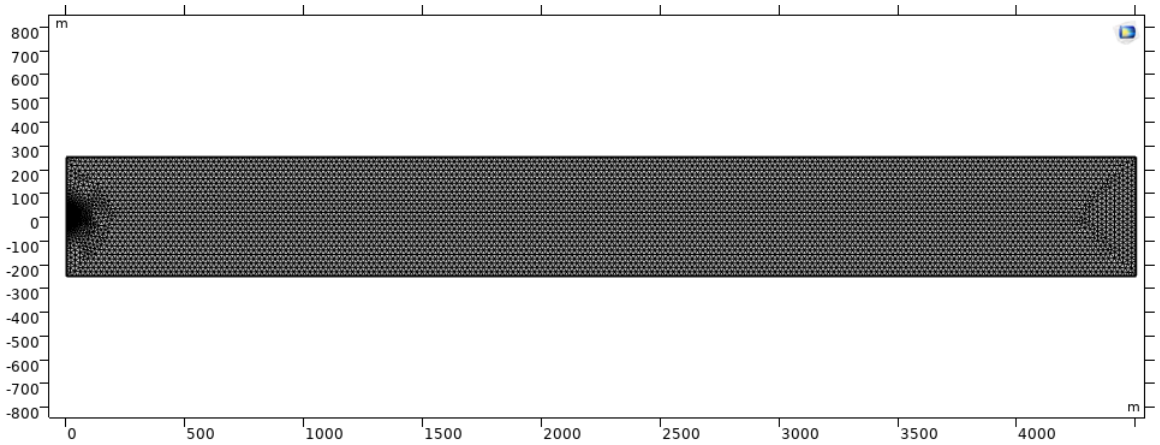

Figure A.5: A coarse mesh applied to the domain

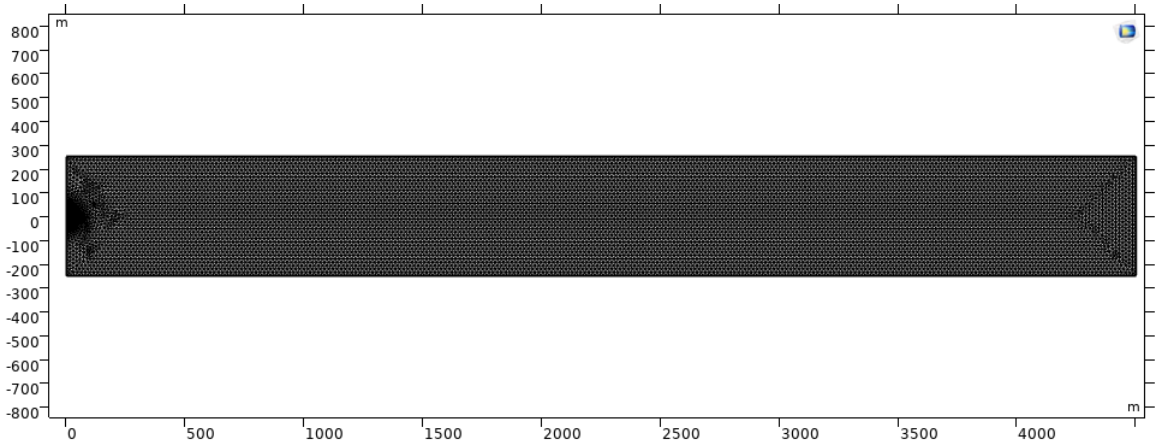

Figure A.6: A normal mesh applied to the domain

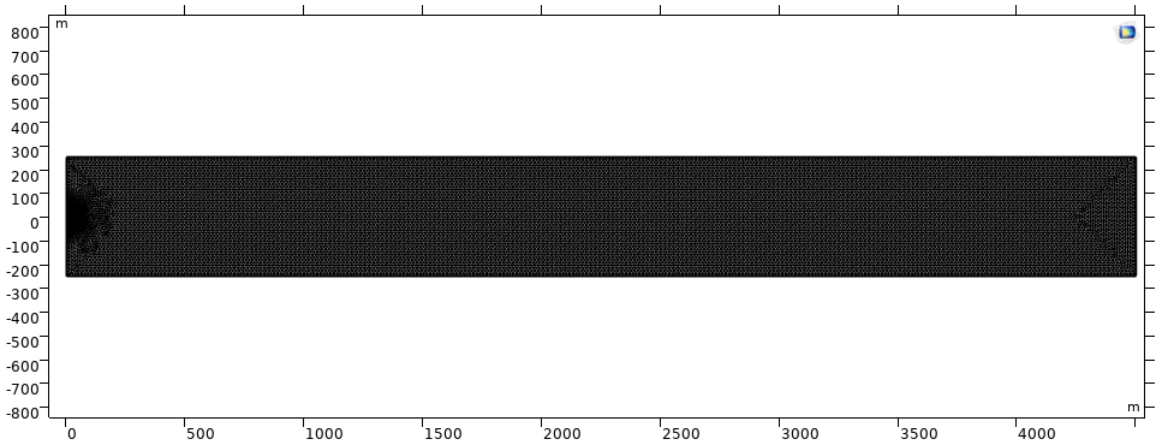

Figure A.7: A fine mesh applied to the domain

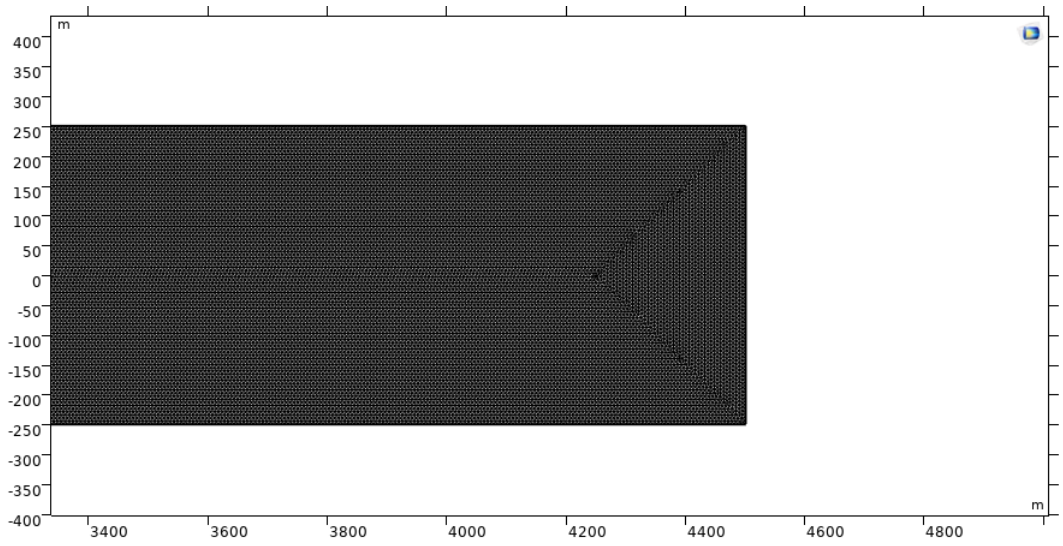

Figure A.8: A finer mesh applied to the domain

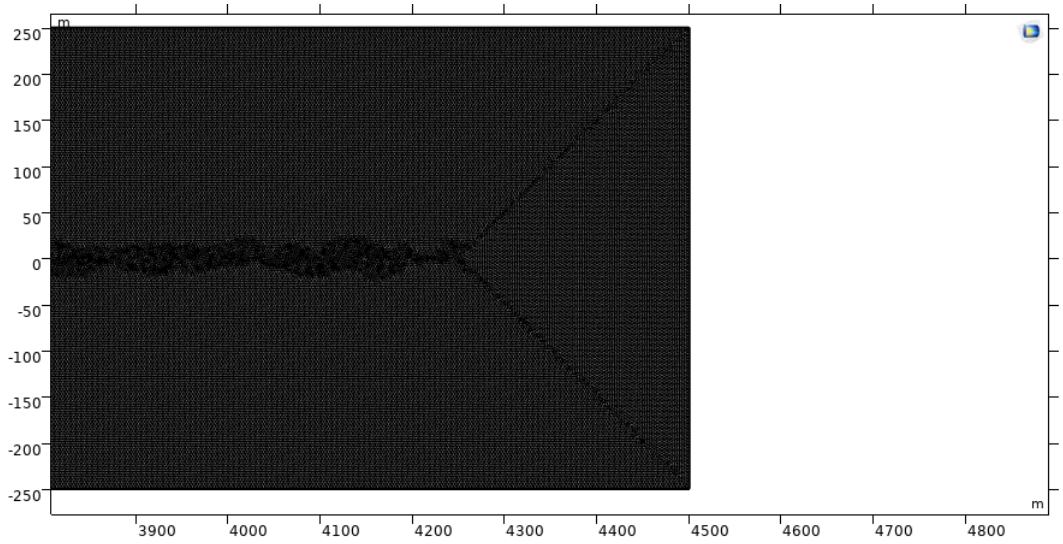

Figure A.9: An extra fine mesh applied to the domain

A.4. Aircraft velocity

Velocity Arrivals	velocity Departures
26,770867	70,05699828
21,09847677	78,33244032
64,4062521	84,46913567
73,74514815	84,49576307
21,63113146	82,95479289
45,85771245	85,52312384
24,20074933	83,46843992
73,3114288	82,41386457
45,85771245	80,38671063
22,6413812	85,52312384
22,1450067	79,84495716
49,48298824	80,38671063
42,77625834	80,90030605
46,37135551	79,84495716
29,32782032	75,25139404
47,97862616	77,30537509
62,86539359	82,4411558
65,94722628	86,61165495
22,1450067	77,85120333
48,45614642	83,9820967
46,9160518	81,3862765
48,96955659	68,03120739
27,78473896	86,03681791
33,4546853	81,41391218
49,45356353	78,27836433
48,42609779	84,52551317
47,39869375	78,3037171
53,0775587	74,16741128
49,96731835	84,98297239
51,48553907	79,30617713
46,88501613	83,49855605
70,57076714	83,46843992
49,45356353	77,81890169
49,45356353	80,35872169
51,50866536	80,35872169
52,02247385	80,35872169
45,85771245	80,35872169
53,14731894	80,35872169
72,1121315	80,35872169
49,9964407	80,35872169
48,42609779	80,35872169
72,62593819	76,248862

Figure A.10: The velocity of the aircraft for both arrivals and departures

A.5. Wind Speed Sensitivity

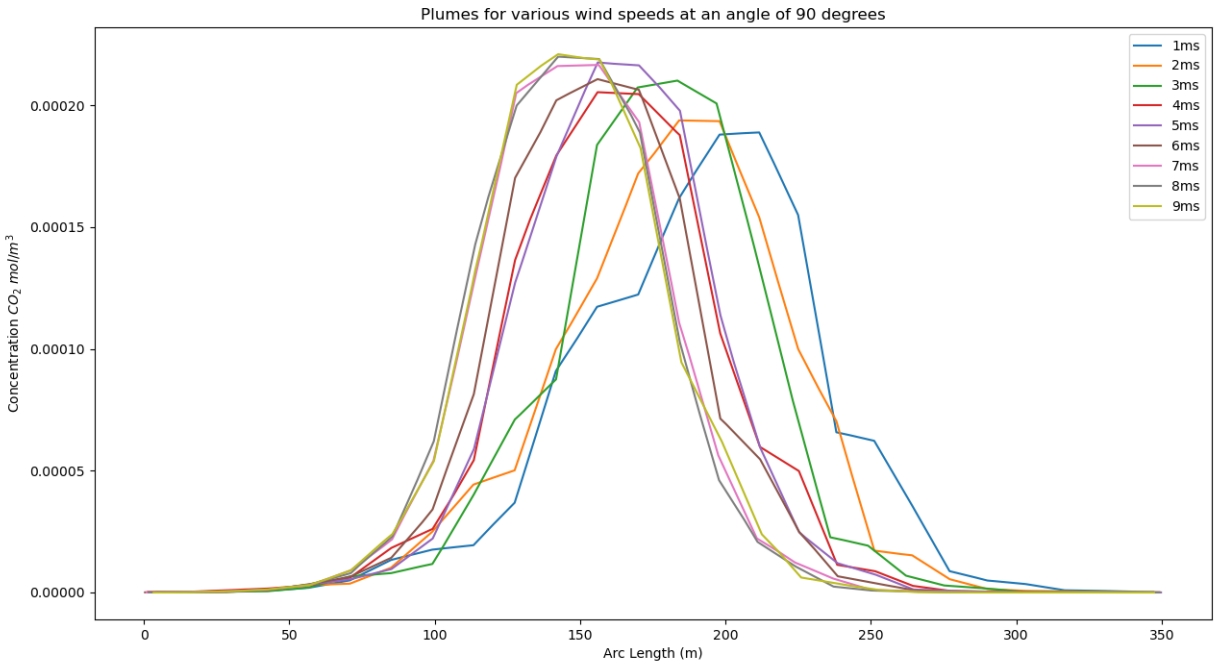

Figure A.11: The plumes simulated for different wind speeds

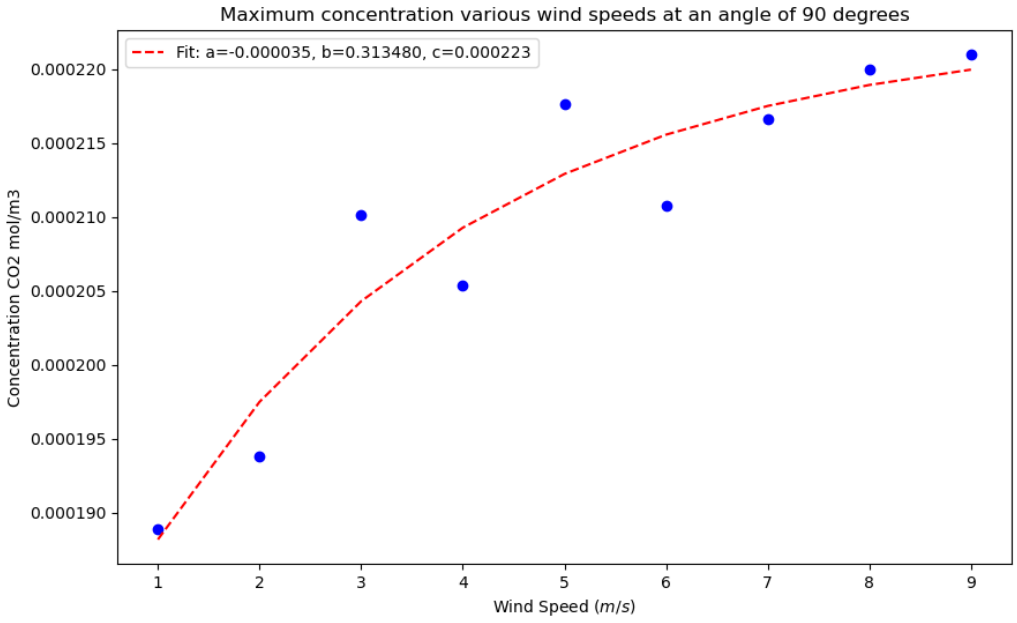

Figure A.12: The maximum concentration of the plume for different crosswind velocities

A.6. Emissions Databank Thrust Levels

Manufacturer	Engine Identification	Rated Thrust (kN)
General Electric Company	GE90-115B	513,9
General Electric Company	GE90-115B	513,9
General Electric Company	GE90-115B	513,9
General Electric Company	GE90-113B	504,9
General Electric Company	GE90-113B	504,9
General Electric Company	GE90-110B1	492,6
General Electric Company	GE90-110B1	492,6
General Electric Company	GE90-110B1	492,6
Rolls-Royce plc	Trent XWB-97	436,7
Rolls-Royce plc	Trent XWB-97	436,7
Rolls-Royce plc	Trent XWB-97	436,7
General Electric Company	GE90-94B	432,8
General Electric Company	GE90-94B	432,8
General Electric Company	GE90-94B	430,9
General Electric Company	GE90-92B	426,7
General Electric Company	GE90-92B	426,7
Pratt & Whitney	PW4098	424,1
General Electric Company	GE90-90B	419,3
General Electric Company	GE90-90B	418,1
General Electric Company	GE90-90B	418,1
General Electric Company	GE90-90B	418,1
Rolls-Royce plc	Trent 895	413,1
Rolls-Royce plc	Trent 892	411,5
General Electric Company	GE90-90B	410,8
Pratt & Whitney	PW4090	408,3
General Electric Company	GE90-85B	397,2
General Electric Company	GE90-85B	395,3
General Electric Company	GE90-85B	395,3

Figure A.13: The emissions databank containing the thrust levels of the different jet engines

A.7. Aircraft Velocity Sensitivity

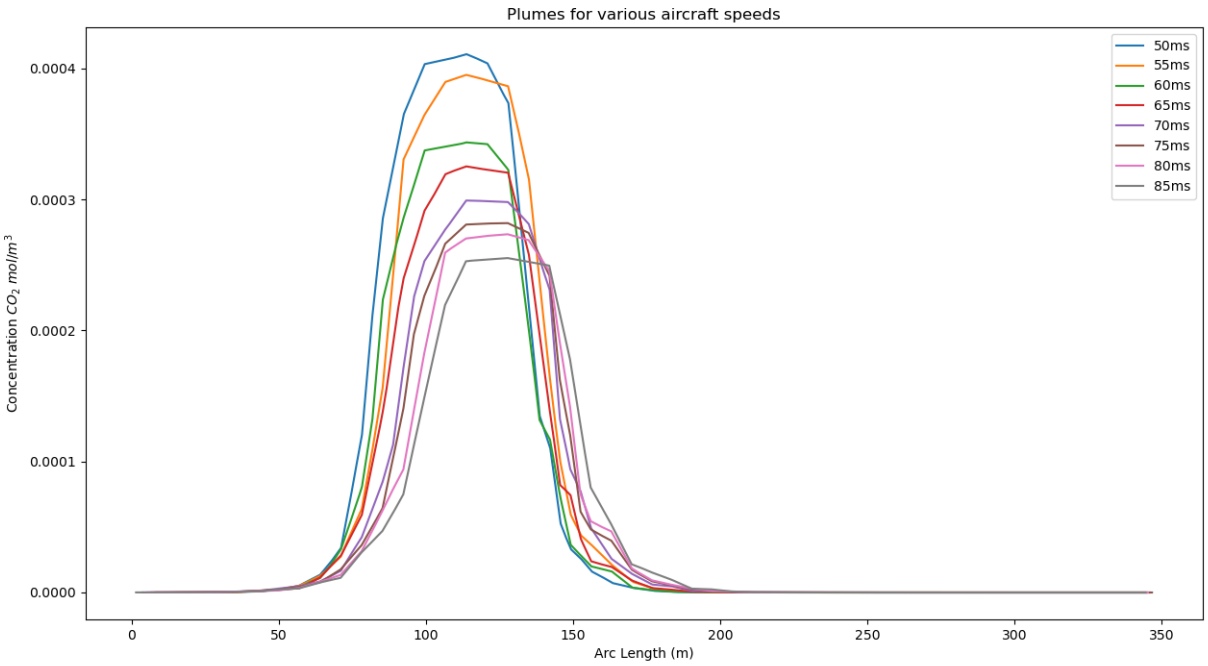

Figure A.14: The emissions databank containing the thrust levels of the different jet engines

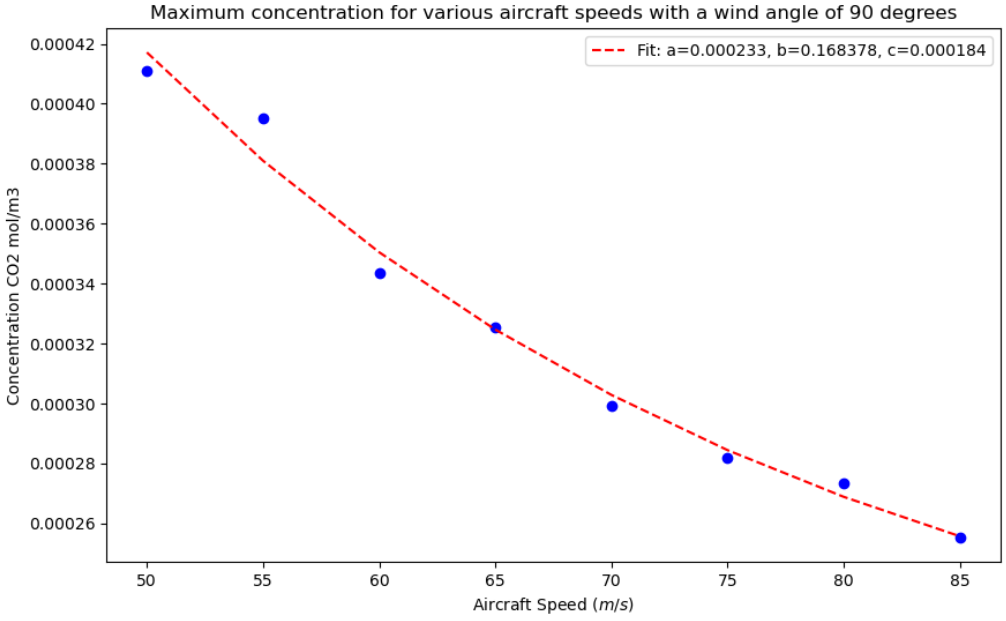

Figure A.15: The peak concentration of the plume when comparing the different speeds aircraft travel at

A.8. Jet Engine Exit Speed

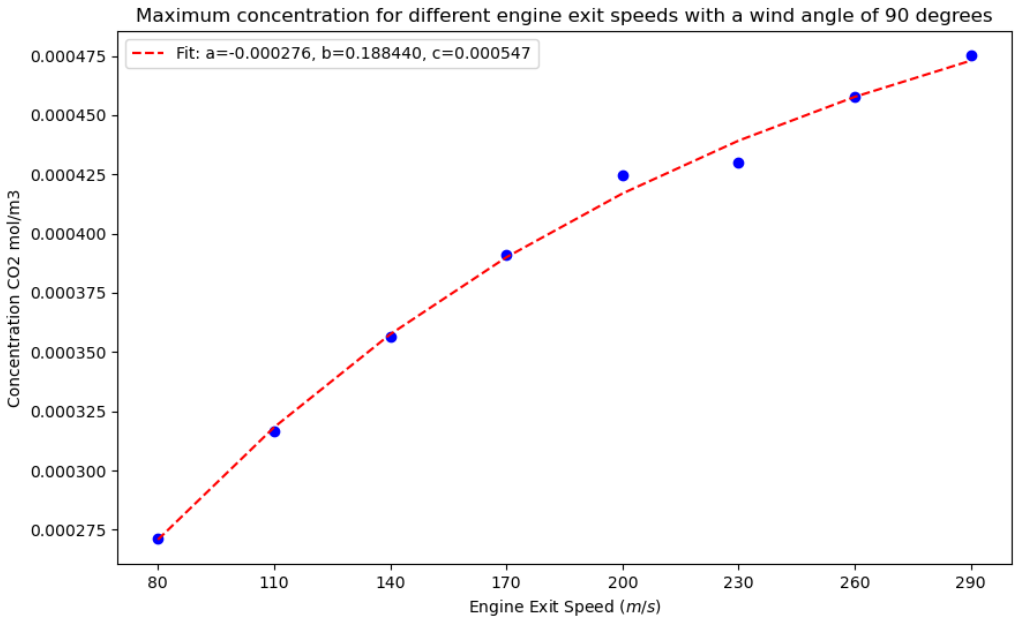

Figure A.16: The peak concentration for different exit velocities

A.9. Input Concentration Sensitivity

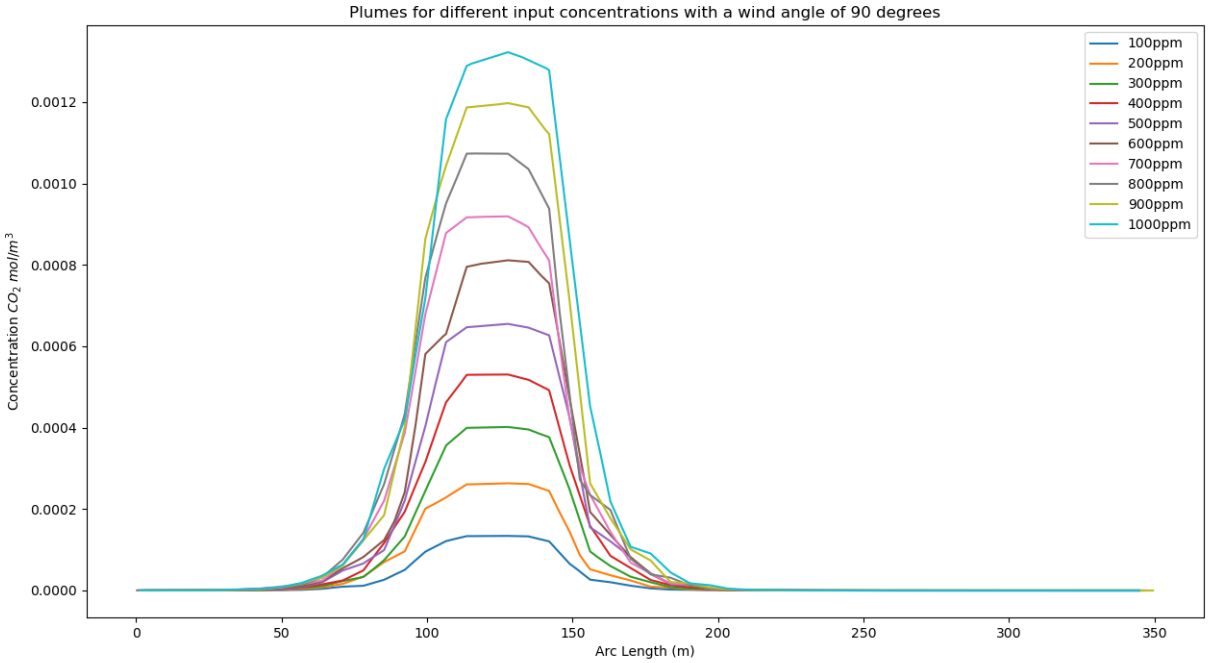

Figure A.17: The complete plumes for different input concentrations

A.10. Engine separation Distance Sensitivity

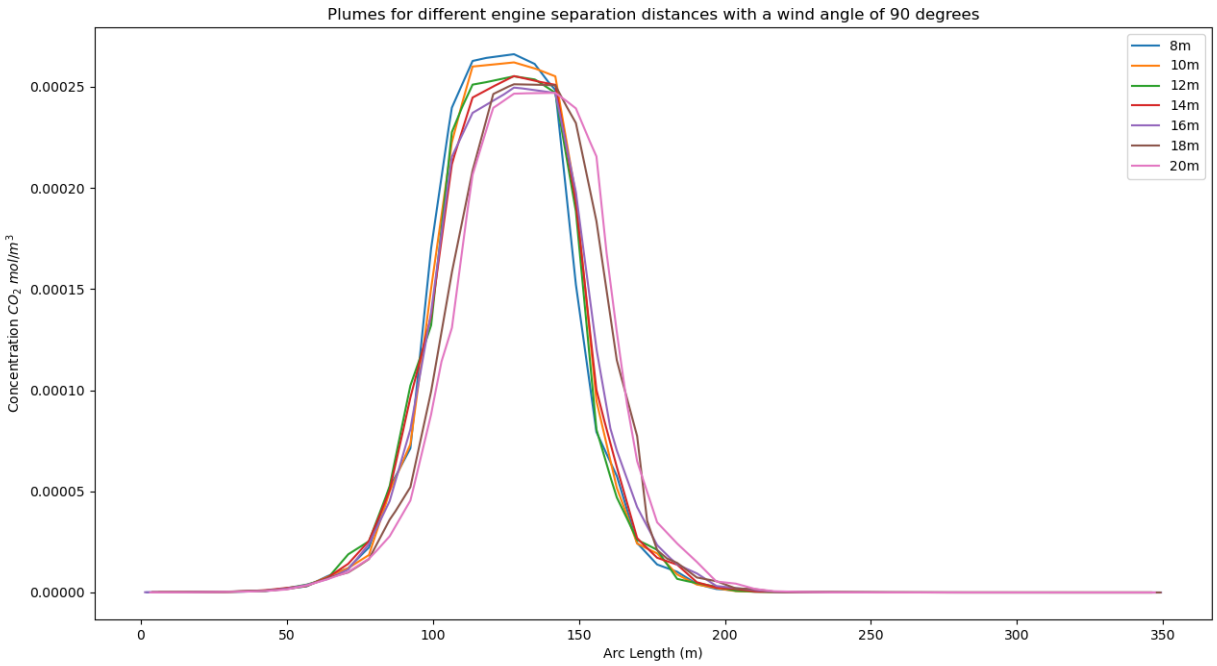

Figure A.18: The complete plumes for different engine separation distances

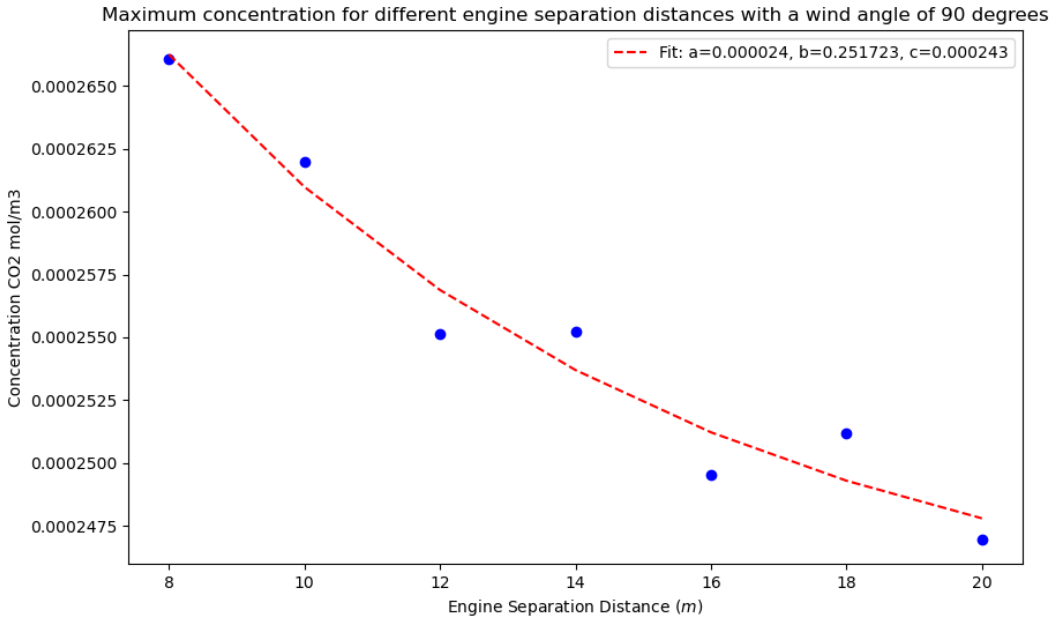

Figure A.19: The peak concentration when comparing the distances between the engines

A.11. Engine Exit Velocity Sensitivity

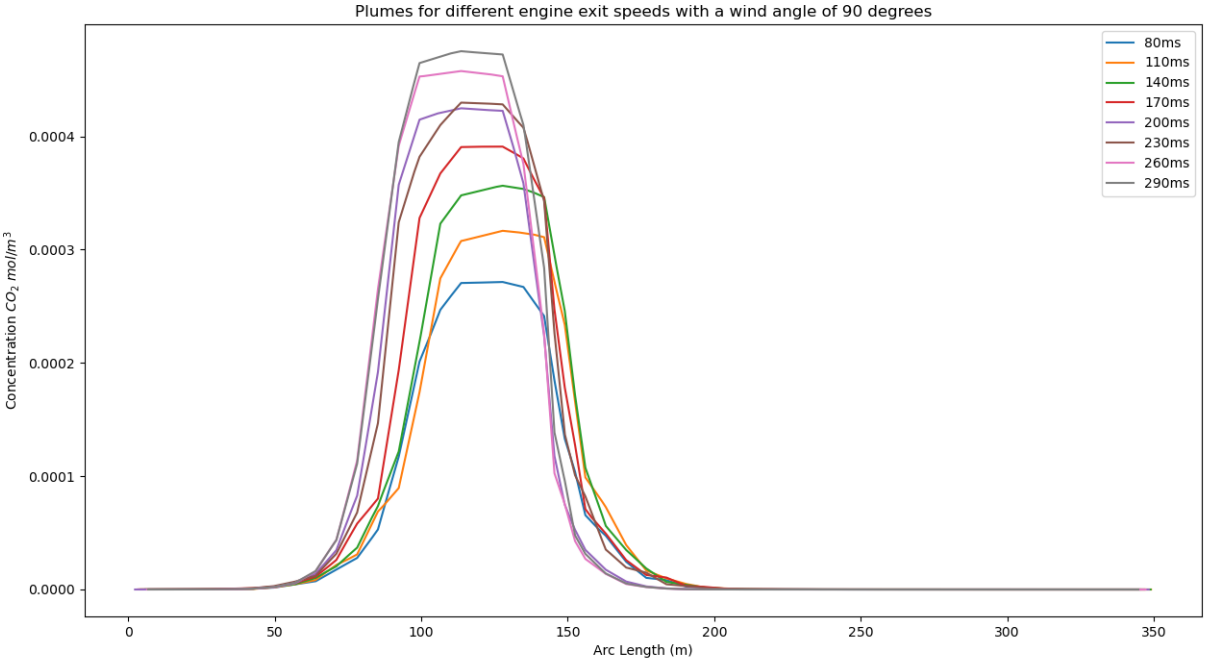

Figure A.20: The complete plumes for different engine exit velocities

A.12. Emissions Indices CO

CO EI T/O (g/kg)	CO EI C/O (g/kg)	CO EI App (g/kg)	CO EI Idle (g/kg)
1,39	2,03	22,38	58,6
1,13	1,62	15,56	47,7
0,75	0,92	3,28	17,35
0,87	1,07	3,96	26,04
0,77	0,96	3,91	23,73
0,12	0,01	1,36	32,59
0,79	0,97	3,8	22,43
0,75	0,56	6,72	39,91
0,77	0,97	3,93	23,95
0	0	1,4	32,84
0,74	0,55	6,8	40,07
0,83	1,03	4,21	25,58
0	0	1,83	32,4
0,5	0,5	7,62	38,47
0,77	0,97	3,93	23,8
0	0	1,51	32,68
0,74	0,55	6,79	39,97
0,71	0,74	4,08	34,17
0,83	1,03	4,22	25,73
0	0	2	34,86
0,5	0,5	7,65	41,29
0,97	1,19	4,5	29,88
0,77	0,64	5,63	37,97
0,94	1,16	4,28	26,32
0,94	1,16	4,28	26,32
0	0	2,02	35,07
0,87	1,07	3,96	26,04
0	0	1,62	36,04
0	0	1,97	23,09
0,75	0,56	6,72	39,91
0,74	0,55	6,8	40,07

Figure A.21: The emissions indices of CO for different engines and operating modes

A.13. Cross-Section sensitivity versus the wind speed

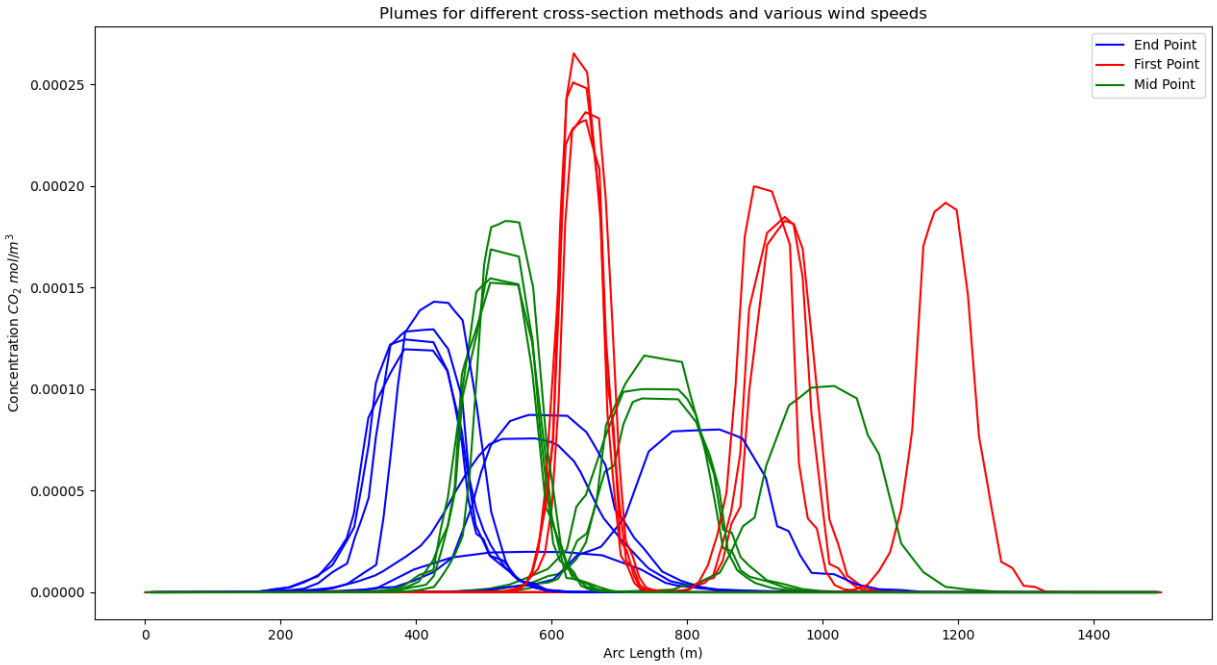

Figure A.22: The entire plumes for the different wind speeds and cross sections

A.14. Plume Duration Times

p2_old_time_plume_start	p2_old_time_plume_end
14:20:51	14:21:36
14:01:53	14:02:30
14:03:37	14:04:10
14:14:29	14:15:03
14:09:37	14:10:21
14:07:15	14:07:55
14:13:22	14:13:52
14:11:16	14:11:45
14:39:24	14:39:58
14:33:46	14:34:17
15:16:39	15:17:17
14:36:17	14:36:46
14:45:15	14:46:00
14:49:23	14:50:01
14:52:52	14:53:28
15:26:51	15:27:23
15:29:59	15:30:32
15:37:52	15:38:26
15:40:43	15:41:31
15:42:29	15:43:05
16:25:20	16:25:47
16:04:40	16:05:16
16:01:54	16:02:56
16:08:36	16:09:15
16:13:10	16:14:21
16:15:36	16:16:14
16:47:01	16:48:00
16:29:05	16:29:37
16:35:08	16:36:00

Figure A.23: The start and end times of the plumes at the measurement station

B

Plume Width Results

B.1. Departing Aircraft used for simulating and measuring plume width

Departure Aircraft Models	
Embraer EMB-190 STD	A320 214
EMB-190 STD	Boeing 787-9 Dreamliner
ERJ-175STD	777 206ER
A320-214	A320-251N
Boeing 767 319ER/W	737NG 86N/W
Boeing 777-206(ER)	777 306ER
777 206ER	777 306ER
737NG 8K2/W	ERJ-190STD
787 8	ERJ-175STD
777-F	787 9
737NG 8K2/W	EMB-175 200STD
737NG 8K2/W	EMB-190 STD
EMB-190 STD	EMB-175 200STD
737NG 8K2/W	Embraer ERJ-175
EMB-190 STD	Boeing 737NG 8K2/W
EMB-190 STD	EMB-190 STD
AIRBUS A320-214	A350-941
777-224	A320-214
EMB-190 STD	787-9
A330-323	A330-941
A319 111	A330-941
A330 203	777-224
777 306ER	EMB-175 200STD
787-9	A350-941
A330 303	Boeing 787-10
A321-271NX/LR	Boeing 787 9
A330-343(P2F)	777 306ER
A380 861	Embraer EMB-190 STD
A330 223F	ERJ-175STD
737NG 8K2/W	B777-206ER
A330-323	737NG 7K2/W
A350-941	AIRBUS A319-111
EMB-190 STD	EMB-190 STD
Embraer EMB-175 200STD	EMB-190 STD
E195-E2	737NG 8K2/W
737NG 8K2/W	ERJ-145 LU
Boeing 777-306(ER)	737NG 86N/W
737NG 800/W	A320 214SL
ERJ-175STD	CRJ 900 LR NG
Boeing 787-10	EMB-190 STD
A350-941	ERJ-190STD
CL-600-2D24	EMB-190 STD
C Series 300	ERJ-175STD
777 206ER	E195-E2
A330-323	787 8

Figure B.1: The different aircraft measured and simulated departing the Polderbaan at Schiphol regarding the plume width

B.2. Departing Aircraft's Engine diameter used for simulating and measuring plume width

Aircraft Engine Diameters Departures (Inch)
155.6
57
118.5
65
62.7
139.1
112
79
72
55.7
106.9
60.7
118
78
106
114
57.6
94.6

Table B.1: The different unique diameter values that occur in the measurements and simulations

B.3. Departing Aircraft's Engine separation distance used for simulating and measuring plume width

Engine Separation Distances (m)
18
10
9.65
9.4
18.9
19.46
11.52
4.10
18.74
9.8
4.80
11.51
21
5.60
13.50
14.30
11.50

Table B.2: The different unique engine separation distances that occur in the measurements and simulations

B.4. Arriving Aircraft used for simulating and measuring plume width

Arrivals Aircraft Models	
ERJ-175STD	737NG 7K2/W
EMB-190 STD	Boeing 787 9
737NG 7K2/W	737NG 8K2/W
737NG 8K2/W	AIRBUS A320-214
EMB-190 STD	737NG 8K2/W
EMB-190 STD	EMB-175 SD
AIRBUS A319-131	A320-214
EMB-175 200STD	AIRBUS A319-111
EMB-190 STD	737NG 7K2/W
737NG 8K2/W	777 FFX
777-F	Boeing 777 206ER
787 9	Airbus A320 232SL
EMB-190 STD	Boeing 757-308
A320-214	A320 214
737NG 8K2/W	737NG 8K5/W
Embraer EMB-190 LR	A330 303
A319-112	Embraer EMB-190 STD
A320-214	787 9
A320 232SL	B777-206ER
EMB-190 STD	EMB-190 STD
EMB-190 STD	737NG 8K2/W
A320-214	ERJ 190-100 SR Embraer 190
AIRBUS A319-131	EMB-190 LR
Boeing 777-39P(ER)	EMB-190 STD
A350-941	737NG 9K2/W
EMB-190 STD	BOEING 737-8AS
A320-271N	777 306ER
737NG 7K2/W	Embraer EMB-175 200STD
Boeing 787 9	Embraer EMB-190 STD
737NG 8K2/W	777 306ER
737NG 7K2/W	777 206ER
Boeing 737NG 8K2/W	777 306ER
777F	737NG 8K2/W
737NG 8K2/W	EMB-190 STD
ERJ-175STD	Boeing 737NG 8K2/W
737NG 8K2/W	737NG 8K2/W
A321-251NX	737NG 8K2/W
737NG 8K2/W	Embraer ERJ-175
EMB-190 STD	737NG 7K2/W
EMB-175 200STD	737NG 8K2/W
737NG 8K2/W	737NG 8K2/W
787 9	EMB-190 STD
A320 214	Boeing 777 306ER
EMB-190 STD	787 8
EMB-190 STD	737NG 7K2/W
AIRBUS A319-111	777 206ER
A330 343E	777 306ER
A320-214	EMB-190 STD
EMB-190 STD	Embraer EMB-175 200STD
EMB-190 STD	Embraer EMB-190 STD
737-8K2	777 206ER
737NG 8K2/W	737NG 8K2/W
737NG 8K2/W	737NG 8K2/W
A320-271N	EMB-170 LR
A320-214	B777-206ER
787 9	737NG 8K2/W
A319-111	777 206ER
B787-9	737NG 9K2/W
A320-251N	737NG 8BK/W
Boeing 737NG 8HC/W	AIRBUS A319-111

Figure B.2: The different aircraft measured and simulated arriving at the Polderbaan at Schiphol regarding the plume width

B.5. Arriving Aircraft's Engine diameter used for simulating and measuring plume width

Aircraft Engine Diameters Departures (Inch)
155.6
65
57
139.1
62.7
72
67.5
53
118
86.3
114
57.6
78
84.6

Table B.3: The different unique diameter values that occur in the measurements and simulations covering the plume width in Arrivals

B.6. Arriving Aircraft's Engine separation distance used for simulating and measuring plume width

Engine Separation Distances (m)
18
9.65
10
18.9
19.46
9.40
11.52
21.50
11.50
21
10.54
18.74
9.80

Table B.4: The different unique engine separation distances that occur in the measurements and simulations covering the plume width in Arrivals

C

Concentration Results

C.1. Arriving Aircraft used for simulating and measuring concentration levels

Aircraft Model
AIRBUS A320-232
737NG 8K2/W
A330-323
EMB-190 STD
ERJ 190-100 SR Embraer 19
A330-323
777 206ER
EMB-190 STD
737NG 8K2/W
EMB-190 STD
737NG 8K2/W
737NG 8K2/W
777 206ER
EMB-175 200STD
Boeing 787-10
737NG 8K2/W
E195-E2
AIRBUS A320-232
EMB-190 STD
737NG 8K2/W
A320-251N
Boeing 737NG 8K2/W
Boeing 737NG 8K2/W
737NG 8K2/W
737NG 9K2/W
EMB-190 STD
777 306ER
737NG 8K2/W
AIRBUS A320-232
Embraer E175STD
737NG 8K2/W
737NG 8K2/W
737NG 8K2/W
EMB-190 STD
737-8K2
737NG 7K2/W
ERJ-175STD
737NG 8K2/W
737NG 8K2/W

Figure C.1: The different aircraft measured and simulated arriving at the Polderbaan at Schiphol regarding concentration levels

C.2. Departing Aircraft used for simulating and measuring concentration levels

Aircraft Model
Embraer EMB-190 STD
EMB-190 STD
ERJ-175STD
A320-214
737NG 8K2/W
ERJ-175STD
737NG 8K2/W
737NG 8K2/W
EMB-190 STD
737NG 8K2/W
EMB-190 STD
EMB-190 STD
AIRBUS A320-214
EMB-190 STD
A319 111
CL-600-2D24
C Series 300
A330 303
A321-271NX/LR
A330-343(P2F)
ERJ-190STD
A330 223F
737NG 8K2/W
A330-323
A320 214
EMB-190 STD
Embraer EMB-175 200STD
Embraer EMB-175 200STD
Embraer EMB-175 200STD
Embraer EMB-175 200STD
Embraer EMB-175 200STD
Embraer EMB-175 200STD
Embraer EMB-175 200STD
Embraer EMB-175 200STD
DHC-8-402 Dash 8
E195-E2

Figure C.2: The different aircraft measured and simulated departing at the Polderbaan at Schiphol regarding concentration levels

D

Gaussian Line Source

D.1. Gaussian Theory

In addition to the CFD approach in COMSOL to model the plume and concentration levels, another method was used. This method was built on the Gaussian dispersion theory [17]. There have been many variations on the Gaussian plume theory. This includes the type of source that can used. One of these source types is Line Sources. Line sources, like roads, trains, or rivers, are extended sources that exhaust pollutants along a line. The Gaussian plume model considers the dispersion of pollutants from these sources because the emissions are dispersed over the length of the source. One model that has improved the theory behind this is by Briant et al. [10]. The model was originally created to estimate pollutants from roadways. However, a runway can be seen to have characteristics similar to roadways. The Gaussian model is seen as a steady-state model, meaning it is not time-dependent.

The main formula used in the model can be seen in Equation D.1. In this formula, Q is the amount of pollutants emitted in kg/s. The coordinates in the plane are denoted with x, y and z. The wind angle in relation to the runway is θ. While the wind speed is u. σ_y and σ_y are the dispersion coefficients in x and y direction.

$$\begin{aligned} \mathsf{C}(x,y,z) = \frac{\mathsf{Q}}{2\sqrt{2\pi}u\cos\theta\sigma_z\left(\mathsf{d}_{\mathsf{eff}}\right)}\exp\left(\frac{-2^2}{2\sigma_z^2\left(\mathsf{d}_{\mathsf{eff}}\right)}\right) \\ \times\left[\mathsf{erf}\left(\frac{(y-y_1)\cos\theta - x\sin\theta}{\sqrt{2}\sigma_y\left(\mathsf{d}_1\right)}\right) - \mathsf{erf}\left(\frac{(y-y_2)\cos\theta - x\sin\theta}{\sqrt{2}\sigma_y\left(\mathsf{d}_2\right)}\right)\right] \end{aligned} \tag{D.1}$$

In addition, spatial scalars are needed to estimate the location from the line source and the point in question. These can be calculated based on the source extremity location, in other words, the beginning and end point. This is shown in Equation D.2.

$$\begin{aligned} \mathsf{d}_{\mathsf{eff}} &= x/\cos\theta \\ \mathsf{d}_i &= (x-x_i)\cos\theta + (y-y_i)\sin\theta \end{aligned} \tag{D.2}$$

D.1.1. Dispersion Coefficients

As mentioned before, the model needs input dispersion coefficients. In the Gaussian plume model, these are one of the most significant variables is the dispersion coefficients. These coefficients can be calculated in multiple ways. In this model, it is done via Briggs theorem [11]. This theorem uses various classes. These classes are a way of categorizing the stability in the atmosphere and describing the effect of air pollution on its dispersion. The classes range from Category A (extremely unstable) to Category F (extremely stable), and Category D represents a neutral class. There are various metrics and methods that determine which class the atmosphere is. The dispersion coefficient also depends on the distance from the line source. This is seen in Table D.1.

Land category	Stability class	σ_y	σ_z
Rural	A	$0.22x(1+0.0001x)^{-1/2}$	$0.20x$
Rural	B	$0.16x(1+0.0001x)^{-1/2}$	$0.12x$
Rural	C	$0.11x(1+0.0001x)^{-1/2}$	$0.08x(1+0.0002x)^{-1/2}$
Rural	D	$0.08x(1+0.0001x)^{-1/2}$	$0.06x(1+0.00015x)^{-1/2}$
Rural	E	$0.06x(1+0.0001x)^{-1/2}$	$0.03x(1+0.0003x)^{-1}$
Rural	F	$0.04x(1+0.0001x)^{-1/2}$	$0.016x(1+0.0003x)^{-1}$
Urban	A–B	$0.32x(1+0.0004x)^{-1/2}$	$0.24x(1+0.001x)^{-1/2}$
Urban	C	$0.22x(1+0.0004x)^{-1/2}$	$0.20x$
Urban	D	$0.16x(1+0.0004x)^{-1/2}$	$0.14x(1+0.0003x)^{-1/2}$
Urban	E–F	$0.11x(1+0.0004x)^{-1/2}$	$0.08x(1+0.0015x)^{-1}$

Table D.1: Dispersion coefficients for different land categories and stability classes

D.1.2. Stability Classes

To compute the dispersion coefficients, it is necessary to establish the stability class of the atmosphere. These stability classes are identified via the theory of Pasquill [48]. These criteria are seen in Table D.2.

Surface Wind Speed	Strong (>600 W/m^2)	Moderate (600–300 >W/m^2)	Weak (<300 W/m^2)
<2 m/s	A	A–B	B
2–3 m/s	A–B	B	C
3–5 m/s	B	B–C	C
5–6 m/s	C	C–D	D
>6 m/s	C	D	D

Table D.2: Stability class based on surface wind speed and daytime solar insolation.

These classes depend on two variables. One is the surface wind speed, which, in this case, is just the wind speed measured. The other factor is the solar insolation. This can be calculated using the solar constant and the angle of zenith. Seen in Equation D.3. Here, the solar constant is S; this describes the radiation energy the Earth receives per area and unit of time. The angle of zenith (Z) is the angle of the sun with the vertical axis of the earth. This means that throughout the year and time of day, this angle changes, so the correct time must be chosen when trying to simulate the experiments.

$$\text{Daytime Solar Insolation} = S * Cos(Z) \tag{D.3}$$

D.2. Results

The results using this model are produced as follows: the input concentration parameter can be calculated directly as in Equation 4.2, but without the time in mode factor, as the input for this model is in kg/s. The length of the source is the length of the Polderbaan, which is 3800 metres. The model is generated for a height (z) of 1.2, the same as the monitoring station. The x and y are the known coordinates of the station. If all the meteorological conditions measured during the experiments are plugged into the model, a plot like Figure D.1 can be generated. Note that this line source is smaller, which is just for presentation purposes. The problem can be seen by comparing the model concentration values with the experiments. The model values at the location of the monitoring station are all in the order of 0.1 to 0.9 g/m^3, depending on the aircraft type. This is an extreme difference compared to the measured values of the experiments, which have a range of about 1-100 $\mu g/m^3$. These discrepancies indicate that the Gaussian line source approach is not feasible. There are several reasons for this, but the most important is that the Gaussian model is a steady-state model, so this model actually models it as if an aircraft is constantly landing or taking off. This means that a constant rate of pollution is emitted from the entire source. This results in an extreme concentration value compared to the measurements. It was, therefore, decided not to pursue this methodology further.

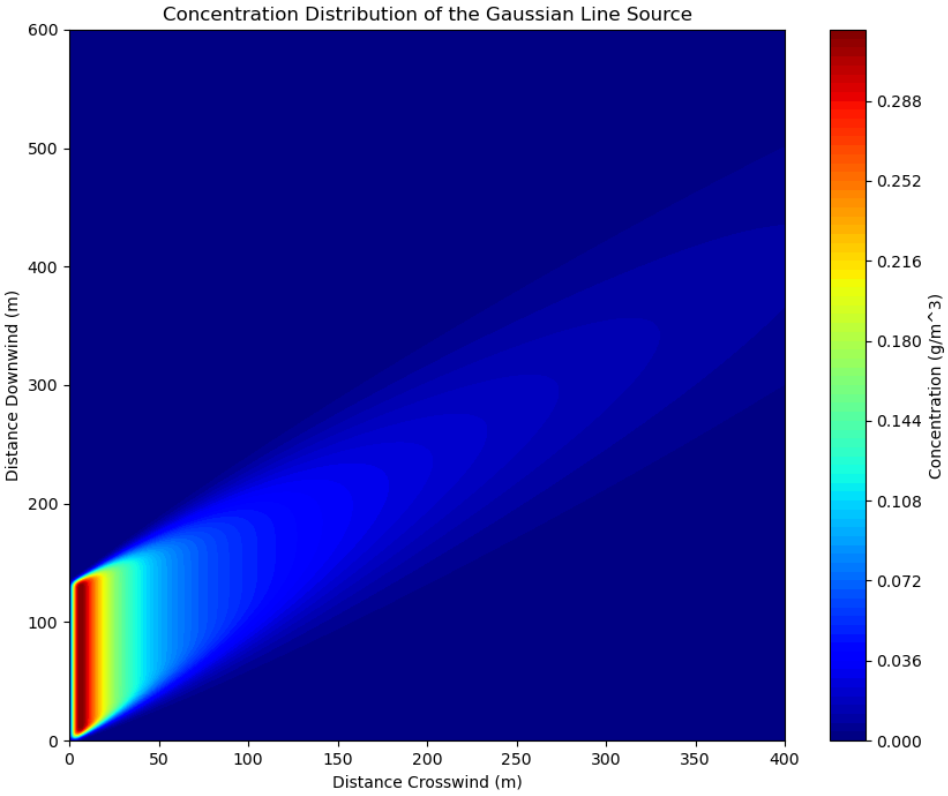

Figure D.1: The concentration plot created using the Gaussian line source at a height of 1.2